Design and Development of a LEBT system and Physics Studies for a High Intensity Proton Linac

By

Rajni Pande

(Enrollment No : PHYS 01200704026)

Bhabha Atomic Research centre

Mumbai 400085

A thesis submitted to the

Board of Studies in ***Physical Sciences***

In partial fulfillment of requirements

for the degree of

DOCTOR OF PHILOSOPHY

Of

HOMI BHABHA NATIONAL INSTITUTE

December, 2014

Homi Bhabha National Institute

Recommendations of the Viva Voce Board

As members of the Viva Voce Board, we certify that we have read the dissertation prepared by Rajni Pande entitled "Design and Development of a LEBT system and Physics Studies for a High Intensity Proton Linac" and recommend that it may be accepted as fulfilling the dissertation requirement for the Degree of Doctor of Philosophy.

	S. Kailas	**Date:** 7/11/2014
Chairman:	Dr. S. Kailas	
	P. Singh	**Date:** 7.11.2014
Guide/Convener:	Dr. P. Singh	
	Pandit	**Date:** 7/11/2014
Member:	Dr. V.S. Pandit	
	Kailash C. Mittal	**Date:** 7/11/2014
Member:	Dr. K.C. Mittal	
	D Kanjilal	**Date:** 07/11/2014
External Examiner:	Dr. D. Kanjilal	

Final approval and acceptance of this dissertation is contingent upon the candidate's submission of the final copies of the dissertation to HBNI. I hereby certify that I have read this dissertation prepared under my direction and recommend that it may be accepted as fulfilling the dissertation requirement.

Date: 7.11.2014

Place: BARC, Mumbai

P. Singh 7/11/2014

Guide: Dr. P. Singh

STATEMENT BY THE AUTHOR

This dissertation has been submitted in partial fulfillment of requirements for an advanced degree at Homi Bhabha National Institute (HBNI) and is deposited in the Library to be made available to borrowers under rules of the HBNI.

Brief quotations from this dissertation are allowable without special permission, provided that accurate acknowledgement of source is made. Requests for permission for extended quotation from or reproduction of this manuscript in whole or in part may be granted by the Competent Authority of HBNI when in his or her judgment the proposed use of the material is in the interests of scholarship. In all other instances, however, permission must be obtained from the author.

Rajni Pande

DECLARATION

I, hereby declare that the investigation presented in the thesis has been carried out by me. The work is original and has not been submitted earlier as a whole or in part for a degree / diploma at this or any other Institution / University.

Rajni Pande

List of Publications

Journals

1. Physics design of a CW high-power proton LINAC for ADS, Rajni Pande, Shweta Roy, S.V.L. S Rao, P. Singh and S. Kailas, Pramana-J Phys., **78**, 247 (2012).
2. Role of beam dynamics studies for accelerator safety, P. Singh, S V L S Rao & Rajni Pande, Ind. J. Pure & Applied Physics, **50**, 439 (2012)
3. Design, development and acceleration trials of Radiofrequency quadrupole, S V L S Rao, Piyush Jain, Rajni Pande, Shweta Roy, Jose V Mathew, Rajesh Kumar, Manjiri Pande, S Krishnagopal, S K Gupta and P Singh, Rev. Sci. Instrum. **85**, 043304 (2014).
4. Electromagnetic and beam dynamics studies of a high current drift tube linac for LEHIPA, S Roy, S V L S Rao, R Pande, S Krishnagopal and P Singh, 2014 JINST **9** P06007.

Technical Report

5. Physics Design of 650 MeV Proton Linac and Transport Line for HFRR at Vizag, Rajni Pande, Shweta Roy, S.V.L.S Rao & P Singh, BARC/2010/015.

Conferences

6. Design of RF structures for a superconducting proton linac, Rajni Pande, Shweta Roy, S. V. L. S. Rao, S. Krishnagopal and P. Singh, Ind. Particle Accelerator Conf. (InPAC-2013), VECC, Kolkata.

7. Transverse Emittance Measurement Studies of a Deuteron Ion Source Beam, Jose V. Mathew, S. V. L. S. Rao, Rajni Pande, M. R. Mishra, L. D. Tayade, P. R. Parate, P. Singh, Ind. Particle Accelerator Conf. (InPAC-2013), VECC, Kolkata.

8. Design, development and acceleration experiments of a four vane RFQ at BARC, S.V.L.S. Rao, Piyush Jain, Jose V. Mathew, Rajni Pande, Shweta Roy,

S. Shrotriya, N. Patel, Shiju, M. R. Mishra, Gireesh Singh, L. Tayade, Praveen P., B.M. Kukreti, Rajesh Kumar, Manjiri Pande, S. Krishnagopal, S.K. Gupta, P. Singh, Ind. Particle Accelerator Conf. (InPAC-2013), VECC, Kolkata.

9. A LEBT for the 400 keV RFQ based neutron generator at BARC, Rajni Pande, S V L S Rao, Shweta Roy, Manas Mishra, L.D Tayade, P.R Parate, Sapna P, Shailaja Ware, S.K Singh, A Agarwal, S.K Gupta, P Singh, Ind. Particle Accelerator Conf. (InPAC-2011), 15-18 February, 2011, IUAC, New Delhi.
10. Design and Development of LEBT for LEHIPA Project, Rajni Pande, Shweta Roy, S V L S Rao, Manas Ranjan Mishra & P Singh, Ind. Particle Accelerator Conf. (InPAC-2011), 15-18 February, 2011, IUAC, New Delhi.
11. Beam Dynamics Studies of Radio Frequency Quadrupole Accelerator for Project X, S.V.L.S Rao, Nikolay Solyak, C.S. Mishra, Rajni Pande, Shweta Roy, P. Singh, Ind. Particle Accelerator Conf. (InPAC-2011), 15-18 February, 2011, IUAC, New Delhi.
12. RF Characterization of DTL Prototype, Shweta Roy, S V L S Rao, Rajni Pande, Piyush Jain, Sumit Garg, Gireesh Singh, S. Krishnagopal and P. Singh, Ind. Particle Accelerator Conf. (InPAC-2011), 15-18 February, 2011, IUAC, New Delhi.
13. Development & Characterization of Prototype RFQ at BARC, Ind. Particle Accelerator Conf. (InPAC-2011), S V L S Rao, Piyush Jain, Rajesh Kumar, Rajni Pande, Shweta Roy, Manas Ranjan Mishra, Gireesh Singh, L D Tayade, Pravin Parate, Sumit Garg, S Krishnagopal, P Singh, S Kailas, P K Nema, 15-18 February, 2011, IUAC, New Delhi.
14. Design Studies of a 650 MeV Proton Linac for MPRR, Rajni Pande, Shweta Roy, V.L.S Rao Sista, P. Singh, P.K. Nema and R.K. Choudhury, Ind. Particle Accelerator Conf. (InPAC-2009), 10-14 February, 2009, RRCAT, Indore.
15. Frequency analysis and field-stabilization for the LEHIPA DTL prototype,

Shweta Roy, S.C.L. Srivastava, Rajni Pande, V.L.S. Rao Sista, S. Krishnagopal and P. Singh, Ind. Particle Accelerator Conf. (InPAC-2009), 10-14 February, 2009, RRCAT, Indore.

16. Dipole stabilizer rods for 400 keV deuteron RFQ, V.L.S Rao Sista, S.C.L. Srivastava, Rajni Pande, Shweta Roy, P. Singh, Ind. Particle Accelerator Conf. (InPAC-2009), 10-14 February, 2009, RRCAT, Indore.
17. Developmental Studies of High Current Proton Linac for ADS Program, P. Singh, S.V.L.S. Rao, Rajni Pande, Shweta Roy, Rajesh Kumar, Piyush Jain, P.K. Nema, S. Krishnagopal, R. K. Choudhury, S. Kailas, V.C. Sahni, International Topical Meeting on Nuclear Research Applications & Utilization of Accelerators, 4-8 May 09, Vienna, Austria.
18. Low energy proton linac development at BARC for ADS program, S.V.L.S.Rao, Rajni Pande, Shweta Roy, Piyush Jain, Rajesh Kumar, S. Krishnagopal, P. Singh, P.K. Nema, R.K. Choudhury, S. Kailas & V.C. Sahni, International Conference on Peaceful Uses of Atomic Energy-2009, Sept 29-Oct 1, 2009, New Delhi, Page 498.
19. High intensity accelerator development for ADS, P. Singh, Rajni Pande, Shweta Roy and S.V.L.S Rao, Indian Nuclear Society News, Vol. 6, No. 2 April-June 2009, p 21-29.

Rajni Pande

Dedicated to

My parents

(Dr. Padmakar Pande & Smt. Urmila Pande)

ACKNOWLEDGEMENTS

I take this opportunity to express my heartfelt gratitude to my guide Dr. Pitamber Singh for his constant motivation, support and cooperation throughout my PhD work. His constant encouragement and constructive criticism helped me at various stages of my work. He has been my true mentor and guide. I wholeheartedly thank him.

I would also like to express my sincere thanks to the members of my doctoral committee Drs S. Kailas, V.S Pandit and K.C Mittal for their support and valuable comments during this period. I gratefully acknowledge the invaluable advices given by Dr. V. S Pandit and the discussions I had with him. I would also like to thank Dr. S. Krishnagopal for various fruitful discussions.

I would like to extend a warm thanks to my friends and colleagues Shweta Roy, S V L S Rao, Tushima Basak, Puneet Jain, Piyush Jain, Jose Mathew, Shashi Srivastava and Sumit Garg for all their support and help. Thanks are also due to Shri. S.K. Gupta, Shri. Arun Agarwal and Shri. N.K. Prasad for various discussions on the fabrication of LEBT components. I am thankful to Shri. S.C. Bapna and the members of the Magnet Development Lab from RRCAT for their assistance in fabricating and testing of the solenoid magnets. I would also like to thank Manas Mishra, Praveen Parate, Laksman Tayade, Gireesh Singh, Prashant Gorule, N. J Koli, H. K Sane and Dalvi for their support and assistance during experiments. It is my pleasure to thank all staff members of IADD who have helped me in all possible ways.

This thesis would not have been possible without the love and support from my family. I would like to express my sincere gratitude to my parents for their constant love and support and for making me the person that I am today. They have been the greatest source of inspiration to me and have given me the motivation and encouragement to do my PhD. I thank them with all my heart. I thank my brother Arvind and his wife Neha for all their encouragement. I am thankful to my husband, Nakul Mudgal for his love, care, support, encouragement and understanding and finally to my little daughter, Aarushi for all her love and for the cheer and joy she brings into my life each day.

Contents

Page No.

SYNOPSIS

High-power proton accelerators have various applications such as accelerator-driven systems (ADS), spallation neutron sources, next-generation radioactive ion beam facilities, neutrino factories etc. Accelerator-driven systems have the capability to incinerate MA (minor actinides) and LLFP (long-lived fission products) radiotoxic waste and can also utilize thorium as nuclear fuel and produce energy without producing much long lived radioactive wastes. This is of particular interest to India due to the possibility of utilization of the vast Thorium resources in our country for nuclear power production. The ADS consists of a subcritical reactor that is driven by an external neutron source produced by a high-power proton beam hitting a high *Z* material and producing neutrons by spallation. The accelerator for ADS is required to deliver proton beam of up to 10 - 30 MW power and operate in the CW mode with high-intensity beams. In India, it is planned that the development of the 1 GeV accelerator for ADS will be pursued in three phases, namely, 20 MeV, 100 MeV and 1 GeV. One of the most challenging parts of such a CW proton accelerator is the low-energy injector, typically up to 10-20 MeV, because the space-charge effects are maximal at lower energies for high current beams. In order to understand these effects, in the first stage, a low energy high-intensity proton accelerator (LEHIPA) is being built in BARC, India as the front end injector to the Linac for ADS. This system will consist of an ECR ion source that will deliver a 50 keV proton beam followed a 3 MeV RFQ and an Alvarez Drift Tube Linac to accelerate the beam from 3 to 20 MeV. The Low Energy Beam Transport (LEBT) and the Medium Energy Beam Transport (MEBT) lines are used to transport and match the beam from the ion source to the RFQ and from the RFQ to the DTL respectively.

This thesis is based on the results of the design, development and characterization of LEBT systems and the physics design studies for high intensity proton linac. The work in this thesis is focused on two main parts: (i) the detailed simulation studies for the LEBT line for LEHIPA and measurements made on a

LEBT test bench with helium, deuteron and proton beams and (ii) Design studies for a 30 mA, 1 GeV proton linac. The thesis is organized in six chapters. In the first chapter, a brief introduction on the high intensity proton linac is presented. It discusses about the possible acceleration configurations for an accelerator for ADS, the design issues for such accelerators and a review of other high intensity accelerator projects in the world.

Chapter 2 discusses the design and development of the LEHIPA LEBT. The LEBT system is used to transport and match the beam from the ion source into the RFQ with minimum emittance growth and loss of beam current. With this criterion, a magnetic LEBT line using two solenoids for focussing and matching the beam has been designed to match a 50 keV, 30 mA proton beam from ECR ion source to the RFQ. The LEBT is about 3m long and its functions include beam focusing and steering at the RFQ match point, dc beam current diagnosis and beam profile measurement through CCD monitors. The LEBT also has a water-cooled collimator and an electron trap at the RFQ entrance. Simulations were also done using the analytical KV beam envelope equations to compare the results from the code. The results were found to be similar. The beam to be transported through the LEBT is a 30 mA, 50 keV proton beam. Space charge effects are most severe for such high currents at low energies leading to increase in beam size and emittance. In the LEBT, space charge compensation facilitates the transport of high current beams and reduces emittance growth due to space charge forces. Space charge compensation is done by introducing a residual gas in the LEBT at low pressure. Due to ionization of the residual gas atoms, electrons and slow ions are created inside the beam. The slow ions are repelled radially outward from the beam while the electrons are trapped by the beam potential and remain in the beam. So the effective space charge of the beam is gradually reduced until it reaches a stationary degree of compensation. Simulations were also carried out to study the effects of space charge compensation in the LEBT which show that as the degree of space charge compensation increases, the transverse beam sizes as well as the emittances come down.

Based on the beam dynamics simulations, the two solenoids for LEHIPA were designed for a maximum peak field 3.5 kG and effective length of 30 cm. The solenoid design was done in POISSON. A 3 cm thick core made of magnetic material is used to increase the magnetic field of the solenoid by providing a low resistance path to the magnetic flux lines, with a lower value of current in the solenoid coils. Based on this design the solenoids were fabricated and tested. The results were in good agreement with the simulations.

The beam coming from the ion source contains H_2^+ and H_3^+ ions in addition to the H^+ ions. There are also electrons trapped in the beam due to space charge compensation in the LEBT. All these have to be removed before entering the RFQ. The H_2^+ and H_3^+ ions, having a greater momentum than proton are less focused by the solenoids and hence can be cut off by putting a collimator just before RFQ entrance. In addition, an electron trap is needed to prevent the electrons from the neutralized beam to enter the RFQ. The electron trap is a ring with a negative 1-2 kV potential placed at the entrance of the RFQ through which the beam passes. The potential from this ring prevents low-energy plasma electrons from going through it, but not the protons at 50 keV. This electron trap for LEHIPA has been designed for a potential of -1.5 kV in POISSON. A magnetic steerer has also been designed for steering the 50 keV proton beam into the RFQ. The requirement is beam steering of ±3 cm in horizontal and vertical directions from the axis of the beamline at a distance of 75 cm from the entrance of the steering magnet. The steering magnet has been designed using POISSON.

Characterization of beams through a LEBT test bench setup at BARC has been discussed in Chapter 3 of the thesis. A 400 keV, 1 mA deuteron RFQ has been built at BARC to be used as a neutron generator. The accelerator system consists of a rf ion source, a 400 keV RFQ and a low energy beam transport line to match the beam from the ion source to the RFQ. This LEBT has been designed using 2 solenoids for focusing the beam. Based on the simulations, a LEBT test bench was setup at Van de Graaff Laboratory to validate the simulations. The test bench consisted of an Alphatross ion source, Einzel lens, accelerating tube and 2 solenoids. There were

2 Faraday cups and 2 BPM's in the line to measure the beam current and size. The LEBT test bench is shown in Fig.1. He^+, D^+ and H^+ beam have been extracted from the ion source and accelerated to 50 keV using the dc accelerating tube. This 50 keV beam is then focused with the help of the 2 solenoids in the LEBT line. Experiments to measure the beam emittance of the beams in the line using solenoid scan method and slit wire method were done. In the solenoid scan method, the beam size is measured as a function of the solenoid field. The RMS transverse emittance was then calculated by a least square fitting of the square of the beamsize as a function of the solenoid focusing strength which turns out to be a parabola. The emittance measurement setup for the slit wire method consists of movable slits of 0.35 mm width and movable thin wire of 0.05 mm diameter. The spatial beam distribution is scanned by the slit while the angular distribution is scanned by the wire scanner located at a distance of 140 mm downstream the beam line. A 1 μm precision linear motion mechanism is provided for the slit and wire holders. The beam emittances in both the transverse directions are measured in a simultaneously using this setup. The measured emittances were found to be well within the acceptance of the RFQ and the LEBT line was coupled to the RFQ. H^+ and H_2^+ beams were transported through the LEBT and matched to the RFQ. These beams have been successfully accelerated by the RFQ.

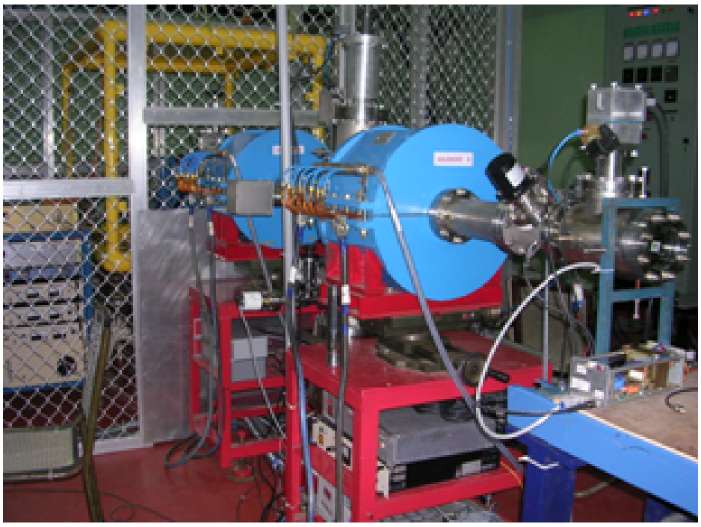

Fig.1. LEBT Test bench.

In Chapter 4, the detailed design studies for a 1 GeV proton linac have been presented. The high-power linac essentially consists of low-energy, the intermediate-energy and the high-energy sections. The low-energy section consists of a high-intensity ion source that delivers beams of few tens of keV energy. Almost all linacs being designed today use the radio-frequency quadrupole (RFQ) to accelerate the high current beam from the ion source to a few MeV beam energy. The intermediate-energy structures accelerate the beam to about 100 MeV. These are usually normal-conducting drift-tube Linac structures (DTL, SDTL, CCDTL). However, superconducting structures, like spoke type resonators and half wave resonators, are also being contemplated especially for CW beams. The high energy structures accelerate the beams from few hundred MeV to GeV energies. At these energies, superconducting RF technology seems to be the best option in order to design a cost-effective machine in terms of both capital and operational costs and superconducting multicell elliptical cavities are used for acceleration in this energy range.

An accelerator configuration for a 1 GeV, 30 mA linac has been worked out and the physics design studies have been done in detail. The main design criterions for such a linac are:

- Low beam loss (<1 Watt/m) to allow hands-on-maintenance of the entire linac
- Low emittance increase
- Minimize halo formation

For this, the following design philosophy was adopted

- Maintaining the transverse and longitudinal phase advances per unit length constant at all transitions between the structures to provide a current independent match into the next structure. For this the quadrupole gradients and accelerating electric fields are varied between the structures.
- Matching the transverse and longitudinal phase spaces at the end of one structure to the acceptance of the next structure by using carefully designed transport lines.

- Keeping the zero current phase advance per period (σ_0) in all the planes below 90 degrees. This is done to avoid envelope instability which causes emittance increase and beam loss.

The design studies involved choice and optimization of various accelerating structures and the beam dynamics studies through the linac. The designed linac consists of a 50 keV ion source, a four-vane 3 MeV Radio Frequency Quadrupole (RFQ), Drift Tube Linac (DTL) upto 40 MeV, Cavity Coupled DTL (CCDTL) upto 100 MeV and 5 cell Superconducting elliptical cavities to accelerate the beam to 1 GeV. The RFQ and DTL operate at 352.21 MHz and the CCDTL and SC Linac operate at the second harmonic frequency at 704.42 MHz. A FFDD lattice is used in the DTL while FD lattice is used in the CCDTL for transverse focusing. The SC cavities are designed to perform over the given velocity range and are identified by a design velocity called the geometric velocity, $\beta_{G.}$ This design approach takes advantage of the large velocity acceptance of the superconducting cavities. The superconducting linac accelerates the beam using three different types of 5-cell elliptical cavities designed corresponding to geometric beta values β_G = 0.49, 0.62 and 0.80. The transverse focusing is achieved by using room temperature electromagnetic quadrupole doublets in between the cryomodules containing the superconducting cavities. The total length of the designed accelerator is about 380 m and the overall transmission is about 96%. The 4% loss takes place in RFQ during bunching of the beam which is not expected to pose any radiation problem. The variation of maximum beam size with energy is shown in Fig. 2. The aperture is 10-12 times the rms beam size in the normal conducting linac and more than 16 times the rms beam size in the superconducting linac where the risk of activation due to beam loss is more.

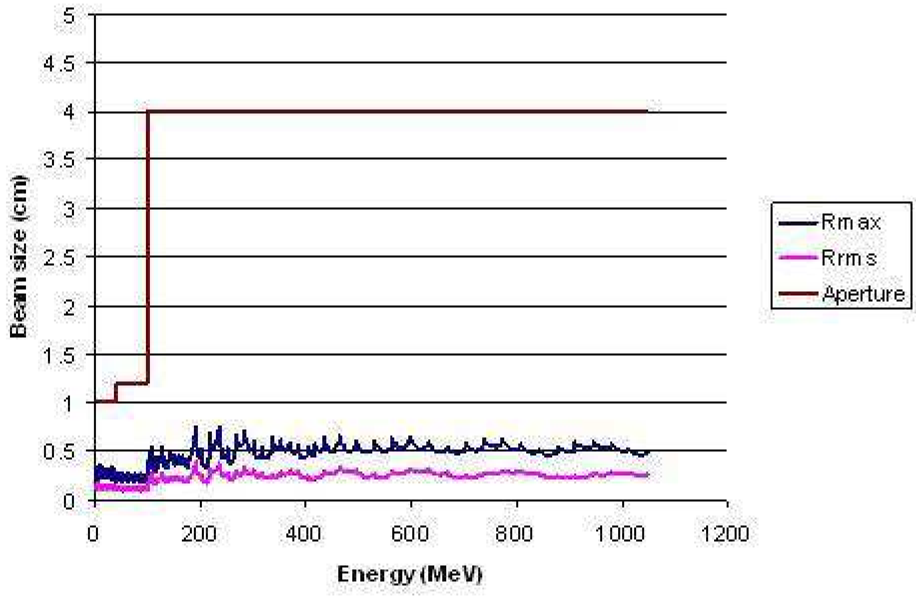

Fig.2. Variation of beam size with energy in the Linac.

Superconducting structures offer several advantages over normal conducting structures particularly for CW operation due to very low RF losses in the cavity. Hence, in view of advances in the superconducting technology and new structures being developed for use in the medium energy range, it has been planned to go for superconducting structures right after the RFQ for the 1 GeV linac for ADS. Two types of structures are now being considered as options for acceleration after the RFQ: the HWR at 162.5 MHz and the SSR at 325 MHz. Both these cavities are TEM class coaxial half wave structures. While in the half wave resonator the inner spoke conductor is along the axis of the cavity, in the spoke resonator, it is perpendicular to it. The 3D electromagnetic designs for these structures have been done using CST Microwave Studio. The main design criterion for theses structures is to minimize the peak surface electric and magnetic fields. The results of these studies are discussed in Chapter 5 of the thesis.

Chapter 6 summarizes the present work in the thesis. It also discusses the future scope of work in the vast field of high current accelerator design.

References:

1. F Carminati, R Klapisch, J P Revol, J A Rubio and C Rubbia, CERN/AT/93-47(ET)
2. S S Kapoor, Roadmap for development of accelerator-driven sub-critical reactor systems, BARC/2001/R/004.
3. P. Singh, S.V.L.S. Rao, Rajni Pande, T. Basak, Shweta Roy, M. Aslam, P. Jain, S.C.L. Srivastava, Rajesh Kumar, P.K. Nema, S. Kailas and V.C. Sahni, Accelerator Development in India for ADS Programme, Pramana – J. Phys. **68**, 33 (2007).
4. T. P. Wangler, Principles of RF Linaear Accelerators, John Wiley & Sons, INC, 1998.
5. H Padamsee *et al*, *RF superconductivity for accelerators*, Cornell University, Ithaca, New York (Wiley-Interscience Publication, 1998)
6. J H Billen and L M Young, POISSON SUPERFISH, LA-UR-96-1834, L.A.N.L. K.R.
7. Crandall, TRACE 3D Documentation, Third edition Los Alamos Report LA-UR-97-886, May 1997
8. J H Billen, *PARMILA* Code, LA-UR-98-4478, Revised July 26, 2005
9. C Pagani et al, Design criteria for elliptical cavities, SRF, 2001.
10. Rajni Pande, Shweta Roy, S V L S Rao, P Singh and S Kailas, Physics design of a CW high-power proton LINAC for ADS, Pramana – journal of Phys., **78**, 247, 2012.
11. K. Shepard *et al.*, “Development of Niobium Spoke Cavities for a Superconducting Light-Ion Linac”, Proceedings of the XIX International Linac Conference, Chicago Illinois, p. 956.

List of Figures

List of Tables

CHAPTER 1

Introduction

1.1 Introduction

High-power proton accelerators have various applications such as accelerator-driven systems (ADS), spallation neutron sources, next-generation radioactive ion beam facilities, neutrino factories etc. In particular, accelerator driven systems [1] have evoked considerable interest in the nuclear community around the world because of their capability to incinerate the MA (minor actinides) and LLFP (long-lived fission products) radiotoxic waste and utilization of Thorium as an alternative nuclear fuel. In the Indian context, due to our vast thorium resources, ADS is particularly important as one of the potential routes for accelerated thorium utilization and the closure of the fuel cycle [2]. The ADS consists of a subcritical reactor that is driven by an external neutron source produced by a high-power proton beam produced in an accelerator striking on a high Z material and producing neutrons by spallation. The accelerator for ADS is required to deliver proton beam of up to 10 - 30 MW power and operate in the CW mode with high-intensity beams.

While many efforts are on around the world for developing high energy and high current proton accelerators for ADS, at present no such linac is yet operating anywhere in the world. Since the linac is for ADS applications, the CW mode of operation is essential in order to prevent thermal shocks to the target which is undesirable. There is no experience worldwide in making and operating proton linacs in CW mode at 1 GeV, which makes the design of the ADS linac particularly challenging.

1.2 Accelerator driven systems

With increasing population and industrialization, the energy requirement in the world including that from electricity generation is rapidly growing. Most energy requirements today are met by burning fossil fuel and hydroelectricity generation. Nuclear power appears to be an attractive option for clean electricity generation and presently constitutes about 17% of the total electric power generation in the world. Presently, fission chain reaction is the only way known to harness nuclear energy, while the naturally occurring uranium and the man-made plutonium are the two key elements that are serving as nuclear fuel. Accelerator Driven Systems offer an attractive option of utilization of Thorium as an alternative nuclear fuel in addition to their capability to incinerate the MA (minor actinides) and LLFP (long-lived fission products) radiotoxic waste.

In an ADS system, a high-energy proton beam from an accelerator strikes a high Z element (e.g.; Pb, W, U, Th etc..) target which yields copious neutrons by spallation reaction. Around 20–30 neutrons are produced per incident proton. These neutrons are then used to drive a sub critical reactor and produce power which is used for generation of electricity. An important parameter in the ADS design is the spallation ratio i.e. number of neutrons produced per GW spent or number of neutrons per incident charged particle on the target. The spallation ratio increases with the proton energy above 100 MeV and saturates at around 1 GeV as can be seen from Fig.1.1. Hence the optimum energy of the accelerator is 1 GeV because beyond that there is very little increase in the no. of neutrons per unit beam power.

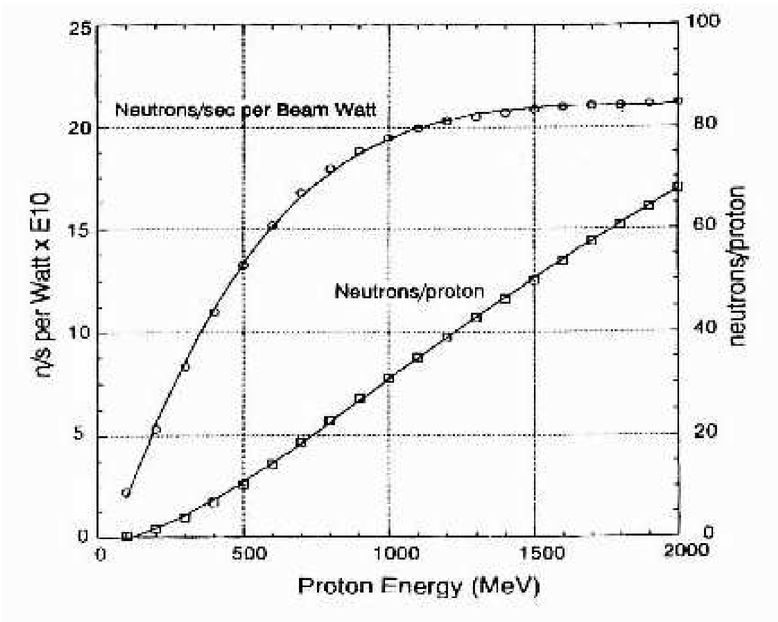

Fig.1.1: Variation of n/sec per unit incident beam power with proton beam energy.

The thermal power output from an ADS reactor is given by

$$P_{thermal}(MW) = E_{fission}(MeV) I(A) \frac{\nu_s}{\nu} \frac{k}{1-k}$$

Where,

$E_{fission}$ is the energy released per fission, I is the proton beam current, ν_s is the number of spallation neutrons released from the spallation target per incident proton, ν is the number of neutrons released per fission and k is the effective neutron multiplication factor.

Then, for

Proton Energy = 1 GeV, ν_s = 25 neutrons/proton, ν = 2.5 neutrons/fission

$P_{thermal}$ = 1500 MW (for 500 MW electrical) and k=0.95, the beam current requirement, calculated from the relation, comes out to be ~ 44 mA. Thus the beam current requirement from the proton accelerator is of the order of tens of mA.

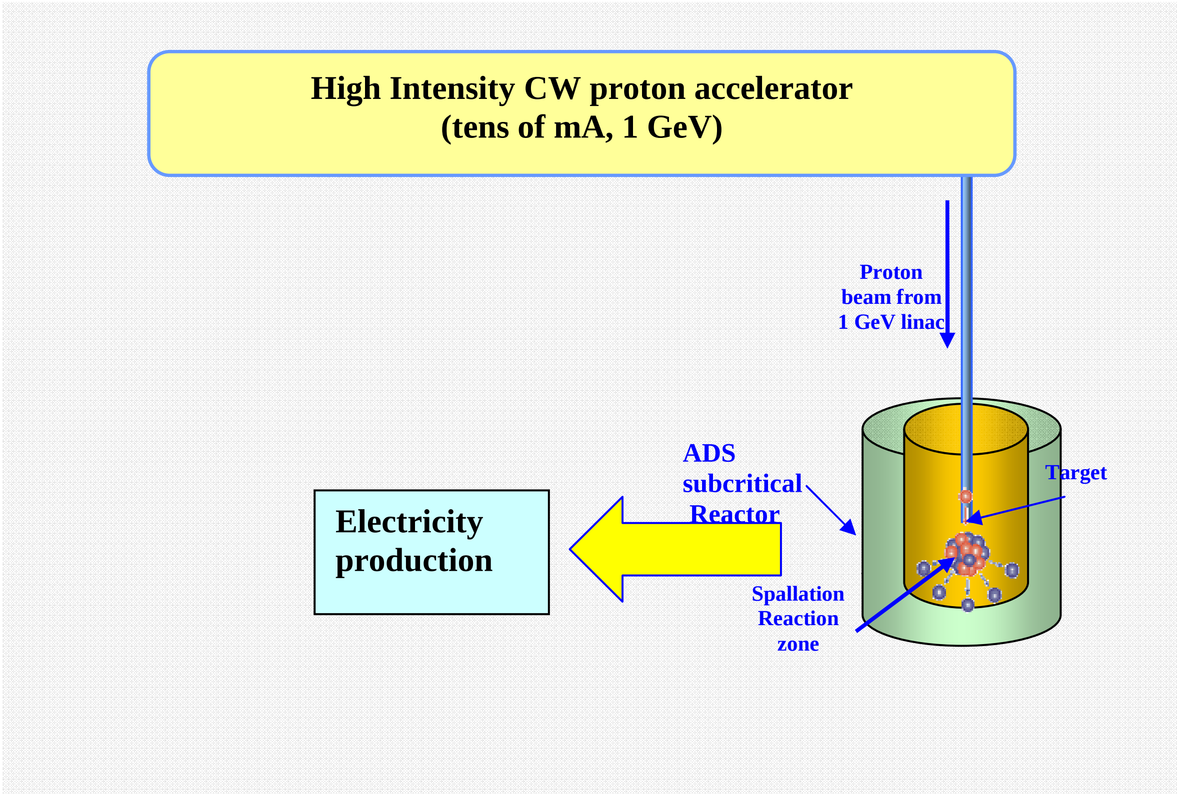

Fig 1.2: Schematic of an ADS system.

The schematic of an ADS system is shown in Fig. 1.2. The major sub-systems of ADS are:

1. High power proton accelerator - 1 GeV energy, tens of mA beam current.
2. Spallation target – Made of heavy element (Pb, W, U, Pb-Bi eutectic…).
3. Sub-critical Reactor core – A fast neutron system, thermal neutron system or a combination of fast and thermal neutron systems.

For accelerator driven systems it is necessary that the accelerator is reliable, rugged and stable with very low number of beam interruptions, which could affect the lifetime of key components such as windows, reactor parts and structure, as well as the ADS operation.

1.3 Accelerator for ADS

Linacs and Cyclotrons were the two options considered for the accelerator subsystem of the ADS in the beginning. A cyclotrons by its intrinsic design operates in CW mode and is compact and cheaper to build, but is limited by the maximum proton current that it can accelerate which is only a few mAs where as the required beam current is a order of magnitude higher. Linacs on the other hand can accelerate higher beam currents to high energy. Hence the linac option is now being considered worldwide.

The accelerator for ADS must meet the following requirements [3]:

- The accelerator must deliver 1 GeV energy proton beam of current ≥ ~10 mA.
- Robust and reliable for round the year uninterrupted operation i.e, its availability~100%.
- Operational with minimum beam loss in accelerator channel for limiting activation of components and their hands-on maintenance. (Beam loss <~1 nA/m of particle trajectory).
- Have high (electrical) conversion efficiency from mains to beam power.

A typical ~1 GeV proton linac in MW average power range consists of three main sections:

1.3.1 Low energy section

The kinetic energy of the particles from an ion source is about a few tens of keV. These particles are accelerated by a pre-accelerator, which can be either a Cockcroft-Walton or Radio Frequency Quadrupole (RFQ) linac. The former has been in use for many years and has a maximum energy of about 750 keV. Almost in all laboratories it has now been replaced by the RFQ, which is a common choice for low energy accelerators. This is because an RFQ [4, 5] can accelerate beams to energies of few MeVs with much smaller physical size. It can accept dc beam and bunch it with very high efficiency (>90%) eliminating the need for an external buncher where the bunching efficiency is very low. The RFQ simultaneously bunches, focuses and accelerates the beams using RF fields and maintaining good beam quality of the high intensity beam at the same time.

1.3.2 Medium Energy section

Intermediate-velocity structures accelerate beam to about 100-200 MeV in the range $\beta \sim 0.1$ to 0.5. These structures are usually normal-conducting drift-tube linac structures (DTL, SDTL, CCDTL). However, superconducting structures, as spoke type resonators, are being contemplated especially for CW beams. At low energies, the Alvarez DTL is the widely used structure. The conventional Alvarez type DTL structure is however expensive to build due of its large dimensions and the accurate alignment required for mounting the drift tubes. The magnets inside the drift tubes for focusing at the low energy end of the DTL are difficult to make because of the smaller drift tube lengths at these energies. However, for a high-intensity linac where beam optics has to be smooth, the choice of the conventional Alvarez DTL is unavoidable at low energy because of its short focusing periods. When the beam energy exceeds a few tens of MeV, the focusing period can become longer, and alternative structures like CCDTL, SDTL etc can be considered [6]. Different alternatives to the DTL have been developed, all relying on the principle of separating the focusing from the RF structure, with the quadrupoles placed between the accelerating tanks. Some of these structures are based on TE mode operation like the IH-DTL [7] and CH-DTL [8], which provide a high shunt impedance, but require relatively long tanks and unconventional beam optics solutions that are difficult to apply for high intensity operation due to the longer focusing periods. Other structures are based on the TM_{010} mode for operation, using shorter DTL tanks containing drift tubes of smaller diameter with quadrupoles placed between the tanks. Since these structures do not have magnet inside the drift tubes, the drift tubes can be smaller resulting in higher shunt impedances. But they also have increased losses due to a higher number of cavity end walls, thus arriving at similar shunt impedance values to conventional DTL. Some examples are Separated DTL

(SDTL) where the accelerating tanks are decoupled from each other, and of Cell-Coupled DTL (CCDTL) when the tanks are coupled together via coupling cells, forming a single resonator. The CCDTL was originally developed at Los Alamos at a frequency of 805 MHz [9].

1.3.3 High energy section

High-velocity structures accelerate beam from few hundred MeV upto GeV energies and consist of normal-conducting coupled-cavity linac structures (CCL) or of superconducting cavities that offer some advantages such as higher gradient capabilities and lower operation costs. The CCL is an established technology and has been used in most of the existing linacs (e.g., Fermilab, Los Alamos National Laboratory, Brookhaven National Laboratory, etc.). The highest energy, using this technology, reaches 800 MeV at LANSCE [10] at Los Alamos. However, the recent times, projects like SNS [11] are using SC linac for the advantages that it offers. SC linacs have been proved reliable and efficient in electron machines (e.g., LEP and CEBAF). However, employing it for proton machines is still a challenge due to the varying β values of the proton beam at these energies. Compared with a room temperature linac, an SC linac has the following advantages:

1. Higher accelerating gradient.
2. Larger aperture (which is particularly important for high intensity beams).
3. Lower operation cost.
4. Lower capital cost if higher energy is required.

1.4. Technical challenges

The most-challenging engineering task for high-current cw normal-conducting accelerators is thermal management. Large amount of power is dissipated on the walls and other internal surfaces of normal conducting structures that are significantly increased by CW operation and high accelerating gradients. If not cooled, the cavity can get detuned and the RF power will be deflected back. The cooling demands for precision resonance control in the cavity typically require cavity temperature regulation to 0.1 °C or better.

Another important concern in building such high-power linacs is the minimization of beam losses (typically less than 1 nA/m of particle trajectory), which could limit the availability and maintainability of the linac and various subsystems due to excessive activation of the machine. A careful beam dynamics design is therefore needed to avoid the formation of beam halo that would finally be lost in the linac or in transfer lines.

Though a high acceleration gradient is desired in order to reduce the linac length, the longitudinal beam dynamic issues, together with the need of limiting the power transferred by the coupler to the high current (tens of mA) beam and the CW RF cryogenic losses, make it challenging to achieve higher gradients.

1.5. High Power Accelerator development Programmes: International scenario

Most of the existing operating proton linacs are injectors for large synchrotrons, and are short pulse, low-duty-factor machines with relatively low average beam current and power. The major exception is the LANSCE linac at Los Alamos, an 800 MeV accelerator that can deliver an average beam power exceeding 1 MW, with a peak current of about 20 mA, a duty factor of up to 10%, and macropulses 0.5-1.0 ms long. There are a number of high intensity proton sources operating at various laboratories over the world. The SNS at the Oak Ridge National Laboratory in the U.S is a linac-based spallation neutron source. The SNS SC cavities have been designed using maximum accelerating gradients upto 24.4 MV/m. The design beam energy is 1 GeV, beam power 1.4 MW. The European Spallation Source (ESS) [12] specifies a 1.33 GeV H- linac delivering a beam power of up to 5 MW in 2 ms pulses, with a peak current of about 100 mA. High-power linacs for tritium production were designed in the USA and France in the 1990s. The linac designed at Los Alamos for the Accelerator Production of Tritium (APT) project was initially a

100 mA CW, 1700 MeV accelerator consisting of an Alvarez-type drift tube linac (DTL) up to 200 MeV, followed by a LANSCE-style side-coupled linac to the full beam energy. However, with advances in SC linac technology, the final design for the APT accelerator [13], assumed a SC linac from 211.4 MeV to 1030 MeV, with the NC technology applied only to the low-energy section of the linac. The SC-cavity design gradient was 5 MV/m, which allowed a much shorter machine than the original all-NC design, as well as one that was electrically significantly more efficient. However, as a result of recent progress in SC elliptical cavity performance, resulting from better niobium material and improved surface preparation techniques, cavity accelerating gradients of more than 10 -15 MV/m can now be assumed, with Q values of better than 1×10^{10}.

European R&D for ADS design and fuel development is driven by the EUROTRANS Programme [14]. In EUROTRANS, two ADS design routes are followed, the XT-ADS and the EFIT. The XT-ADS is designed to provide the experimental demonstration of transmutation. The EFIT, the European Facility for Industrial Transmutation, aims at a conceptual design of a full transmuter. The proposed reference design for the XADS (Experimental Accelerator driven System) accelerator (600 MeV, 6 mA) consists of a proton injector (ECR source + normal conducting RFQ structure) followed by normal conducting IH-DTL or/and superconducting CH-DTL up to a transition energy from where on a fully modular superconducting linac brings the beam up to the final energy [15]. For MYRRHA, an ADS demonstration project in Belgium, a 600 MeV, 2.5 mA linac is under development [16].

JAERI at Japan has been proposing the Neutron Science Project [17] which aims at the construction of the world’s most powerful spallation neutron source and related research facility complex to enhance basic sciences and ADS development. The JHF at KEK/JAERI is a synchrotron-based facility. It has a 400 MeV NC linac, a 600 MeV SC linac to boost the energy from 400 MeV to 600 MeV, a 3 GeV rapid cycling synchrotron with a beam power of 1 MW, and a 50 GeV slow ramp synchrotron with a beam power of 0.75 MW. The major facilities would be a superconducting proton linac, a 5-MW target station allowing neutron pulses for neutron scattering research, and research facilities for ADS experiments, neutron physics, materials irradiation, and Spallation radioactive ion (RI) beam production for exotic nuclei science. Japanese ADS application programme is named OMEGA (Option Making Extra Gains of Actinides and FP). This is conversion of their critical reactor project Actinides Burner Reactor (ABR) into ADS. The 600 MeV linac will be used for R&D to drive the ADS facility.

Korea Atomic Energy Research Institute (KAERI) was involved in a project named KOMAC (Korea Multi-purpose Accelerator Complex)[18]. The final objective of KOMAC is to build a 20-MW (1 GeV, 20 mA) cw proton linear accelerator. A 100 MeV proton accelerator project has been taken up as PEFP (proton engineering frontier project). The goal of the first phase of the project is to develop a high duty cycle 20 MeV accelerator.

In China, a multipurpose verification system as a first phase of their ADS programme consists of a low energy accelerator (150 MeV, 3 mA proton LINAC). China Institute of Atomic Energy (CIAE), Institute of High Energy Physics (IHEP) and Institute of Heavy Ion Physics in Peking University (PKUIHIP) are jointly carrying on the R/D of the proposed accelerator. Some R&D, such as ECR high current ion source development, RFQ design and technology study, superconducting cavity study, conceptual design of 150 MeV, 3 mA proton LINAC, preliminary design of 1 GeV, 20 mA LINAC and intense beam physics have started. [19]

In Russia, ITEP is pursuing a programme for experimental demonstration of ADS (XADS) [20]. This hybrid electronuclear facility of moderate power integrates the pulse proton linac (36 MeV, 0.5 mA) and subcritical blanket assembly (heat power of 100 kW). The 36 MeV proton linac ISTRA-36 with the average current of 500 μA will be used as a driver. It will deliver proton beam pulses of 100 mA of 220 μs duration with a repetition rate of 25 pps The linac consists of the 82 keV injector, 3 MeV, 150 MHz RFQ, 10 MeV, 300 MHz DTL-1 section, LEBT , a 36 MeV, 300 MHz DTL-2 section and HEBT.

Prototypes of 100% duty proton injectors with output current > 100 mA have been successfully tested at Los Alamos (LEDA) and CNRS/CEA (IPHI) collaboration [21,22]. Both injectors employ microwave-driven ion sources of similar design, and both use solenoid lenses in the low-energy beam transport to the RFQ, with nearly complete space-charge neutralization from trapped electrons. Measured output emittance values are about 0.2 mm-mrad at 100 mA. The LEDA injector operating voltage is 100 kV, while the IPHI injector voltage is 80 kV.

1.6 Accelerator development for Indian ADS Programme

In 2000, an ADS Coordination Committee at BARC, chaired by Dr.S.S.Kapoor studied various scientific and technological issues connected with development and application of ADS systems in the country and prepared a report thereon [23]. It is planned that the development of the 1 GeV accelerator for ADS will be pursued in three phases, namely, 20 MeV, 100-200 MeV and 1 GeV. Phase I is the development of a 30 mA, 20 MeV room temperature linac. Phase II, which is the development of the medium energy linac up to energies of 100-200 MeV could be normal conducting or superconducting depending on the progress of superconducting technology for structures in this energy range. This phase has now been modified, in view of good progress in development of structures like the superconducting spoke resonators. It is now planned to go for superconducting linac right after the RFQ at 3 MeV. The third phase, which is the development of the high energy linac upto 1 GeV is superconducting based on multicell elliptical cavities. The road map of the Indian ADS programme is shown in Fig. 1.4.

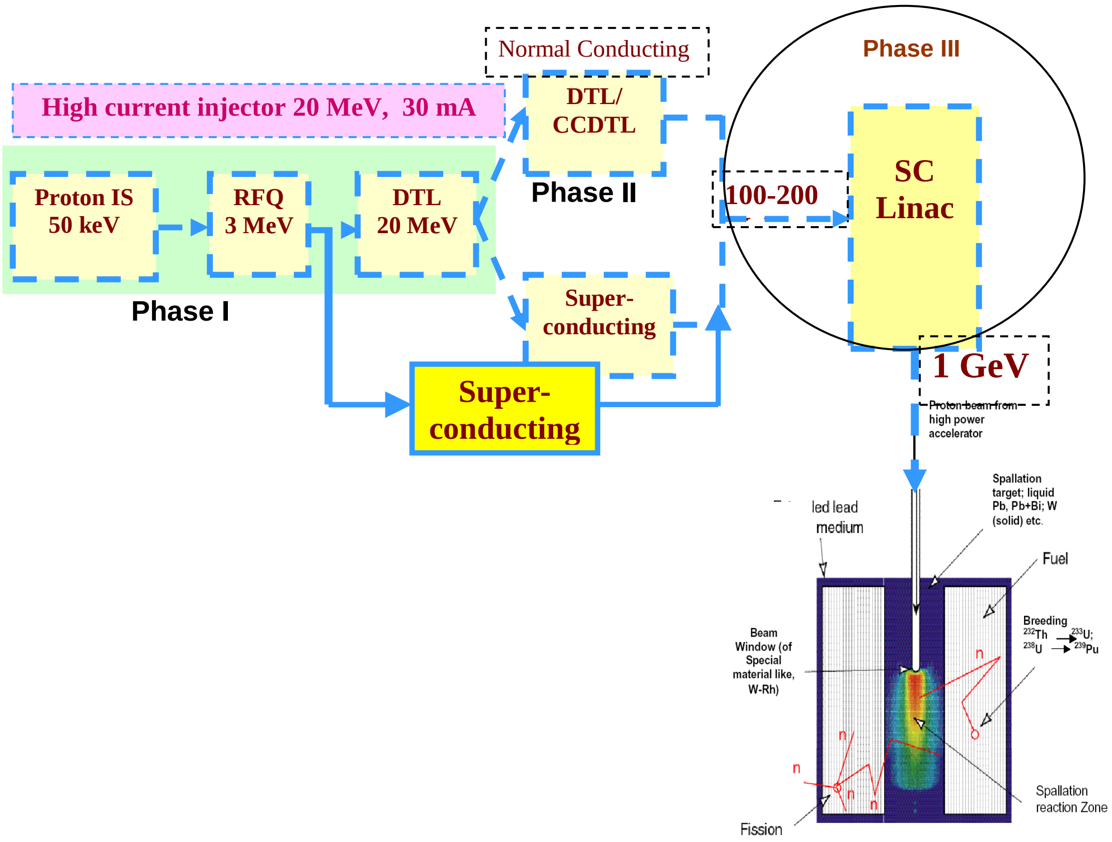

Fig. 1.3: Roadmap for Indian ADS Programme.

One of the most challenging parts of such a CW proton accelerator is the low-energy injector, typically up to 10-20 MeV, because the space-charge effects are maximal at lower energies. With this challenge in mind, a low energy (20 MeV) high intensity (30 mA) proton accelerator (LEHIPA) is being built at BARC [24] as a front-end injector for the 1 GeV linac for ADS. The major components of LEHIPA are a 50 keV ECR ion source, a 3 MeV RFQ and a 20 MeV DTL. The Low Energy Beam Transport (LEBT) and Medium Energy Beam Transport (MEBT) lines will transport and match the beam from the ion source to the RFQ and from the RFQ to the DTL respectively/ The layout of LEHIPA is shown in Fig.1.4.

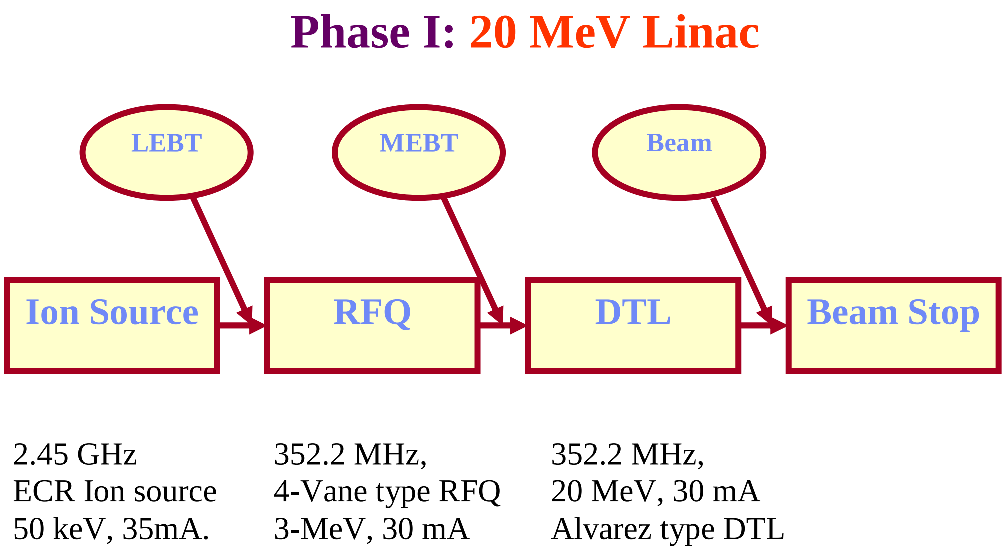

Fig. 1.4: Layout of LEHIPA.

For the next phase, an accelerator configuration for a 1 GeV, 30 mA linac with normal conducting structures in the medium energy part, has been worked out and the physics design studies have been done in detail [25]. It consists of a 50 keV ion source [26], 4 vane 3 MeV Radio Frequency Quadrupole (RFQ), Drift Tube Linac (DTL) upto 40 MeV, Cavity Coupled DTL (CCDTL) upto 100 MeV and 5 cell Superconducting elliptical cavities to accelerate the beam to 1 GeV. Another configuration using superconducting structures like spoke resonators at intermediate energies is being worked out.

This linac will have various applications at different stages. The ECR ion source can be used for ion-implantation. The RFQ (~ 3 MeV, >10 mA cw) can be used for: (i) Boron neutron-capture therapy (BNCT), (ii) Neutron radiography, and (iii) Detection of mines and explosives. The DTL (20 MeV) can be used for: (i) Medical radioisotope production, (ii) Small scale transmutation experiments, (iii) intense neutron (with Be, Li targets) source for fusion reactor material testing. At 100 MeV and above the proton beam can be used for RIB production.

1.7 Outline of the thesis

This thesis is based on the results of the design, development and characterization of LEBT systems and the physics design studies for high intensity proton linac. The work in this thesis is focused on two main parts: (i) the detailed simulation studies for the LEBT line for LEHIPA and measurements made on a LEBT test bench with helium, deuteron and proton beams and (ii) Design studies for a 30 mA, 1 GeV proton linac. The thesis is organized in six chapters. In this chapter, a brief introduction on the high intensity proton linac is presented. It discusses about the possible acceleration configurations for an accelerator for ADS, the design issues for such accelerators and a review of other high intensity accelerator projects in the world.

Chapter 2 discusses the design and development of the LEHIPA LEBT. The LEBT system is used to transport and match the beam from the ion source into the RFQ with minimum emittance growth and loss of beam current. With this criterion, a magnetic LEBT line using two solenoids for focussing and matching the beam has been designed to match a 50 keV, 30 mA proton beam from ECR ion source to the RFQ. The beam to be transported through the LEBT is a 30 mA, 50 keV proton beam. Space charge effects are most severe for such high currents at low energies leading to increase in beam size and emittance. In the LEBT, space charge compensation facilitates the transport of high current beams and reduces emittance growth due to space charge forces. Simulations were also carried out to study the effects of space charge compensation in the LEBT which show that as the degree of space charge compensation increases, the transverse beam sizes as well as the emittances come down. Based on the beam dynamics simulations, the two solenoids for LEHIPA were designed for a maximum peak field 3.5 kG and effective length of 30 cm. Based on this design the solenoids were fabricated and tested. The results were in good agreement with the simulations. An electron trap is needed at the end of the LEBT to prevent the electrons from the neutralized beam to enter the RFQ. This electron trap for LEHIPA has been designed for a potential of -1.5 kV in POISSON. A magnetic steerer has also been designed for steering the 50 keV proton beam into the RFQ.

Characterization of beams through a LEBT test bench setup at BARC has been discussed in Chapter 3 of the thesis. A 400 keV, 1 mA deuteron RFQ has been built at BARC to be used as a neutron generator. The accelerator system consists of a rf ion source, a 400 keV RFQ and a low energy beam transport line to match the beam from the ion source to the RFQ. This LEBT has been designed using 2 solenoids for focusing the beam. Based on the simulations, a LEBT test bench was setup at Van de Graaff Laboratory to validate the simulations. He^+, D^+ and H^+ beam have been extracted from the ion source and accelerated to 50 keV using the dc accelerating tube. This 50 keV beam is then focused with the help of the 2 solenoids in the LEBT line. Experiments to measure the beam emittance of the beams in the line using solenoid scan method and slit wire method were done.

In Chapter 4, the detailed design studies for a 1 GeV proton linac have been presented. The low-energy section of the linac consists of a high-intensity ion source that delivers beams of few tens of keV energy. Almost all linacs being designed today use the radio-frequency quadrupole (RFQ) to accelerate the high current beam from the ion source to a few MeV beam energy. The intermediate-energy structures accelerate the beam to about 100 MeV. These are usually normal-conducting drift-tube Linac structures (DTL, SDTL, CCDTL). However, superconducting structures, like spoke type resonators and half wave resonators, are also being contemplated especially for CW beams. The high energy structures accelerate the beams from few hundred MeV to GeV energies. At these energies, superconducting RF technology seems to be the best option in order to design a cost-effective machine in terms of both capital and operational costs and superconducting multicell elliptical cavities are used for acceleration in this energy range. An accelerator configuration for a 1 GeV, 30 mA linac has been worked out and the physics design studies have been done in detail. The design studies involved choice and optimization of various accelerating structures and the beam dynamics studies through the linac.

Superconducting structures offer several advantages over normal conducting structures particularly for CW operation due to very low RF losses in the cavity. Hence, in view of advances in the superconducting technology and new structures being developed for use in the medium energy range, it has been planned to go for superconducting structures right after the RFQ for the 1 GeV linac for ADS. Two types of structures are now being considered as options for acceleration after the RFQ: the HWR at 162.5 MHz and the SSR at 325 MHz. Both these cavities are TEM class coaxial half wave structures. While in the half wave resonator the inner spoke conductor is along the axis of the cavity, in the spoke resonator, it is perpendicular to it. The 3 D electromagnetic designs for these structures have been done using CST Microwave Studio. The main design criterion for theses structures is to minimize the peak surface electric and magnetic fields. The results of these studies are discussed in Chapter 5 of the thesis.

Chapter 6 summarizes the present work in the thesis. It also discusses the future scope of work in the vast field of high current accelerator design.

CHAPTER 2

Design of the Low Energy Beam Transport line for LEHIPA

2.1 Introduction

A 20 MeV, 30 mA proton linac is being built at BARC as a front end injector to the proton linac for ADS [24]. This linac will consist of an ECR ion source which will provide 30 mA proton beam at 50 keV. This beam is then accelerated to 3 MeV using a four vane RFQ and further to 20 MeV using an Alvarez DTL. The two transport lines, Low Energy Beam Transport (LEBT) and Medium Energy Beam Transport (MEBT) will be used to match and transport the beam from the ion source to the RFQ and from the RFQ to the DTL respectively. The beam quality and transmission through the RFQ is very sensitive to the beam parameters at its input. Also beam quality degradation is initiated mainly in the low energy sections of the linacs and later manifests itself in the form of beam halos at high energies. So careful studies in matching the beam from the ion source to the RFQ is required for minimizing emittance growth and avoiding beam halo formation, which is the major cause of beam loss. The LEBT also includes useful diagnostics for the beam from the ion source.

2.2 Design Issues

The main design criterion in the Low Energy Beam Transport (LEBT) system is to transport and match the beam from the ion source into the RFQ with minimum emittance growth and loss of beam current. The LEHIPA LEBT has been designed to match the 30 mA, 50 keV, CW proton beam from the ion source to the RFQ. The beam in the LEBT is a low energy, high current beam. At these energies, for such high currents, the space charge forces, which are the forces due to the coulomb repulsion between the particles, are very strong. These forces are highly non-linear and can lead to rapid increase in emittance and beam size. For this reason, a short length of the beam transport line is desirable. However, a short line does not leave much space for accommodating diagnostics for online monitoring of the beam which is desirable for high space charge beams. Thus, a proper choice has to be made between these conflicting requirements.

Two types of LEBTs are generally used to match the beams from the ion source into the RFQs – electrostatic [27] and magnetic [28,29]. Einzel lenses are used for focusing the beam in an electrostatic LEBT. Electrostatic focusing is more efficient than magnetic focusing at low energies and it allows for a more compact LEBT. However, the use of high voltages in electrostatic LEBT can cause voltage breakdown. Magnetic focusing, on the other hand, requires much larger space but it allows space charge compensation which facilitates the transport of space charge dominated beams in the LEBT. For space charge compensation, a gas is introduced in the LEBT line. The beam ionizes this gas producing electrons and ions. The electrons generated by the background gas ionization have very low velocity and get trapped in the beam thereby reducing the effect of the space charge forces. The ions are repelled by the positive potential of the proton beam towards the beam pipe. The magnetic forces in a magnetic LEBT have little effect on the low velocity electrons allowing high space charge compensation. A magnetic LEBT thus allows space charge compensation for dc and long pulse beams. The same is not possible using electric forces in an electrostatic LEBT which are velocity independent. Besides, the Einzel lenses that are used in electrostatic LEBTs induce strong aberrations that lead to emittance growth. Finally, as the beam in the electrostatic LEBT is not space charge compensated, the beam size and divergence increases with beam current. Hence operation of electrostatic LEBTs with high beam currents (for currents of tens of mA) is difficult as it will lead to increase in beam emittance and beam loss. Magnetic LEBT is then the best choice for high current beams for long pulse and CW operations. For short pulse operations, an electrostatic LEBT is generally preferred. For LEHIPA, due to CW operation and beam current of 30 mA, it is not possible to use a compact electrostatic LEBT. The LEHIPA LEBT has been designed using two solenoids for focusing and matching the beam from the ion source to the RFQ.

2.3 LEBT Design

2.3.1 Computer codes

Many computer codes are available to study the beam dynamics of space charge dominated beams. Generally two types of codes are used for beam dynamics simulations in accelerators and transport lines: envelope tracking codes and PIC (Particle-in-cell) codes.

2.3.1.1 Envelope codes

These codes follow the evolution of the beam through a series of beam transport elements represented by their matrices. The space charge forces are incorporated as externally applied defocusing forces. Only linear space charge forces are considered. For this, the beam is assumed to have a uniform charge distribution. Although in real life, the beams are not uniform, it has been shown that, for beams with ellipsoidal symmetry, the evolution of the rms beam envelope is nearly independent of the density profile and depends only on the linearized part of the self forces. Consequently, for calculation purposes, the real beam may be replaced by an equivalent uniform beam having identical rms properties [30,31]. Codes like TRANSPORT [32], TRACE2D and TRACE3D [33] are based on this method.

2.3.1.2 PIC codes

These codes are based on the Particle-in-cell method. They can compute space charge induced emittance growth effects by tracking the beam particles. The beam distribution evolves with time and non linear space charge forces are taken into account for calculation of emittance growth. The simulation is done with macroparticles, each of which represents 10^4 to 10^5 real beam particles. In this method, at each step a mesh is superimposed on the bunch. The number of particles in each cell is counted, and the smoothed space-charge force acting on each particle is obtained by summing the fields from the charges in each cell. These forces are applied to deliver a momentum impulse to each particle. These calculations can be time consuming and the time required for the calculation depends both on the number of macroparticles and the mesh. PARMTEQM [34], TRACK [35], TRACEWIN [36] and GPT [37] are some of the codes that use this method for beam dynamics calculations.

All these codes can simulate the effects of space charge compensation by reducing the effective current in the LEBT depending on the degree of space charge compensation. For more realistic beam transport simulations of space charge compensation, it is necessary to use a self-consistent code that can simulate the beam interactions with the gas (ionization, neutralization, scattering) and the beam line elements along with the dynamics of main beam and the secondary particles. Examples of such codes are WARP [38] or SOLMAXP [39].

TRANSPORT, TRACE 2D, TRACE 3D and TraceWin have been used for the design of LEHIPA LEBT.

2.3.2 Solenoid focusing

Solenoids are often used for focusing the low energy beams in magnetic LEBT systems [40]. Solenoids are preferred over quadrupoles because they are more efficient at lower energies and they focus in both the transverse directions with lesser aberrations. Solenoid focusing results from the interaction between the azimuthal velocity component induced in the entrance fringe-field region and the longitudinal magnetic-field component in the central region. In a solenoid, the longitudinal magnetic field on the axis is maximum at the centre and decreases toward the ends approaching zero far away from the solenoid. At the ends of the solenoids, there is a radial component of the magnetic field. Here, there is an interaction between the radial field component of the magnetic field and the axial velocity component of the beam, producing an azimuthal acceleration. In this way the particle acquires the azimuthal velocity component in the entrance fringe-field region. In the central region, particles traveling parallel to the field are unaffected, but those with an azimuthal velocity component will experience a force causing them to describe an orbit that is helical in space, and circular when viewed from the end of the solenoid. The net effect is a deflection toward the axis, independent of charge state or transit direction [41].

When a charged particle enters from the field-free region to the region of uniform magnetic field in a solenoid, it starts rotating with the Larmour frequency, which equals half the cyclotron frequency in the uniform magnetic field [42]. The particle's trajectory as it comes out of the solenoid is rotated by an angle about the axis of the solenoid given by

$$\phi_{rot} = \frac{qB_s L_{sol}}{2p}$$

Where q is the charge of the particle, B_sL_{sol} is the longitudinal field integral along the axis of the solenoid and p = $\gamma\beta$mc is the mechanical momentum of the particle.

2.3.3 Beam Dynamics

The computer codes TRACE2D and TRANSPORT were used for an initial design of the LEBT for a 50 keV, 30 mA DC H^+ beam. The LEBT was used to transport the phase space ellipse at the exit of the ion source and match it to the acceptance of the RFQ. The beam from the ion source was matched to the RFQ match point using TRACE2D to get a mismatch factor of zero in x and y. This matching was done using 2 solenoids and 3 drift spaces.

The RFQ match point [43] was calculated using TRACE2D. The matched ellipse parameters at the shaper were calculated by considering the first two cells of the shaper section. This ellipse was then back traced through the 8 cell long radial matching section to obtain the matched ellipse at the beginning of the radial matching section. This is shown in Fig. 2.1. The Twiss parameters at the RFQ match point are

$\alpha_x = \alpha_y = 1.8$,

$\beta_x = \beta_y = 6.43$ cm/rad.

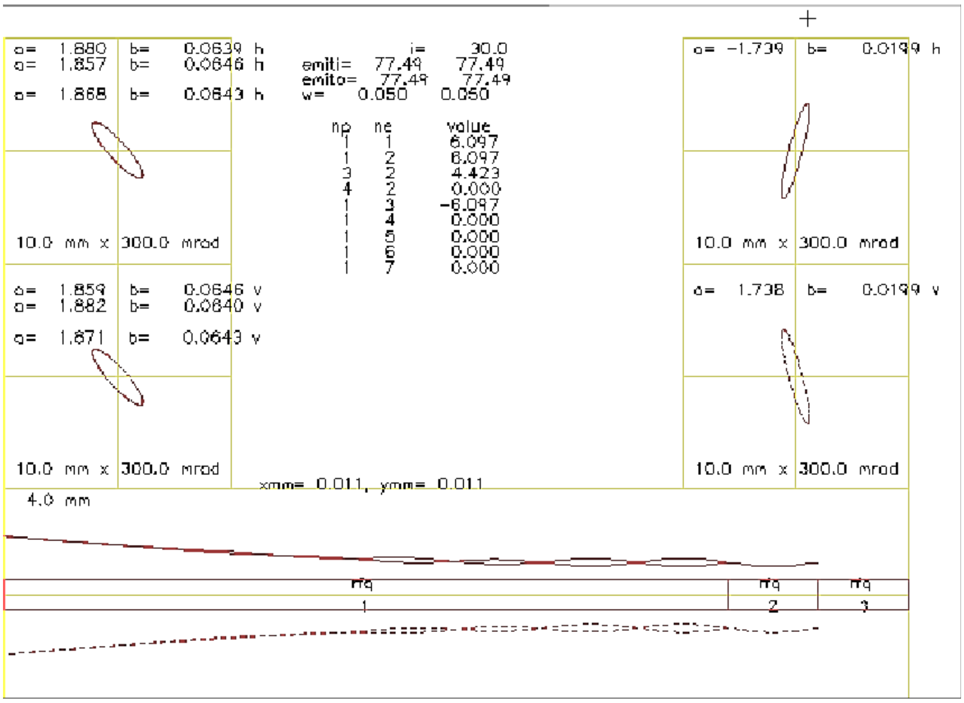

Fig.2.1: Beam trajectory through the radial matching section of the RFQ.

The ion source used in LEHIPA is an ECR based source with a five electrode system for beam extraction [26]. The Twiss parameters at the entrance of the last electrode of the ion source, obtained from the ion source design, are as follows:

$\alpha_x = \alpha_y = -1.8$

$\beta_x = \beta_y = 24.77$ cm/rad

for an emittance of 0.02π cm mrad.

TraceWin code was used for designing the LEHIPA LEBT. TraceWin includes both the envelope matching as well as the PIC subroutine PARTRAN for beam matching. Initially the beam was matched using the envelope matching method using two solenoids. The schematic of the LEBT is shown in Fig 2.2. The total length of the LEBT is 3.28 m which includes the length of the 5th electrode of the ion source which is grounded. The drift lengths have been chosen to be able to accommodate beam diagnostics, steerers, gate valves, bellows and vacuum pump in the LEBT.

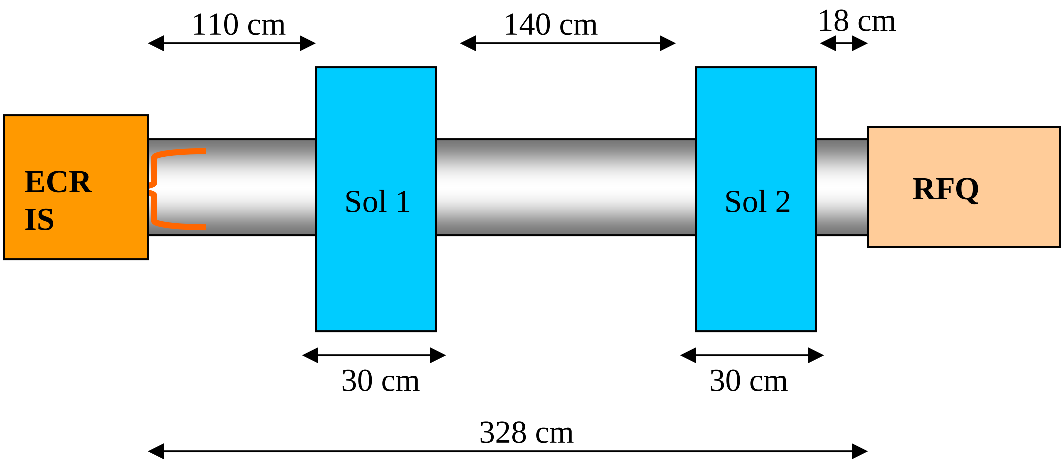

Fig. 2.2: Schematic of the LEHIPA LEBT.

The beam trajectory with envelope matching is shown in Fig. 2.3. and the LEBT parameters obtained from this matching are shown in Table 2.1.

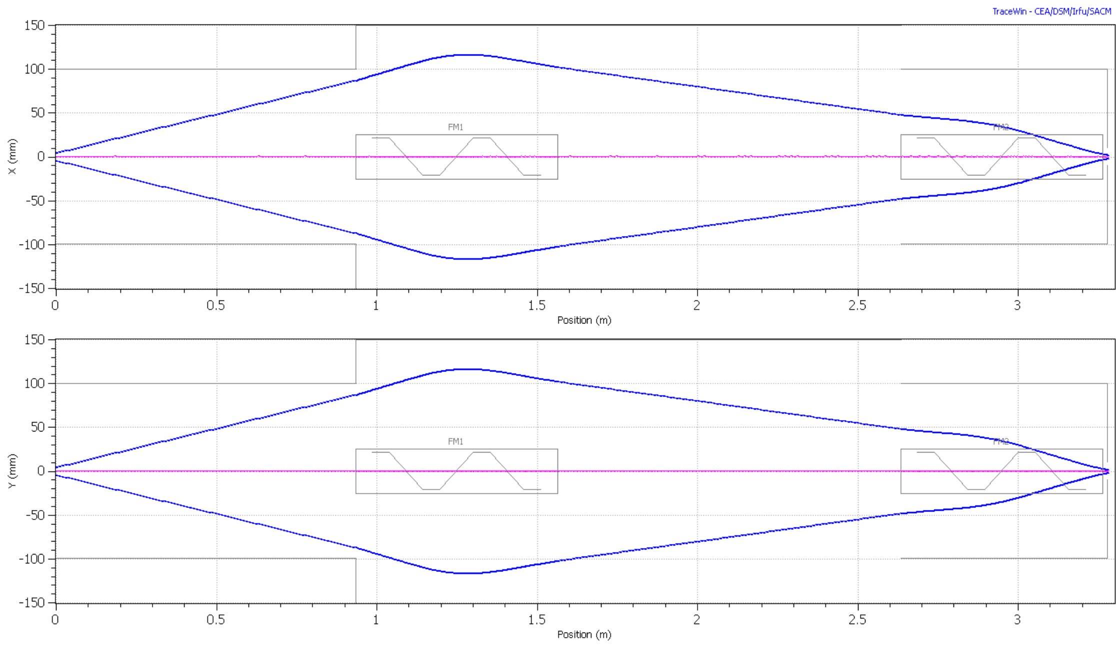

Fig. 2.3: Beam trajectory in LEBT as calculated from envelope calculation in TRACEWIN with no space charge compensation.

Table 2.1. LEBT Parameters from envelope matching.

Element	**Length(cm)**	**Strength(kG)**
Drift	110	
Solenoid	30	1.628
Drift	140	
Solenoid	30	2.229
Drift	18	
Total length	328	

The final matching was then done using PIC calculations using PARTRAN in TraceWin. The matching was studied with different input beam distributions at the LEBT input: the KV distribution, the 4D Waterbag distribution [44] and the Gaussian distribution. For all simulations, a mismatch factor ~ 10^{-6} was considered as acceptable for the design of the LEBT system. The matching was done with 10,000 particles while the beam dynamics through the LEBT after the matching was studied with 100,000 particles. For all matching calculations in TraceWin, the actual 1 D profile of the magnetic field in the designed solenoid was considered. The results of the matching with different input beam distributions are summarized in Table 2.2. The beam profile in transverse phase space and coordinate space at the end of the LEBT as obtained with different input beam distributions are shown in Fig. 2.4., Fig. 2.5 and Fig. 2.6. It can be seen that for KV distribution, for which the space charge forces in the beam are linear, the increase in emittance is less as compared to the 4 D Waterbag and Gaussian distribution which have highly non linear space charge forces. The increase in emittance at the end of the LEBT for the full beam without space charge compensation is very high and not acceptable for injection into the RFQ.

Table 2.2. Matching Parameters for different beam distribution at the input of LEBT.

Input beam Distribution	**Solenoid 1 (kG)**	**Solenoid 2 (kG)**	**Emit. At the end of LEBT ε_x (mm mrad)**	**Emit. At the end of LEBT ε_y (mm mrad)**
Envelope	1.628	2.229	0.2000	0.2000
KV	1.608	2.212	0.225	0.225
4 D waterbag	1.583	2.201	0.4352	0.4352
Gaussian 3 σ	1.545	2.219	0.7858	0.7859

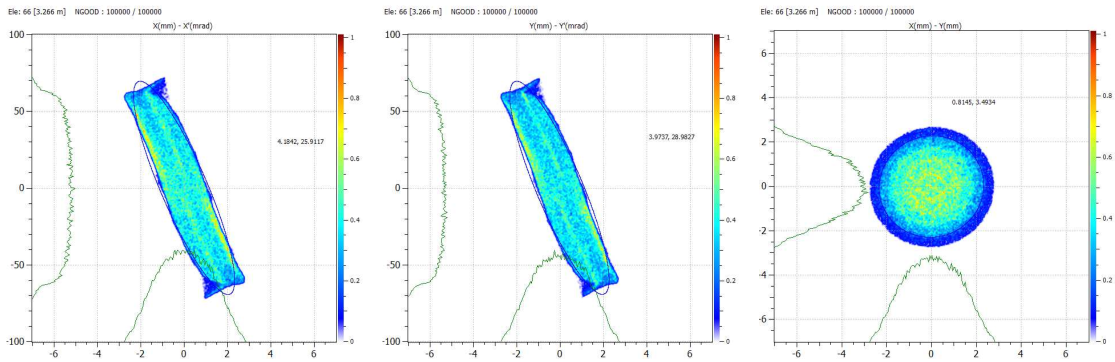

Fig. 2.4: Beam profile in transverse phase space and coordinate space at the end of the LEBT with KV distribution.

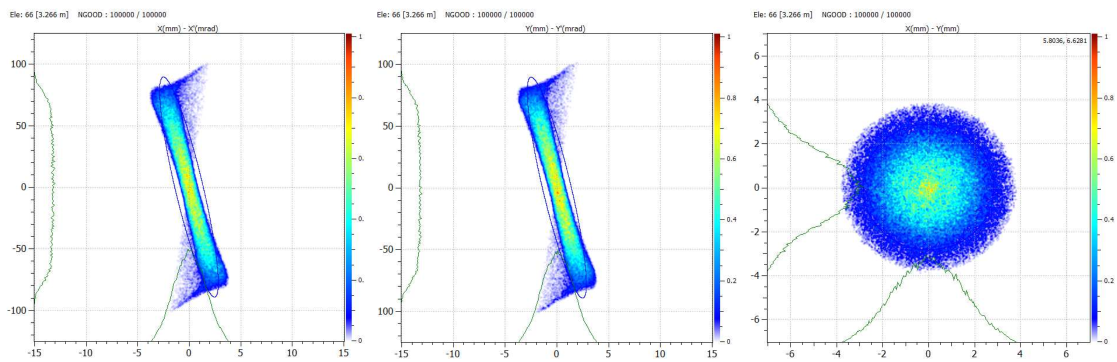

Fig. 2.5: Beam profile in transverse phase space and coordinate space at the end of the LEBT with 4D Waterbag distribution.

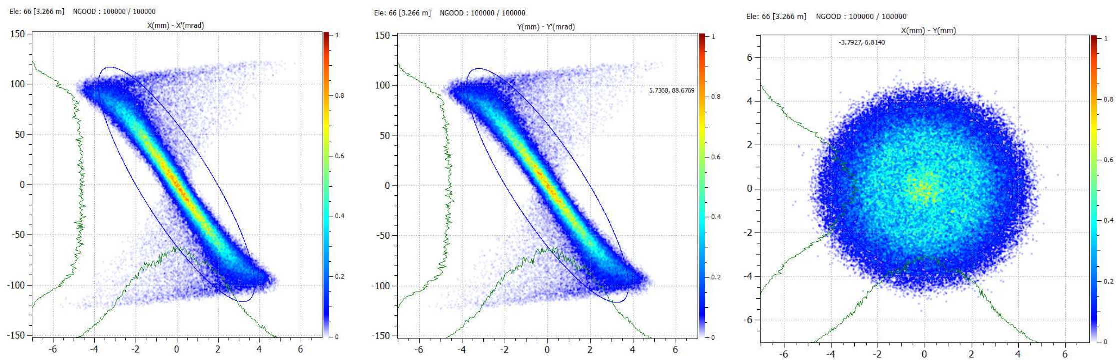

Fig. 2.6: Beam profile in transverse phase space and coordinate space at the end of the LEBT with 3 σ Gaussian distribution.

There are two solutions to matching the beam from the ion source to the RFQ in the LEBT: with or without a beam waist between the two solenoids. The former requires higher values of the solenoid field and is called strong focusing while the latter is called weak focusing solution. It has been found that strong focusing in the LEBT leads to higher increase in beam emittance at the end of the LEBT [45]. Hence the weak focusing has been adopted for the LEHIPA LEBT.

Effects of changing the lengths of the drifts in the LEBT on beam size and emittance were studied. The results of these simulations are shown in Table 2.3., Table 2.4. and Table 2.5. All these simulations were done for the uncompensated beam current of 30 mA. The matching was done with 10,000 particles while the beam dynamics was done with 100,000 particles using a 4 D Waterbag beam distribution at the input of the LEBT. It is seen that reducing the length of the first drift has significant effect on the maximum beam size and beam emittance at the end of the LEBT. Reducing the length of the second drift does not have any effect on the maximum beam size in the LEBT but increases the emittance at the end of the LEBT. Increasing the length of the third drift space increases the emittance at the end of the LEBT. From here it can be inferred that, for minimum beam size in the LEBT, it is desirable that the length of the first drift be kept as small as possible. For minimum emittance growth in the LEBT, it is desirable to have a small length of the first and third drift spaces while the second drift space should be long.

Table 2.3. Effect of changing the first drift length on the LEBT design.

Length of Drift 1 (cm)	Length of Drift 2 (cm)	Length of Drift 3 (cm)	Strength of Sol 1 (kG)	Strength of Sol 2 (kG)	Maxm beam size (cm)	Emit. at LEBT end ε_x (mm mrad)	Emitt. at LEBT end ε_y (mm mrad)
110	140	18	1.583	2.201	12.3	0.4352	0.4352
90	140	18	1.712	2.377	11.17	0.3386	0.3431
70	140	18	1.889	2.573	9.11	0.2851	0.2883
50	140	18	2.202	2.822	5.39	0.2593	0.2612

Table 2.4. Effect of changing the second drift length on the LEBT design.

Length of Drift 1 (cm)	Length of Drift 2 (cm)	Length of Drift 3 (cm)	Strength of Sol 1 (kG)	Strength of Sol 2 (kG)	Emit. at LEBT end ε_x (mm mrad)	Emitt. at LEBT end ε_y (mm mrad)
110	180	18	1.568	2.362	0.3944	0.4012
110	160	18	1.575	2.285	0.4124	0.4189
110	140	18	1.583	2.201	0.4352	0.4352
110	120	18	1.593	2.117	0.4670	0.4729
110	100	18	1.615	2.012	0.5366	0.5422
110	80	18	1.642	1.911	0.5813	0.5864
110	60	18	1.692	1.760	0.6662	0.6714

Table 2.5. Effect of changing the third drift length on the LEBT design

Length of Drift 1 (cm)	**Length of Drift 2 (cm)**	**Length of Drift 3 (cm)**	**Strength of Sol 1 (kG)**	**Strength of Sol 2 (kG)**	**Emit. at LEBT end ε_x (mm mrad)**	**Emitt. at LEBT end ε_y (mm mrad)**
110	140	18	1.583	2.201	0.4352	0.4352
110	140	30	1.528	1.931	0.4320	0.4362
110	140	40	1.471	1.787	0.4821	0.4850
110	140	50	1.405	1.684	0.5805	0.5836

2.3.4 Solving KV equation in the LEBT

Simulations were also done using the analytical KV beam envelope equations to compare the results from the code.

The general KV equation [46] describes a charged-particle beam propagating in the z direction through a channel with linear external and space-charge forces, where the transverse external focusing functions, $k_x(z)$ and $k_y(z)$, or the transverse emittances, ε_x and ε_y may be different. The equations for the beam envelopes, $X(z)$ and $Y(z)$, are coupled and may be written in the form

$$X'' + k_x X - \frac{2K}{X+Y} - \frac{\varepsilon_n^{\;2}}{\beta^2\gamma^2 X^3} = 0$$

$$Y'' + k_y Y - \frac{2K}{X+Y} - \frac{\varepsilon_n^{\;2}}{\beta^2\gamma^2 Y^3} = 0$$

Where, K represents the force due to space charge.

In our case, where solenoids are used for focusing the beam in the LEBT,

$|k_x| = |k_y| = \left(\dfrac{qB}{2mc\beta\gamma}\right)^2$ is the hard edge focusing functions and B is the magnetic field for the solenoid.

$K = \dfrac{2I}{I_0\beta^3\gamma^3}$ is the generalized perveance with I_0 = 31 MA for protons.

X and Y are the beam envelope radius in x and y respectively. The rms unnormalised emittance of the 50 keV, 30 mA proton beam from the ion source is taken as 0.02 cm mrad. The beam is circular and hence identical in x and y. Hence we can write the above set of equation with X = Y = R as

$$R'' + kR - \frac{K}{R} - \frac{\varepsilon_n^{\ 2}}{\beta^2\gamma^2 R^3} = 0$$

The initial conditions are R(0) = 4.38 mm and R′(0) = 36.4402 mrad.

The maximum beam size in the LEHIPA LEBT obtained with the numerical solution of KV equation is 12.2 cm and is 12.3 cm with TRACE2D which are comparable. The beam trajectory in the LEBT with the numerical solution of KV equation is shown in Fig. 2.7. It can be seen that the beam profiles in both the cases are similar and focusing is achieved.

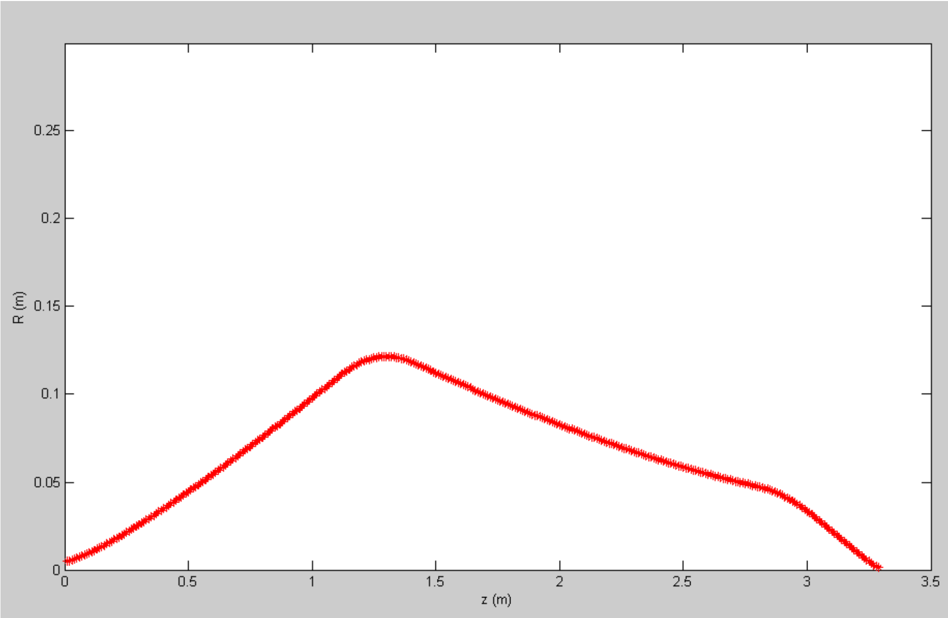

Fig.2.7: Beam trajectory in the LEBT with the numerical solution of KV equation.

2.4 Space charge compensation

2.4.1 Theory of space charge compensation

The transport of high current beams at low energies is critical, because at kinetic energies of a few MeV, the beams are space charge dominated. These space charge forces, due to coulombic repulsion between the beam particles, are highly non linear and cause increase in beam size and emittance. These effects of high space charge can be reduced by using space charge compensation, where the space charge of the beam is neutralized by trapped electrons. This occurs when a residual gas is introduced and the gas pressure in the LEBT is relatively high (10^{-5} mbar). The proton beam ionizes the molecules of the residual gas and produces electrons which are trapped in the positive potential of the beam and reduces the beam space charge as shown in Fig. 2.8.

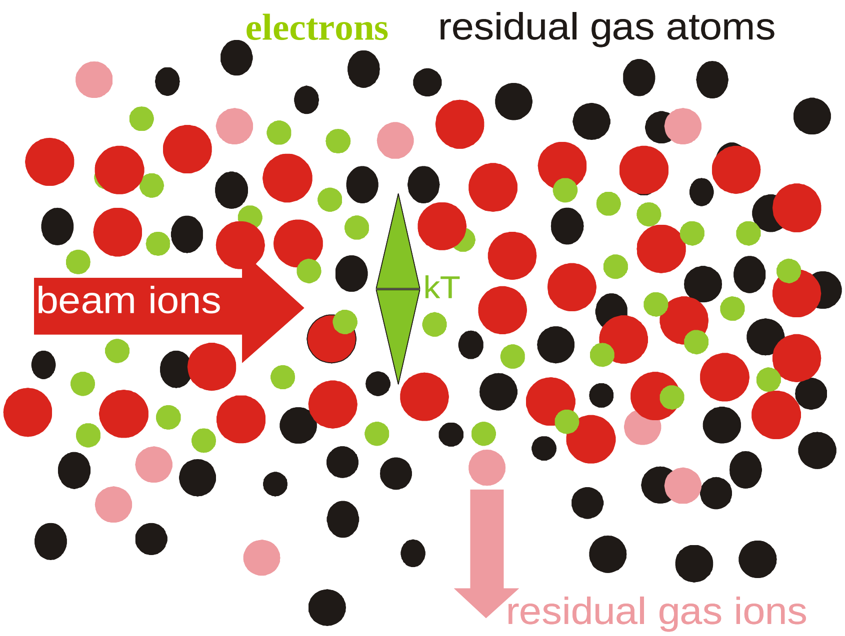

Fig. 2.8: Space Charge compensation.

Consider a proton beam propagating through a H_2 residual gas. It produces e^-/H_2^+ by ionization.

$$p + H_2 \rightarrow p + e^- + H_2^+$$

The secondary particles created in the collisions that have the same charge polarity as the beam particles i.e. the H_2^+ ions, are expelled to the walls by the beam's space charge. Electrons, produced by ionization, are trapped within the beam by its own space charge, resulting in a decrease of the effective beam potential and hence the space-charge expansion of the beam, to a value that is considerably less than that of the unneutralized beam. The space charge compensation degree for the 75 keV, 130 mA proton beam of the LEDA has been measured and found to be 95% - 99% [47]. Experimentally, a decrease in beam emittance has been observed with the increase in background pressure [48].

The degree of neutralization depends on the gas density n_g, the chemical composition of the gas, the ionization cross section σ_i for the production of electron-ion pairs, the velocity v of the beam particles and the pulse length of the beam.

The gas density for a background pressure of 10^{-5} torr is of the order of 3.2116×10^{17} m^{-3} and the beam density for proton beam current of 30 mA is 6.068×10^{14} m^{-3}.The density increase with time of the electrons or ions created in the collisions between the beam particles and the number of gas molecules or atoms is given by

$$\frac{dn}{dt} = n_b n_g \sigma_i v$$

Where, n_b is the beam density, which for a proton beam current of 30 mA at 50 keV is 6.068×10^{14} m^{-3}. Then, the rate of production of electrons with time is

$$\frac{dn}{dt} = n_b n_g \sigma_i v$$

$$= 1.2043 \times 10^{19}\, m^{-3} sec^{-1}$$

An important parameter is the charge-neutralization time, defined as the time it takes to obtain full charge neutralization of the beam (τ_n). It is given by:

$$\tau_n = \frac{1}{\sigma n_g v_p}$$

which is of the order of 50 μsec in the case of LEHIPA LEBT.

2.4.2 Beam dynamics with space charge compensation

Simulations were carried out to study the effects of space charge compensation in the LEBT. The effects were studied using both the KV distribution and the 4 D Waterbag distribution in TraceWin. The results of these simulations are shown in Table 2.6 and Table 2.7 and plotted in Figs. 2.9 & 2.10. It can be seen that as the degree of space charge compensation increases, both the maximum beam size in the LEBT as well as the transverse emittances at the end of the LEBT come down. Smaller beam size in the LEBT allows us to use a solenoid with smaller aperture, thus reducing spherical aberrations and the power requirement from the solenoid. Thus space charge compensation facilitates beam transport in the LEBT. The beam phase spaces at the end of the LEBT with different degrees of space charge compensation using 4D Waterbag distribution at the input is shown in Fig. 2.11.

Table 2.6. Effect of space charge compensation on beam dynamics with KV distribution.

Degree of SCC	**Maxm. Beam size (cm)**	**Solenoid 1 (kG)**	**Solenoid 2 (kG)**	**Emit. at LEBT end ε_x (mm mrad)**	**Emit. at LEBT end ε_y (mm mrad)**
0 %	12.3	1.608	2.212	0.2250	0.2248
70 %	7.52	1.529	2.135	0.2033	0.2033
90 %	5.68	1.43	2.088	0.2015	0.2016
95 %	5.31	1.386	2.069	0.2010	0.2012
99 %	1.33	1.337	2.060	0.2008	0.2009

Table 2.7. Effect of space charge compensation on beam dynamics with 4 D Waterbag distribution.

Degree of SCC	Maxm. Beam size (cm)	Solenoid 1 (kG)	Solenoid 2 (kG)	Emit. at LEBT end ε_x (mm mrad)	Emit. at LEBT end ε_y (mm mrad)
0 %	12.3	1.583	2.201	0.4352	0.4352
70 %	7.52	1.498	2.175	0.3190	0.3207
90 %	5.68	1.419	2.108	0.2505	0.2510
95 %	5.31	1.377	2.090	0.2241	0.2243
99 %	1.33	1.337	2.057	0.2040	0.2040

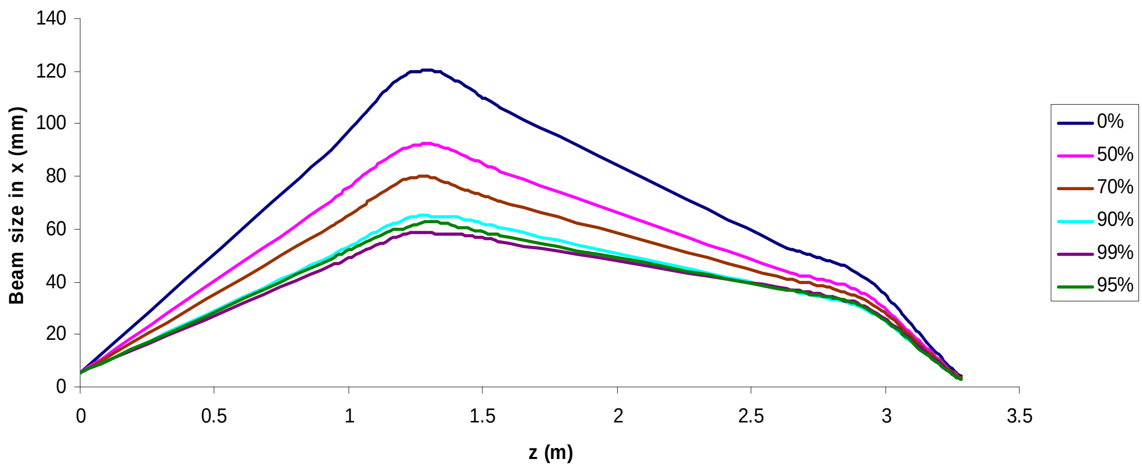

Fig. 2.9: Beam trajectories in the LEBT with different degrees of Space charge compensation.

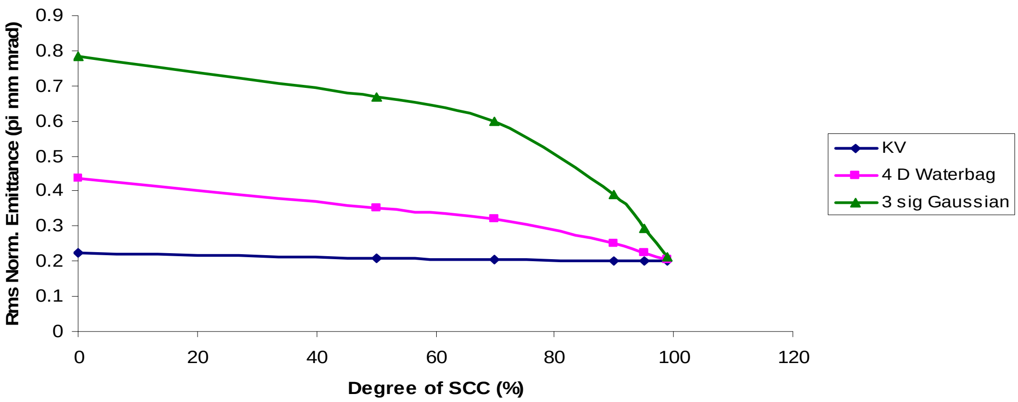

Fig.2.10: Variation of emittance at the end of the LEBT with degree of space charge compensation for KV, 4D Waterbag and Gaussian distribution at the input.

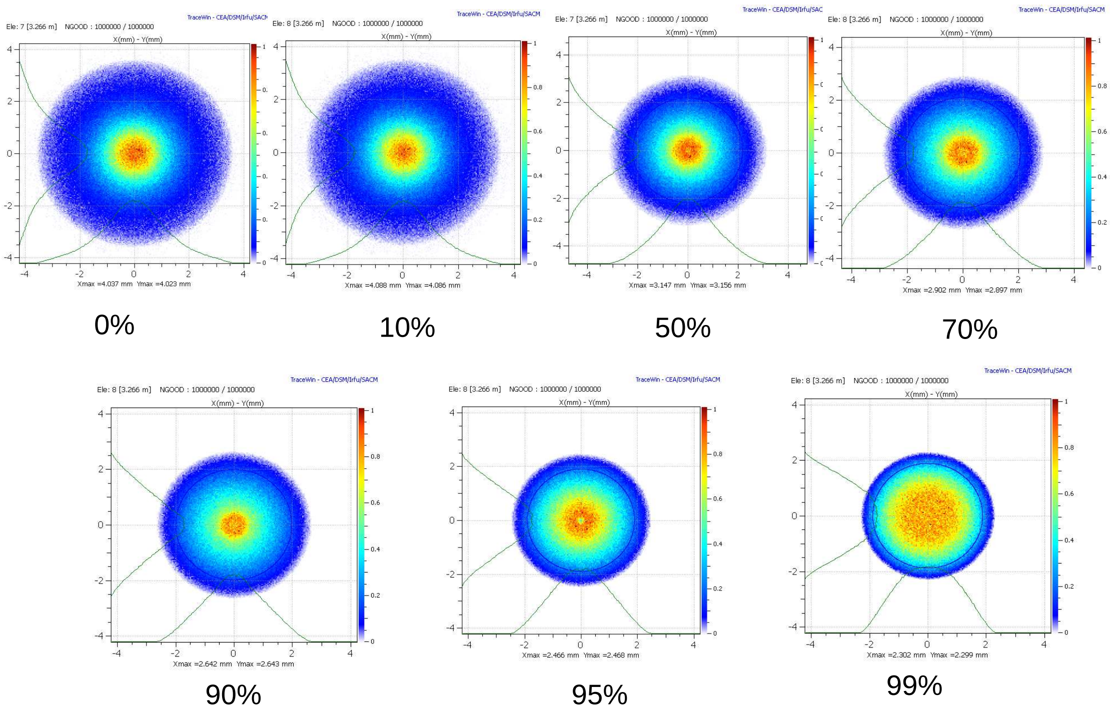

Fig.2.11: Transverse beam profile at the end of the LEBT with different degrees of space charge compensation with 4D Waterbag distribution at the input.

2.5 Aperture studies

The beam from the ion source does not consist of only H^+ ions. It contains some fraction of H_2^+ and H_3^+ ions also. In addition to transporting and matching the proton beam from the ion source to the RFQ, an important function of the LEBT is to prevent these unwanted species from entering into the RFQ. The H_2^+ and H_3^+ ions, due to their higher momentum as compared to the protons are relatively less focused by the solenoids in the LEBT and can be removed by putting an aperture at a suitable location that will allow the proton beam to pass through but will cut out a significant amount of H_2^+ and H_3^+ beams. Studies were done to locate the position and size of the aperture. Both the strong and weak focusing options were studied using KV, 4D Waterbag and 3 σ Gaussian distribution of the input beam with 95 % space charge compensation. Typical values of normalized emittances for H^+, H_2^+ and H_3^+ ions used in the simulations are $\varepsilon_{n,rms}$ (H^+) =0.2 π mm mrad, $\varepsilon_{n,rms}$ (H_2^+) =0.1 π mm mrad and $\varepsilon_{n,rms}$ (H_3^+) =0.0675 π mm mrad. From preliminary measurements of the ECR ion source to be used in LEHIPA, it has been found that the beam has a proton fraction of 74% and H^{2+} and H^{3+} comprise 19% and 7% respectively of the total beam. This corresponds to an input beam consisting of 30 mA H^+, 7.7 mA H_2^+ and 2.84 mA H_3^+. The results of the simulations are summarized in Table 2.8 and Fig. 2.12. (a) & (b) show the beam trajectories of H^+, H_2^+ and H_3^+ ions in the transport line for the weak and strong focusing cases respectively.

It can be seen from the Figures that an aperture of radius 10 mm at the LEBT exit is sufficient for full transmission of the H^+ beam. For the case of weak focussing, the H^{2+} and H^{3+} ion beams have a large beam size at the LEBT exit and can be eliminated largely by using the 5 mm aperture at the exit of the LEBT. In the case of strong focussing, however, the H^{2+} ion beam also has a size comparable to that of the H^+ beam at the LEBT exit and hence is also fully transmitted by the 10 mm aperture. Also, the increase in emittance at the end of the LEBT is much more in the case of strong focussing. Hence, it has been decided to go for the weak focussing option for the LEHIPA LEBT with a 10 mm water cooled aperture at the end of the LEBT.

These calculations were also done with varying degrees of space charge compensation in the LEBT for the weak focussing case with uniform distribution. It was found that, for all cases, the transmission of H_2^+ and H_3^+ ion beams remains less than 3.3% of the total beam current.

Table.2.8. Beam parameters at the end of the LEBT with a 10 mm radius aperture for different input beam distributions for strong and weak focussing cases.

Distribution	**Transmission (%)**			**Emittance in x (π mm mrad)**			**Emittance in y (π mm mrad)**		
	H^+	**H^{2+}**	**H^{3+}**	**H^+**	**H^{2+}**	**H^{3+}**	**H^+**	**H^{2+}**	**H^{3+}**
KV									
Strong Focusing	100	100	17.23	0.2019	0.1005	0.0374	0.2022	0.1007	0.0381
Weak Focusing	100	7.27	4.07	0.2007	0.0374	0.0198	0.2011	0.0368	0.0180
4D Waterbag									
Strong Focusing	100	100	20.54	0.2420	0.1050	0.0320	0.2421	0.1053	0.0326
Weak Focusing	100	9.09	5.06	0.2196	0.0306	0.0154	0.2203	0.0319	0.0161
3 σ Gaussian									
Strong Focusing	100	100	25.87	0.4284	0.1142	0.0276	0.4248	0.1154	0.0271
Weak Focusing	100	10.94	6.04	0.2772	0.0261	0.013	0.2813	0.0262	0.0132

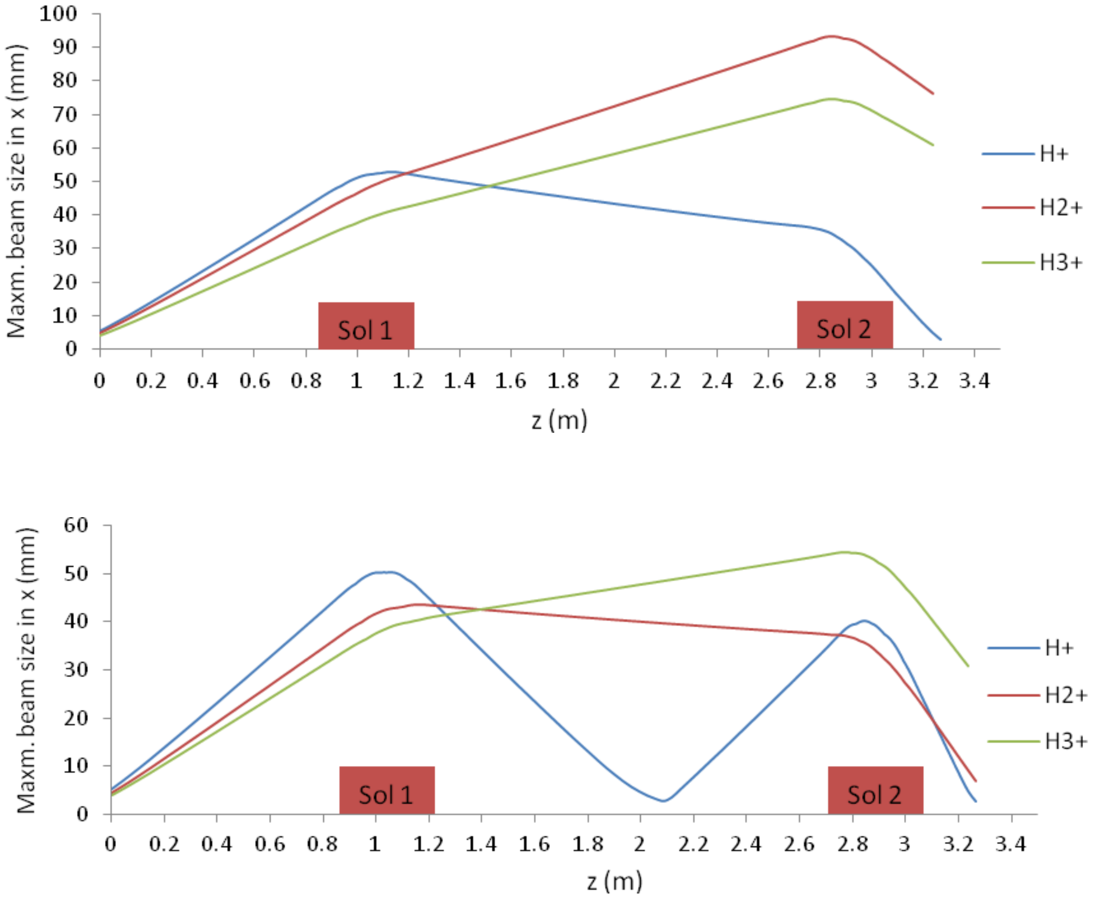

Fig.2.12: Comparison of evolution of the beam profile along the LEBT (with 95% SCC) of H^+, H_2^+ and H_3^+ beams with (a) weak focusing (b) strong focusing.

2.6 Solenoid Design

Beam dynamics simulations showed that the peak magnetic field required in the two solenoids for focusing the beam in the LEBT is less than 3.5 kG and the effective length of the solenoids is 30 cm. The envelope codes like TRANSPORT and TRACE 2D assume a hard-edged model for the solenoid. This means that the magnetic field is assumed to be uniform in the region $0 < z < L$ and zero outside this region, where L is the effective length of the solenoid. For the solenoid lens, using the linear approximation i.e., suppose that the uniform magnetic field with effective length L which has a sudden change from 0 to B_0 at entrance port while from B_0 to 0 at exit port replaces the actual magnetic field, then as shown in Fig.2.13., the effective length *L* of solenoid lens is defined by

$$\int_{-\infty}^{\infty} B(z)dz = B_0 L$$

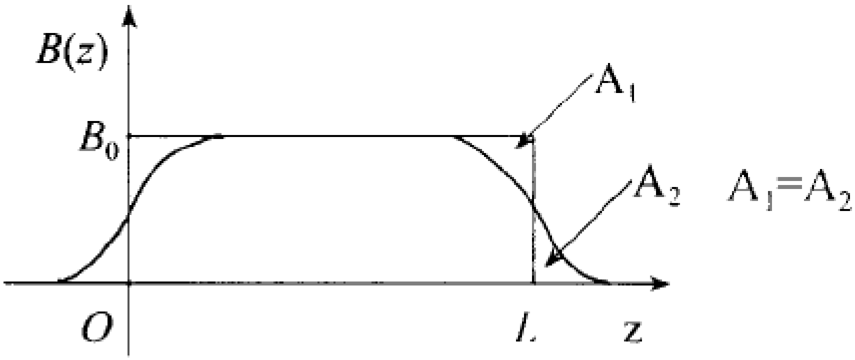

Fig.2.13: Definition of Effective length L of solenoid.

The geometric length of the solenoid is then chosen as the length for which the area under the actual magnetic field curve of the solenoid becomes equal to B_0L. The solenoid design was done in POISSON [49]. The solenoid simulated in POISSON is shown in Fig.2.14. A 3 cm thick core made of magnetic material is used to increase the magnetic field of the solenoid by providing a low resistance path to the magnetic flux lines, with a lower value of current in the solenoid coils. The longitudinal magnetic field profile in the designed solenoid is shown in Fig. 2.15. The parameters of the designed solenoid magnet are shown in Table.2.9. A 3D design of the solenoid was also done using CST Microwave Studio [50]. The 3D model is shown in Fig. 2.16. and the magnetic field on the axis calculated by CST Microwave Studio is shown in Fig. 2.17.

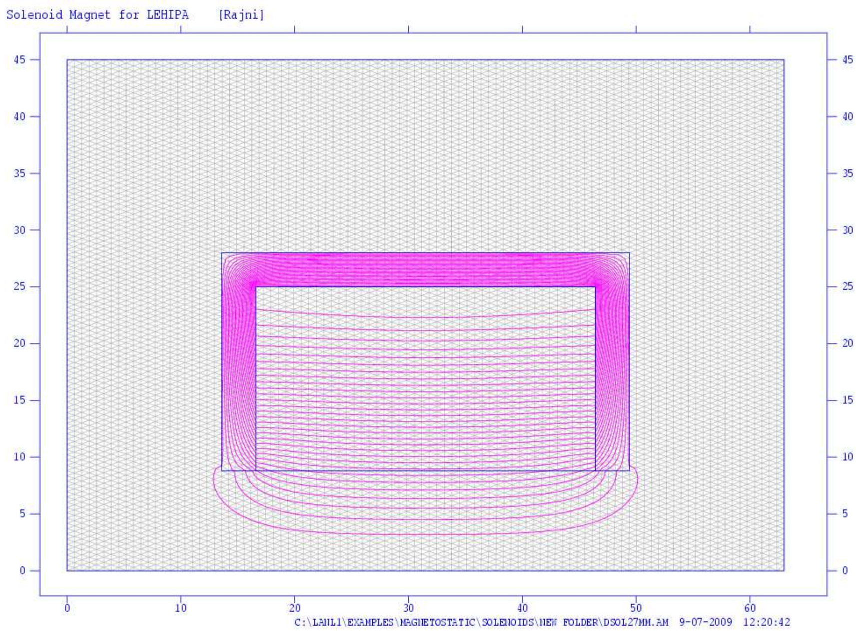

Fig.2.14: Solenoid simulated in POISSON.

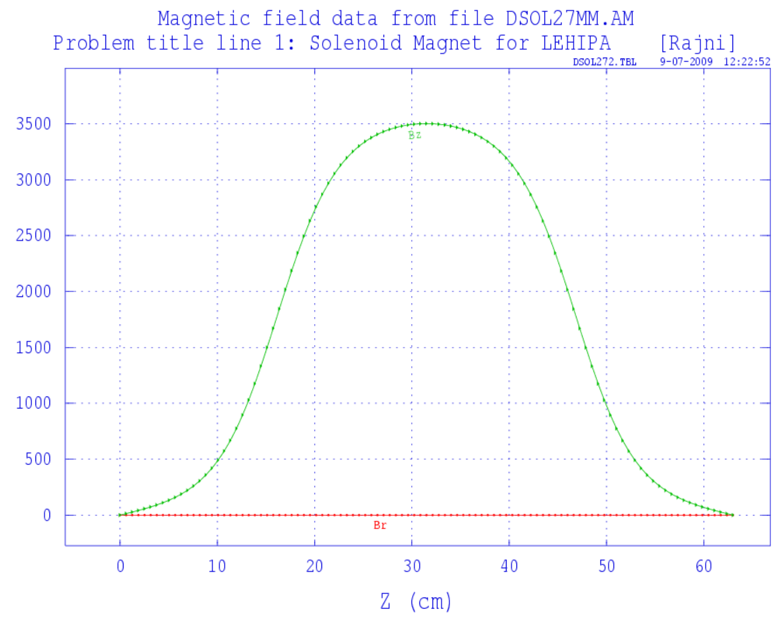

Fig.2.15: Longitudinal magnetic field profile in the simulated solenoid.

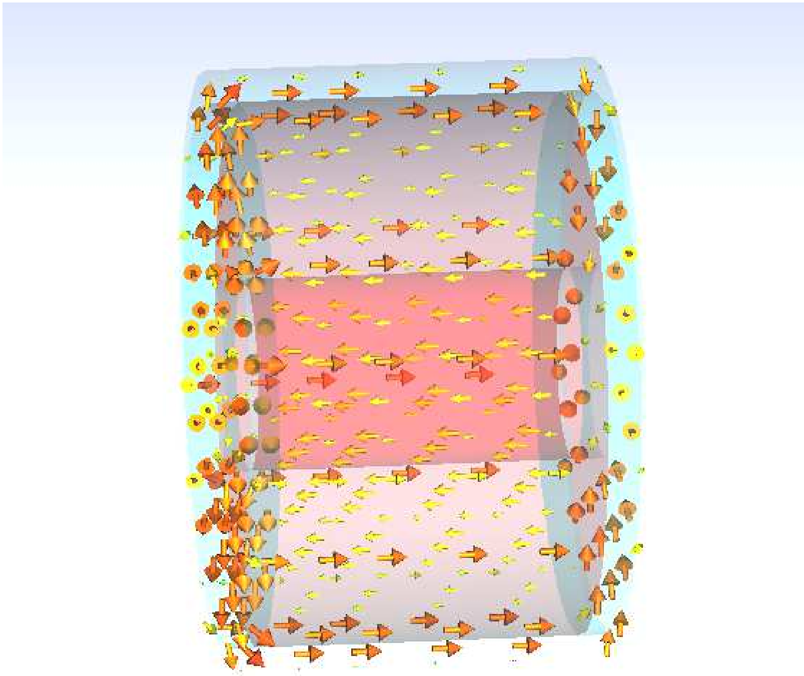

Fig. 2.16: Solenoid design in CST MWS

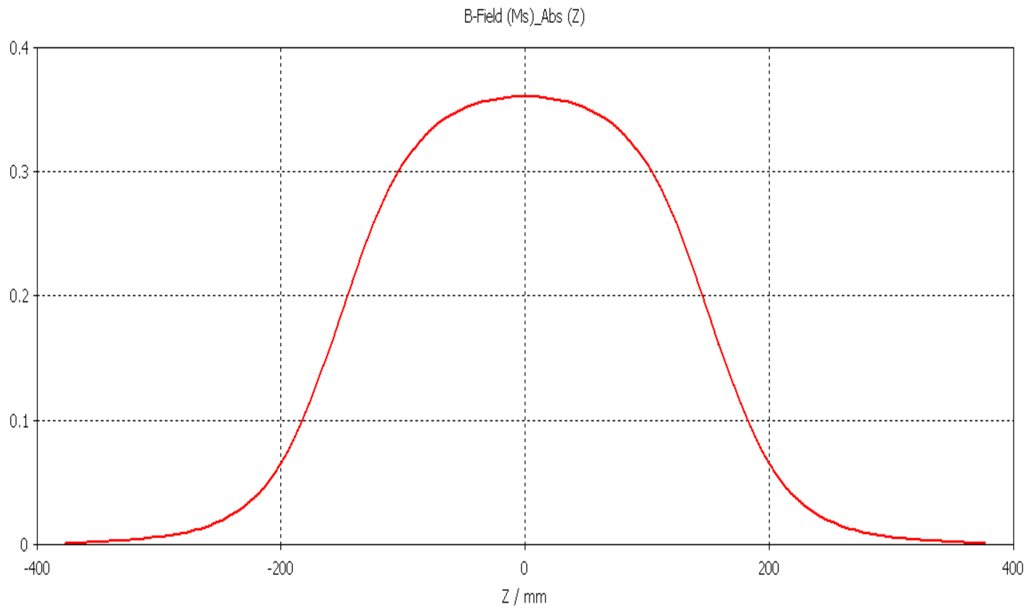

Fig. 2.17: Magnetic field profile along z axis calculated from CST MWS

The solenoid comprises of 8 identical pancake coils. Each pancake consists of 4 x 18 turns. A hollow copper conductor of 7 x 7 mm with 5 mm diameter hole in the centre for cooling water flow is used for the coils. The conductor coil is wrapped in an insulator tape. The conductor in each pancake spirals from the inside out. One fourth of the coil starts at the ID and spirals outward one over the other covering 18 turns. The remaining three fourths of the coil at the ID is wound 3 turns along the length of the solenoid and then crosses over to the next layer and is again wound 3 turns along the length in the opposite direction and so on till it reaches the top. The 2 ends of the coil in the pancake exit at 180^o from each other. This means that if one end comes out from the top, the other end comes out from the bottom of the pancake. The 8 pancakes are connected electrically in series and in parallel for cooling water flow. The coils in adjacent pancakes are wound in opposite directions and are then connected electrically in series. All the 8 coil ends coming out from the top are connected to the water inlet and the 8 coil ends coming out from the bottom are connected to the water outlet. Thus there are 8 cooling circuits. The 8 pancakes are assembled together and enclosed in an octagonal cylindrical core made of Tata A Grade Steel (high permeability material). Openings are provided in the core at the top and bottom for the coil ends to come out for electrical and water connections.

These solenoids have been fabricated and tested and the results are found to be in good agreement with the design values. Fig.2.18. shows the 8 pancakes in the solenoid. Fig. 2.19. shows the cooling circuits in the solenoid. The solenoid complete and assembled is shown in Fig. 2.20.

Table.2.9. Parameters of the Solenoid magnet.

Parameter	**Value**
ID of the solenoid	176 mm
OD of the solenoid (with coil)	500 mm
OD of the solenoid (with core)	560 mm
Effective length	300 mm
Physical length	358 mm
Peak field	3.5 kG (on the axis)
Ampere turns	89500
No. of turns	(18 x 4) x 8 = 576
Maxm. Current in coil	155 A
Voltage drop	61 V
Total power dissipation	9.5 kW
No. of Pancakes	8
Total length of coils required	80 x 8 =512 m
Total resistance of the coils	0.3922 ohms (at room temperature)
Dimensions of copper conductor	7 X 7 mm with circular hole of dia. 5mm
No. of cooling circuits	8
Thickness of iron core (MS 1010)	30 mm

Fig. 2.18: Pancakes in the solenoid.

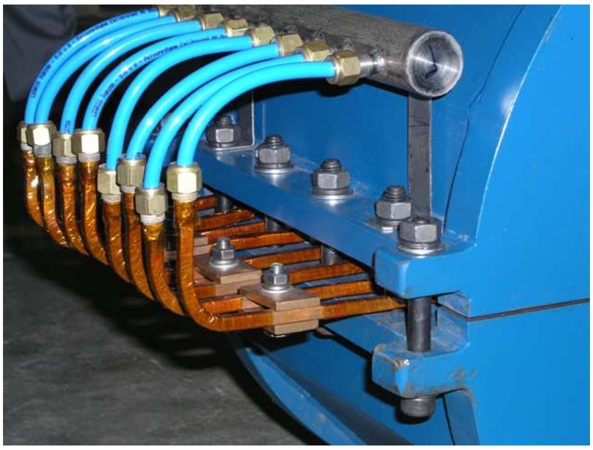

Fig.2.19: Cooling circuits in the solenoid.

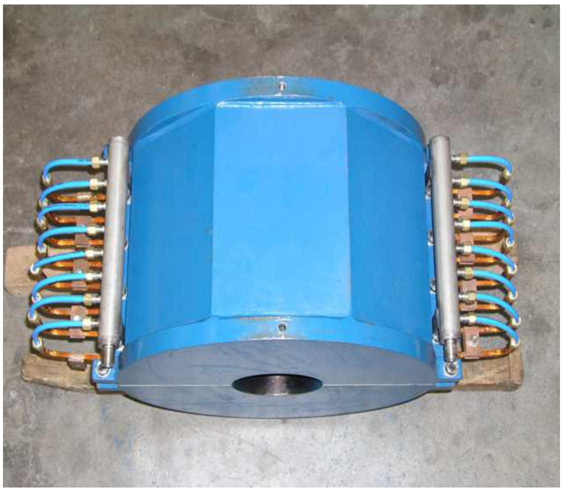

Fig.2.20: The solenoid completely assembled.

2.7 Steerer Design

A magnetic steerer has been designed for steering a 50 keV proton beam into the RFQ. The requirement is beam steering of ±3 cm in horizontal and vertical directions from the axis of the beamline at a distance of 75 cm from the entrance of the steering magnet. This implies a steering angle of 0.04 radian.

The approximate value of the magnetic field on the axis inside the steering magnet can be calculated from the analytical relation:

$$B = \frac{mvSin\theta}{qL}$$

$$\Rightarrow \qquad BL = 0.00129 \text{ T m}$$

The design has been done for B = 95 Gauss for a steerer length of 15 cm.

The magnetic field inside the steering magnet is not exactly uniform and changes when one moves away on either side of the centre. This field deviation should be minimum and magnetic field should be as uniform as possible in the good field region.

A simple steerer configuration is shown below in Fig.2.21. Two sets of coils A1, A2 and B1, B2 steer the beam in y and x respectively. The magnetic field due to coils A1 and A2 is in the x direction. This field acts on the beam (whose direction is perpendicular to the plane of the paper) and the beam experiences a force in the y direction. Hence if the beam is displaced vertically, then these set of coils A1 and A2 are used to steer it back. Similarly the set of coils B1 and B2 steer the beam if it is displaced in the x direction. Thus the two sets of coils independently steer the beam in x and y.

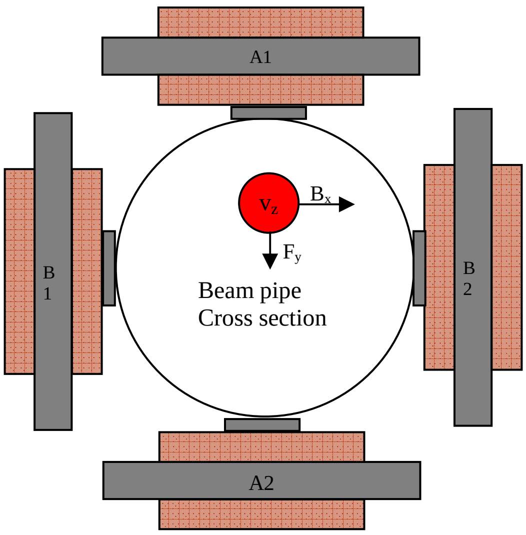

Fig.2.21: Cross-section of the steerer.

A steerer in this configuration was designed using the code POISSON. The coil and core geometry is optimized to get a magnetic field of 95 Gauss at the centre. A conventional design with a plate inside the coil generates the required steering field, however, the field produced by it is not uniform in the good field region which will result in distorting the beam quality. In order to reduce this field deviation suitable shim plates are used. The parameters of the steering magnet are given in Table 2.10 and the magnetic field profile in the steerer is shown in Fig. 2.22.

Table. 2.10. Parameters of the steering magnet.

Parameter	**Value**
Ampere-turn	2500
Width of the coil	17 mm
Height of the coil	100 mm
Width of the iron block	20 mm
Height of the iron block	140 mm
Coil cross section (half)	17 cm^2
Field at origin	95 Gauss
Shim width	2 mm
Shim height	60 mm
Length of the steerer	150 mm
Diameter of the wire	1.45 mm (AWG 15)
Turns per layer	65
Total no. of layers	11
Current	3.5 A
Total resistance of 2 coils	5.329 Ohms
Voltage drop	19 V
Total power dissipation	65.28 W

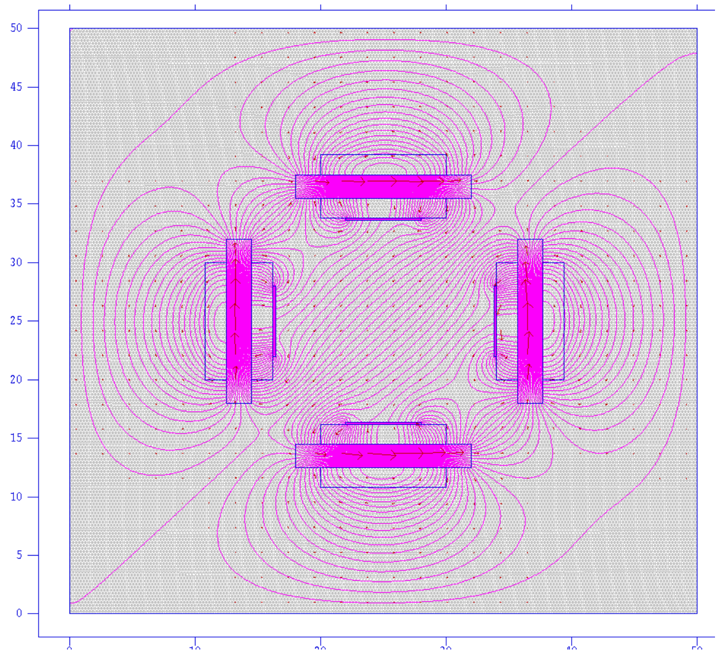

Fig. 2.22: Magnetic field profile in the steerer.

2.8 Electron Trap design

The H^+ beam from the ion source contains a smaller fraction of H_2^+ and H_3^+ ions also. There are also electrons trapped in the beam due to space charge compensation in the LEBT. All these have to be removed before entering the RFQ. The H_2^+ and H_3^+ ions, having a greater momentum than proton are less focused by the solenoids and hence can be cut off by putting a collimator just before RFQ entrance. To maximize the lost fraction, a collimator is needed just before RFQ entrance. In addition an electron trap [51,52] is also needed to prevent the electron from the neutralized beam to enter the RFQ. The electron trap is a ring with a negative 1-2 kV potential placed at the entrance of the RFQ through which the beam passes. The potential from this ring prevents low-energy plasma electrons from going through it, but not 50 keV protons.

The electrons generated by residual gas ionization have very little energy. Maximum energy transferred by an ion beam to an electron is [28]:

$$T_{\max} = \frac{2m_e c^2 \beta^2 \gamma^2}{1 + \frac{2\gamma m_e}{M} + \left(\frac{m_e}{M}\right)^2}$$

Where m_e is electron mass, M is proton mass and β is proton velocity. This comes out to be about 110 eV for a 50 keV proton beam.

Voltage used for trap is much higher than maximum electrons energy for two reasons:

1. The electrode is at some distance from beam axis and we need more potential to have an effective field on axis;
2. When the electrons are stopped, the beam is completely unneutralized and the space-charge effect is very high and it tends to attract electrons on the other side of the trap.

The electron trap has been designed in POISSON. The electric field lines in the electron trap simulated in POISSON is shown in Fig. 2.23.

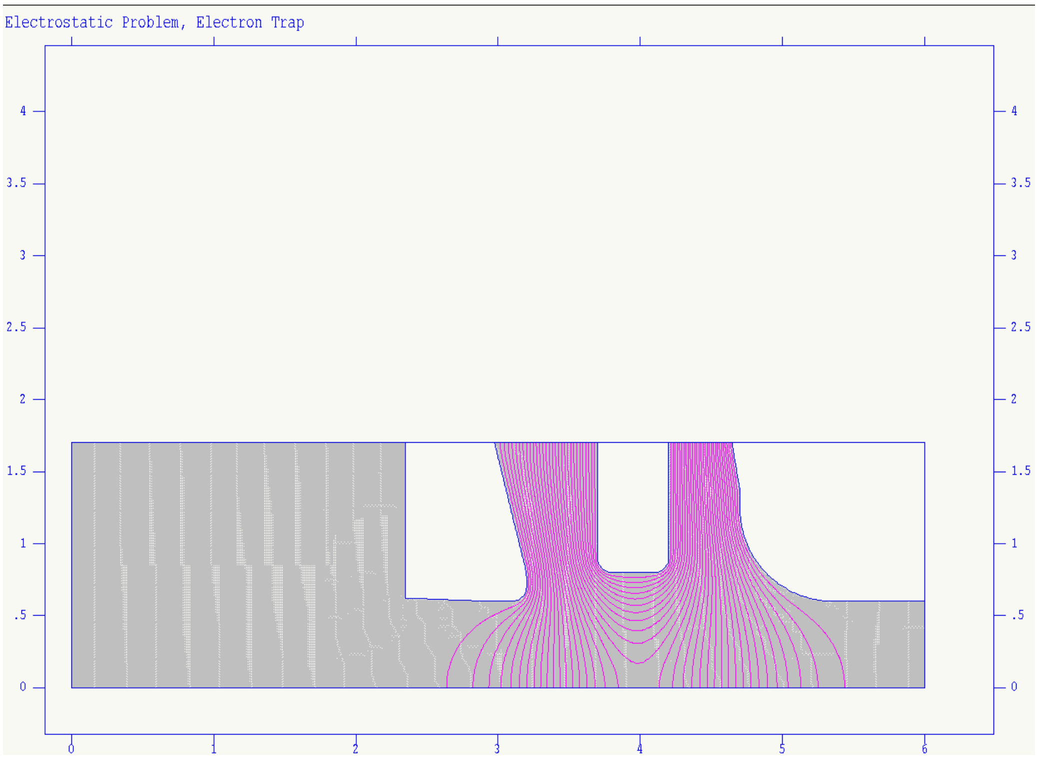

Fig. 2.23: Electron trap simulated in POISSON.

2.9 Beam Diagnostics

Beam properties like beam size, beam position and beam current need to be measured in the LEBT. The beam in the LEBT being high intensity beam, interceptive diagnostics cannot be used. Non interceptive diagnostics like DCCT and residual gas beam profile monitors will be used for online monitoring and measurement of the beam properties. The drift spaces in the beam line will be used to accommodate these diagnostics.

2.10 Summary and conclusions

A two solenoid based magnetic LEBT has been designed for LEHIPA. The main design criterion was to match the beam from the ion source to the RFQ with minimum emittance growth and beam loss. For this detailed beam dynamics studies have been done to study the beam transport in the LEBT. It was found from simulations that space charge compensation decreases the beam size as well as emittance growth in the LEBT. Hence space charge compensation will be used in the LEBT. The LEBT is 3.28 long and its functions include beam focusing and steering at the RFQ match point, dc beam current diagnosis and beam profile measurement through CCD monitors. The LEBT will also have a water-cooled collimator and an electron trap at the RFQ entrance. Design of LEBT components like the solenoids, steerers and electron trap has also been done. A schematic of the designed LEBT is shown in Fig.2.24.

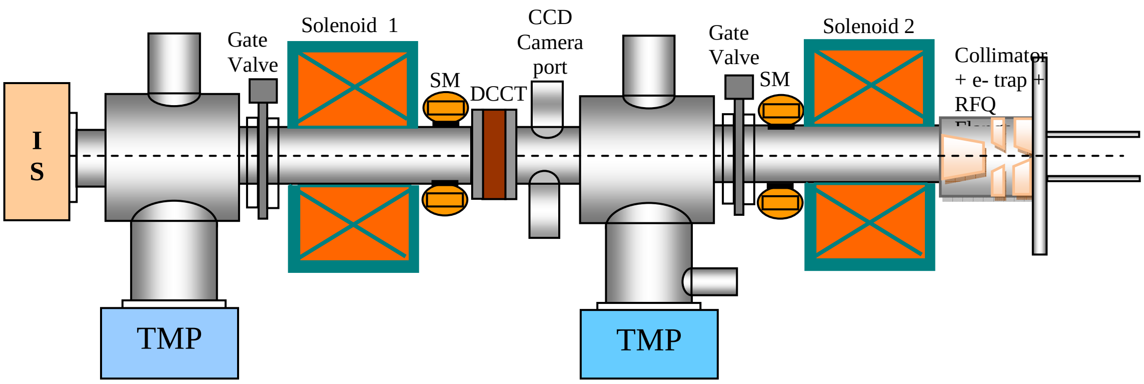

Fig.2.24: Schematic of the LEHIPA LEBT.

CHAPTER 3

Beam Characterization in the LEBT

3.1 Introduction

One of the components of the LEHIPA project [24] at BARC is the 3 MeV CW RFQ [53]. This RFQ is about 4 m long and involves handling of 500 kW RF power at 352.2 MHz. The RFQ is a complex structure which has very tight fabrication tolerances. In order to understand the accelerator technologies involved in fabricating and operating 4 vane type RFQs, it was planned to first build a smaller 400 keV D^+ RFQ to help gain experience in fabrication [54], handling of RF power and operation of high power RFQs. So, this system consisting of a 50 keV, 1 mA dc deuteron source, a LEBT line and a 400 keV CW RFQ was designed. The designed RFQ is 1 m long and the RF power required is about 70 kW. A two-solenoid based LEBT was setup to match the beam from the ion source to the 400 keV RFQ. The transverse emittance of helium, deuteron and proton beams in the LEBT was measured.

3.2 LEBT Design

A 2 solenoid based, magnetic LEBT similar to the LEHIPA LEBT was designed for the 400 keV RFQ based deuteron linac. The design was done for a 50 keV, 1 mA deuteron beam. The deuteron beam was extracted from the RF ion source and accelerated to 50 keV using an accelerating tube. The beam parameters, emittance and the Twiss parameters, were measured at a distance of 1.87 m from the accelerating tube. With these parameters as the input the beam was back traced from here using TRANSPORT code [32] to get the beam parameters at the exit of the accelerating tube. These were then used as input for LEBT design. These input parameters are

$\alpha = 1.679$

$\beta = 3.351$ mm/mrad

$\varepsilon_{n,rms} = 0.043\ \pi$ mm mrad

This corresponds to a converging beam of x = 8.853 mm and x′ = 5.163 mrad. The RFQ match point was obtained from TRACE 2D [55]. The Twiss parameters for the RFQ match point are

$\alpha = 1.35$

$\beta = 3.57$ cm/rad

The beam matching to RFQ was done using TRANSPORT, TRACE 2D [55] and TraceWin [36] codes. The schematic of the LEBT is shown in Fig.3.1. The parameters of the designed LEBT in TraceWin are listed in Table 3.1 and the beam trajectory through the LEBT is shown in Fig. 3.2. The beam phase space at the end of the LEBT is shown in Fig. 3.3. The rms normalized emittance at the end of LEBT increases to 0.054 π mm mrad with 4 D Waterbag distribution at the input.

Table 3.1. Parameters of the LEBT.

ELEMENT	**LENGTH (cm)**	**Magnetic Field (kG)**
Drift	33.05	
Solenoid	30	2.221
Drift	88.3	
Solenoid	30	2.152
Drift	18.35	
Total Length	**199.7**	

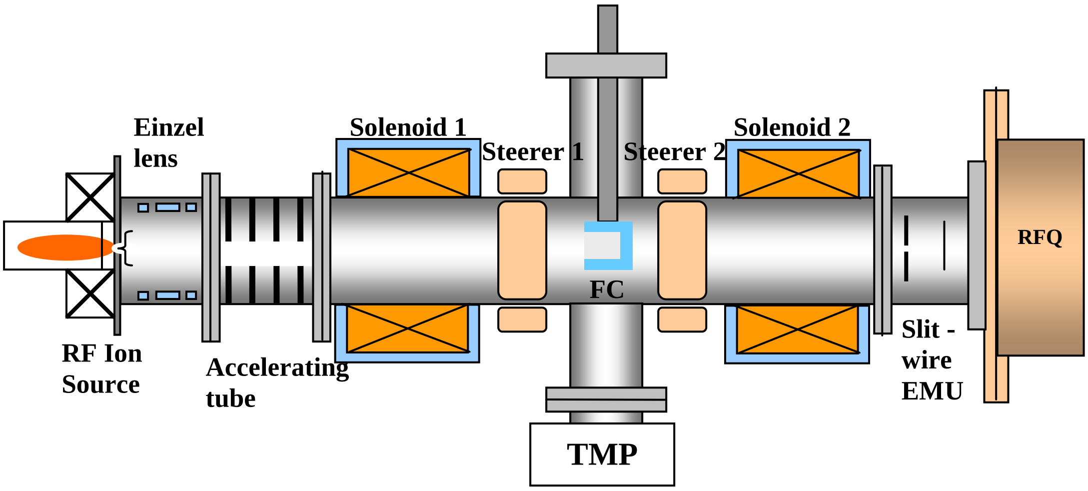

Fig. 3.1: Schematic of the LEBT for the 400 keV linac.

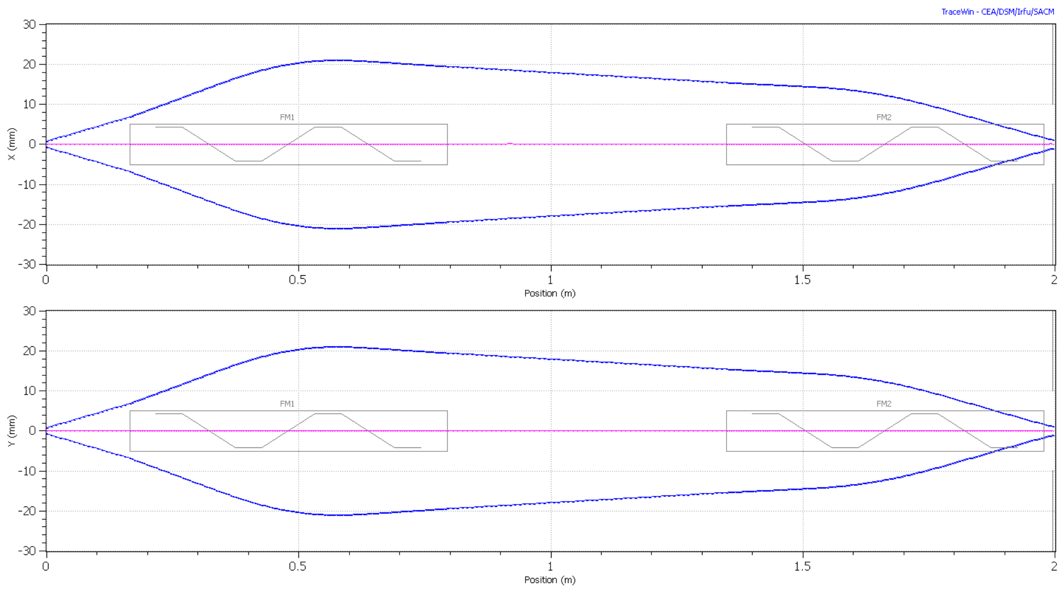

Fig. 3.2: Beam trajectory in LEBT as calculated from envelope calculation in TRACEWIN.

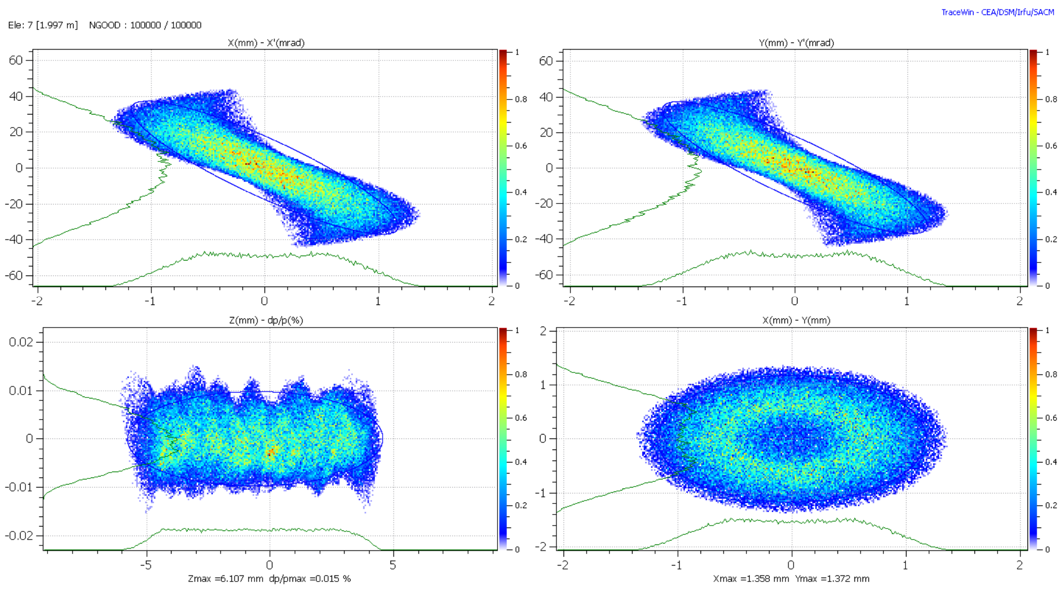

Fig.3.3: Beam profile at the end of the LEBT with 4 D Waterbag distribution.

The solenoid magnets for the LEBT were designed in POISSON [49]. The solenoids have been designed for a peak field of 4 kG and effective length of 30 cm. The solenoid simulated in POISSON is shown in Fig. 3.4 and the magnetic field profile in the designed solenoid is shown in Fig.3.5.

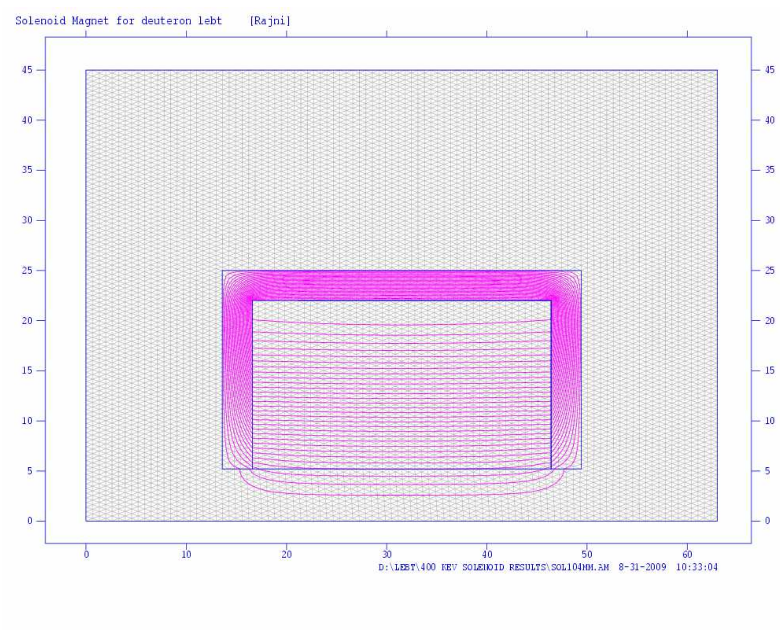

Fig. 3.4: Solenoid magnet designed in POISSON.

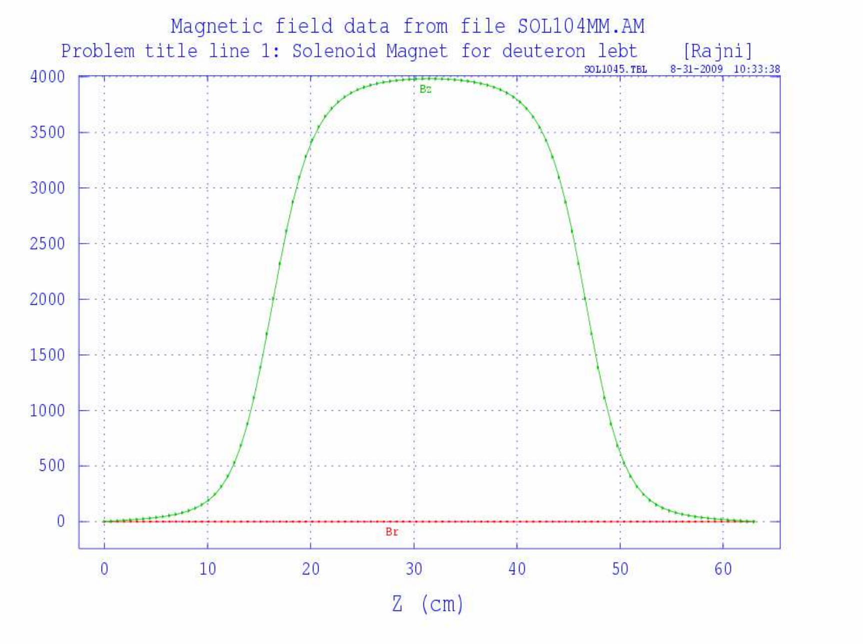

Fig.3.5: Longitudinal magnetic field profile in the simulated solenoid.

Based on the design, the solenoids were fabricated and tested. The results were found to be in good agreement with the designed values. The variation in longitudinal field 3 cm away from the axis is less than 0.3%. This has been verified from magnetic field profile measurements on the solenoid as shown in Fig.3.6.

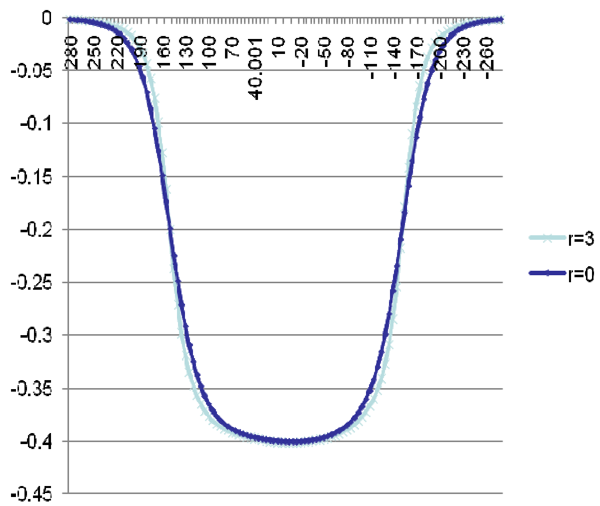

Fig.3.6: Magnetic field profile measurement of the LEBT solenoid.

3.3 LEBT Test Bench

Based on the design, a LEBT test bench [56] was setup at Van de Graaff Laboratory, BARC to characterize the beams in the LEBT. The LEBT test bench consists of an RF ion source, Einzel lens, accelerating tube and 2 solenoids. There were 2 Faraday cups and 2 BPM's in the line to measure the beam current and size. The ion source assembly is shown in Fig.3.7.and the LEBT line with the two solenoids is shown in Fig. 3.8. The beam from the ions source was extracted and then focussed by an Einzel lens. The beam was then accelerated to 50 keV using a dc accelerating tube. This 50 keV beam was then focused with the help of the two solenoids in the LEBT line. He^+, D^+ and H^+ beams have been extracted from the ion source and characterized. . Beam currents of 100 μA, 240 μA and 200 μA for He^+, D^+ and H^+ beams respectively have been extracted and transported through the LEBT line. The emittance of these beams was measured using solenoid scan method and slit scan method.

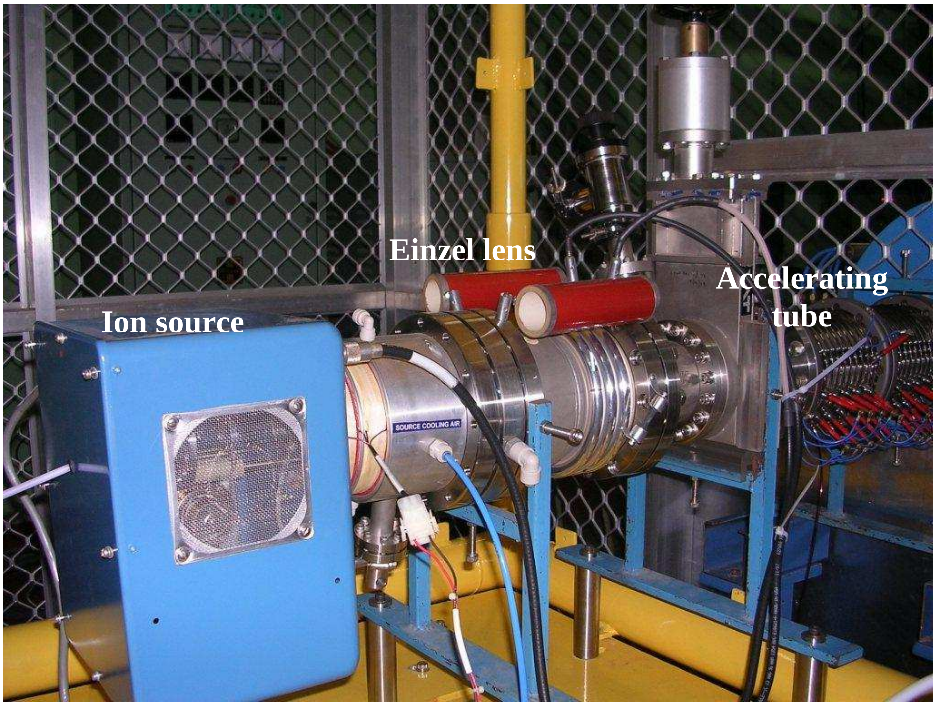

Fig. 3.7: Ion source assembly for the LEBT test bench.

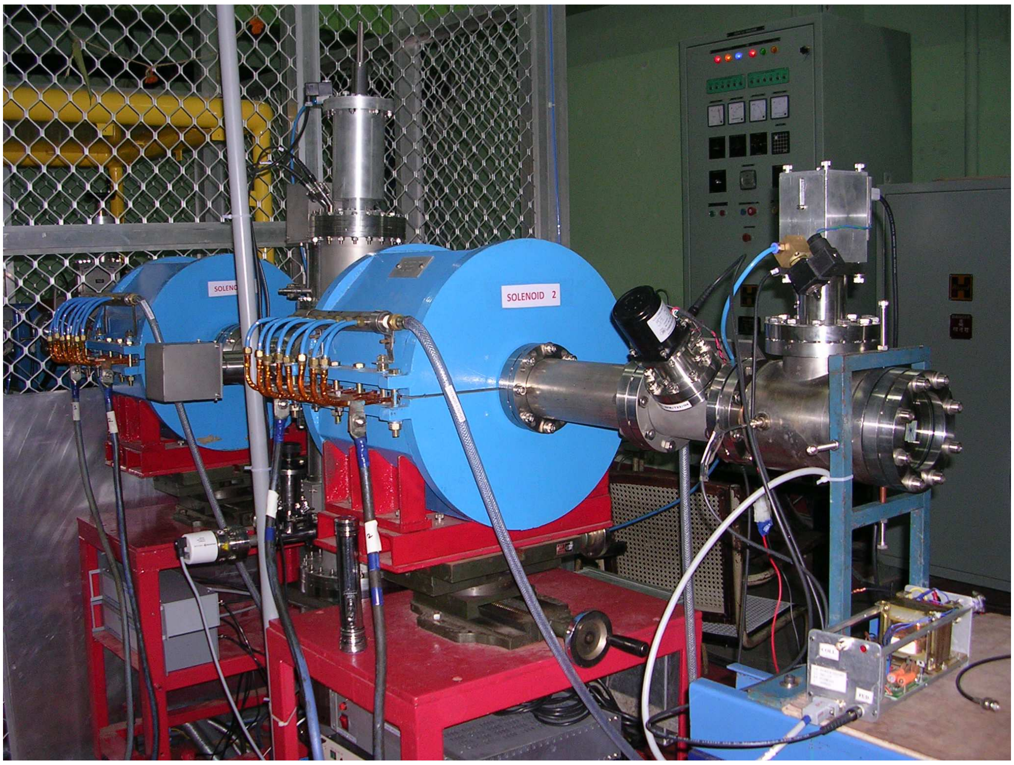

Fig.3.8: LEBT test bench at BARC.

3.4 Transverse beam emittance measurement

3.4.1 Emittance definitions

Beam is defined as a collection of particles that is moving in a certain direction with a very small spread in the energy of the particles. The beam particles move in one direction and have a very limited extent in the direction perpendicular to the direction of motion. Emittance is a property of the beam that quantifies the quality of the beam.

Each particle in the beam can be represented by six coordinates in the six-dimensional phase space x, p_x, y, p_y, z, p_z. The two dimensional projections of the beam in the transverse phase spaces x-p_x and y-p_y are approximately represented by ellipses in the absence of the non-linear forces. With linear focusing, the trajectory of each particle in phase space lies on an ellipse, which may be called the trajectory ellipse. Instead of the transverse momenta, it is convenient to measure the divergence angles, dx/ds and dy/ds. Plots of x − dx/ds and y − dy/ds are known as the trace-space or unnormalized phase-space projections. The general equation for a trajectory ellipse in trace space is written as

$$\gamma x^2 + 2\alpha x x' + \beta x'^2 = \varepsilon \tag{3.1}$$

where

$$1 + \alpha^2 = \beta\gamma \tag{3.2}$$

Here α, β and γ are the Twiss Parameters [57] and ε is called the emittance. The Twiss parameters describe the shape and orientation of the beam ellipse in phase space and are related to the beam size and divergence. The emittance is related to the area of the phase space ellipse. The trace space ellipse in the x transverse plane is shown in Fig.3.9.

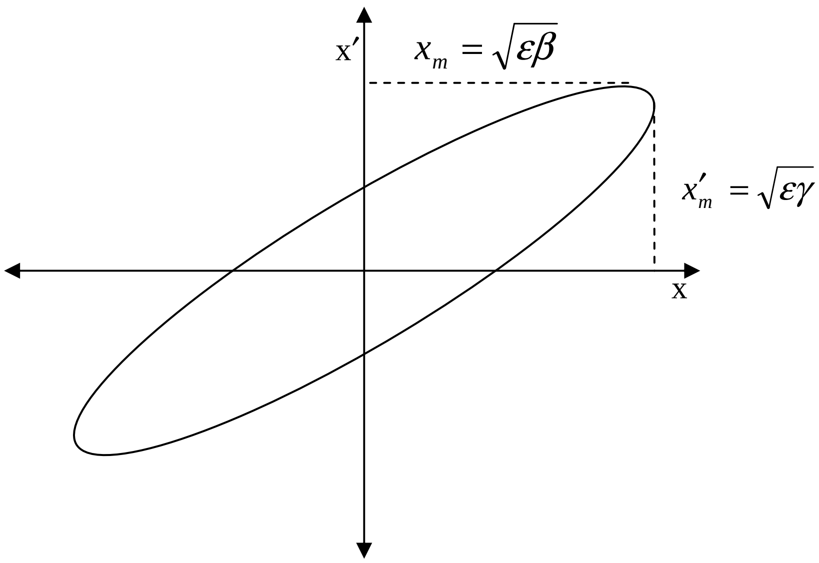

Fig. 3.9: The beam ellipse in transverse trace space x.

Here,

$$x_m = \sqrt{\varepsilon\beta} \tag{3.3}$$

is the beam half width,

$$x'_m = \sqrt{\varepsilon\gamma} \tag{3.4}$$

is the beam half divergence, and the phase space area is given by

$$Area = \varepsilon\pi$$

Hence, emittance is given by

$$\varepsilon = \frac{Area}{\pi} \tag{3.5}$$

This emittance is called the 'unnormalized emittance'. When a beam accelerates, the transverse beam size shrinks. It is convenient to define the 'normalized emittance' which is independent of the beam energy. The normalized emittance is given by

$$\varepsilon_n = \varepsilon\beta\gamma \tag{3.6}$$

Where β and γ are the relativistic factors. Whereas, the unnormalized emittance decreases with increase in beam energy, the normalized emittance is unaffected by the acceleration of the beam. The units of emittance are given in π mm mrad.

When non linear forces are present, the beam phase space deviates from being elliptical. The beam emittance is then defined in terms of the mean-square values, or second moments of the coordinates and momenta of the particles. This is known as the rms emittance and is given by

$$\varepsilon_{rms} = \sqrt{\overline{x^2}\,\overline{x'^2} - (\overline{xx'})^2} \tag{3.7}$$

The rms emittance can be defined for an arbitrary particle distribution and is determined only by the rms characteristics of the beam distribution. Sometimes the total emittance of the beam is defined in terms of the rms emittance depending on the type of beam distribution.

$$\varepsilon_{total} = (n+2)\varepsilon_{rms} \tag{3.8}$$

Where, n = 2, for KV distribution; n = 3, for uniform in all three-dimensional projections; n = 4, for uniform density in 4D space, known as the 4D Waterbag distribution; n = 6, for uniform density in 6D space, known as the 6D Waterbag distribution [58].

3.4.2 Transverse emittance measurement Methods

The phase-space density and emittance of a beam are not measured directly. Transverse emittance can be determined from measurements of the particle distribution as a function of displacement and angular divergence.

3.4.2.1 Sigma Matrix method

Most transverse emittance measurement techniques use the sigma matrix transformations to get the beam emittance. Using the rms beam size and Twiss parameters, we can deduce the emittance of the beam [59]. The trajectory ellipse represented in equation 3.1 can be expressed in matrix form as

$$X^T \sigma^{-1} X = \varepsilon \tag{3.9}$$

Where,

$$X = \begin{bmatrix} x \\ x' \end{bmatrix} \tag{3.10}$$

$$X^T = \begin{bmatrix} x & x' \end{bmatrix} \tag{3.11}$$

And

$$\sigma^{-1} = \begin{bmatrix} \gamma & \alpha \\ \alpha & \beta \end{bmatrix} \tag{3.12}$$

where σ is called the sigma matrix and is defined as

$$\sigma = \begin{bmatrix} \beta & -\alpha \\ -\alpha & \gamma \end{bmatrix} \tag{3.13}$$

For any particle in the beam, the coordinate transformation from one location to the other can be expressed as

$$X_2 = RX_1 \tag{3.14}$$

Where, R is the transfer matrix between the two locations. It can be shown that the sigma matrices at two locations, 1 and 2 are related as

$$\sigma_2 = R\sigma_1 R^T \tag{3.15}$$

This can be written as

$$\begin{bmatrix} \beta_2 \\ \alpha_2 \\ \gamma_2 \end{bmatrix} = \begin{bmatrix} R_{11}{}^2 & -2R_{11}R_{12} & R_{12}{}^2 \\ -R_{11}R_{21} & 1+2R_{12}R_{21} & -R_{12}R_{22} \\ R_{21}{}^2 & -2R_{21}R_{22} & R_{22}{}^2 \end{bmatrix} \begin{bmatrix} \beta_1 \\ \alpha_1 \\ \gamma_1 \end{bmatrix} \tag{3.16}$$

Hence,

$$\beta_2 = R_{11}{}^2 \beta_1 - 2R_{11}R_{12}\alpha_1 + R_{12}{}^2 \gamma_1 \tag{3.17}$$

Or, multiplying on both sides by the emittanceε, we get

$$x_2{}^2 = R_{11}{}^2 x_1{}^2 - 2\varepsilon R_{11}R_{12}\alpha_1 + \varepsilon R_{12}{}^2 \gamma_1 \tag{3.18}$$

In principle, measuring the beam size x_2, at location 2, for three different settings of the R matrix will yield the value of the emittance by using the above equation. In practice, however, more than three independent beam size measurements are taken and the data is subjected to least-squares analysis to get a more accurate value. Two ways are commonly used to measure the emittance using this method:

1. **Moving screen method**: The simplest way is to measure the beam size at different locations. The transfer matrix of a drift space is incorporated in the above equation for different lengths of the drift spaces and the emittance is deduced.

2 **Quadrupole tuning method**: Here the beam size is measured as a function of different values of quadrupole field and the emittance is deduced.

3.4.2.2 Slit-scan method

In the slit-scan method [60], the beam is incident on a series of horizontal or vertical slits or a single slit movable in the horizontal or vertical direction. The beam is transformed into small beamlets through the slits, which are then measured by a wire or a screen kept at a known distance from the slits. These beamlets give the information about the angular distribution of the beam. The position of the slits gives the x values and the corresponding divergence, x′, can be obtained by measuring the beam profile from the wire or the screen. The schematic of the slit wire emittance setup is shown in Fig. 3.10.

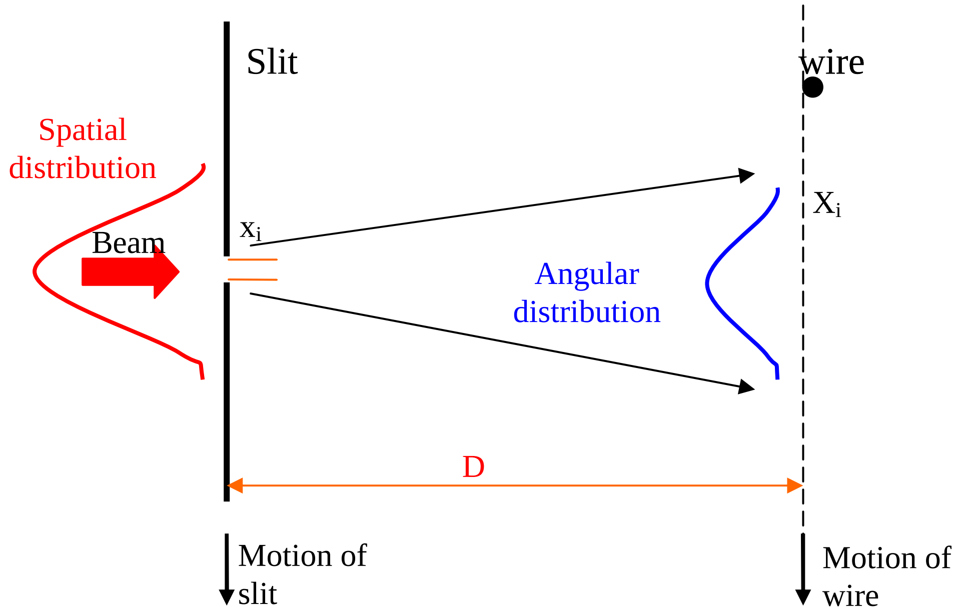

Fig.3.10: Schematic of a slit wire emittance setup.

For each position x_i of the slit, the corresponding x_i' can be calculated as

$$x_i' = \frac{X_i - x_i}{D} \tag{3.19}$$

The rms emittance can then directly be calculated from the equation

$$\varepsilon_{rms} = \sqrt{\overline{x^2}\,\overline{x'^2} - \overline{xx'}^2} \tag{3.7}$$

3.4.2.3 Pepper-pot method

In the pepper-pot method [61], the beam falls on a pepper-pot plate which has a series of holes in both x and y directions. The incident beam is divided into beamlets which is measured on the screen to give their angular distribution. As in the slit method, the rms beam emittance can be calculated directly from equation.

$$\varepsilon_{rms} = \sqrt{\overline{x^2}\,\overline{x'^2} - \overline{xx'}^2} \tag{3.7}$$

The pepper-pot method allows simultaneous measurement of the emittance in both the transverse planes.

3.4.3 Transverse emittance measurement in the LEBT

The emittance of the beams in the LEBT line was measured using the solenoid scan method and the slit scan method described below.

3.4.3.1 Solenoid scan method

The solenoid scan method [62] was used to calculate the emittance of the D^+ and He^+ beam in the test bench. A solenoid can be considered as a focusing magnet with the normalized focusing strength

$$Q = \left(\frac{eB_z}{2p} \right)^2 l_{eff} \tag{3.20}$$

where e is the electric charge, B_z is the longitudinal solenoid field, and p is the momentum of beam. If the effective length of the solenoid l_{eff} is much shorter than its focal length f_{sol}, the solenoid can be considered as a thin focusing quadrupole and the same principle as the quadrupole scan method [63] can be applied to the solenoid scan. Measuring the beam sizes at the final position for different focusing strength of the solenoid can give the emittance and Twiss parameters at the initial position.

The solenoid scan method is very similar to the quadrupole scan method, except for the coupling between horizontal and vertical motions. Rotational coordinates can be used to decouple them for an approximately round beam. Then the transfer matrix for the solenoid-drift system can be written as:

$$R = \begin{pmatrix} 1 & L \\ 0 & 1 \end{pmatrix} \begin{pmatrix} 1 & 0 \\ -Q & 1 \end{pmatrix} = \begin{pmatrix} 1-LQ & L \\ -Q & 1 \end{pmatrix} \tag{3.21}$$

The equation for the square of the rms beam size can then be solved in the terms of focusing strength of the solenoid lens as where the superscript 1 denotes the location of the BPM and 0 is at the beginning of the solenoid:

$$\begin{aligned} \sigma_{11}{}^{1} &= \sigma_{11}{}^{0} L^2 Q^2 - 2(L\sigma_{11}{}^{0} + L^2 \sigma_{12}{}^{0})Q \\ &+ (\sigma_{11}{}^{0} + 2\sigma_{12}{}^{0} L + L^2 \sigma_{22}{}^{0}) \end{aligned} \tag{3.22}$$

Horizontal and vertical beam profiles are measured using the wire scanner. The solenoid was optimized to locate the beam waist at the wire scanner and then the beam size is scanned around that value. A Gaussian distribution was fitted into the beam profile. The fitting coefficient, R^2, in all cases was greater than 0.98. At each value of the solenoid current, 10 readings of the beam profile were taken and averaged to give the beam size. The images were analyzed off line to obtain the rms beam size. A typical beam profile obtained from the wire scanner is shown in Fig. 3.11. (a) and a Gaussian fitted to the beam profile is shown in Fig. 3.11. (b).

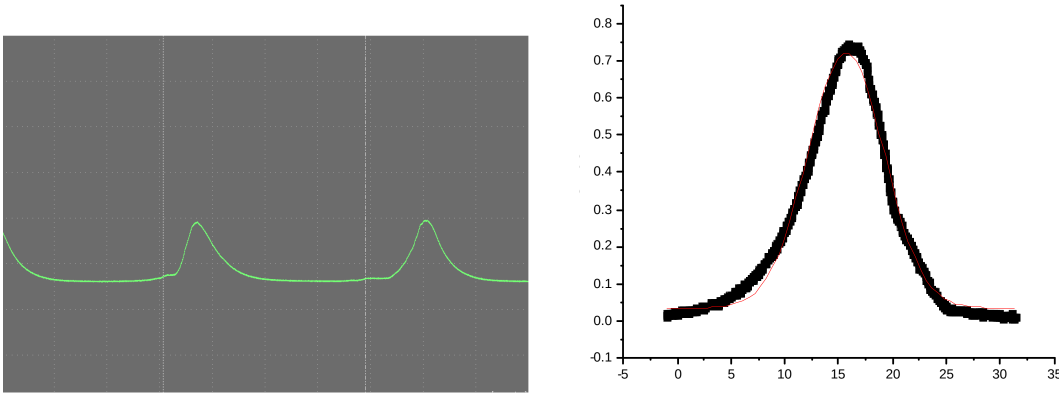

Fig. 3.11: (a). Beam profile obtained from BPM. (b). Gaussian fitted to the beam profile.

After acquiring images for all solenoid scan steps, the RMS transverse emittance was calculated from the coefficients after a least square fitting of the square of the beamsize as a function of the solenoid focusing strength Q as shown in Fig. 3.12 and Fig. 3.13. for Helium and deuteron beams. The normalized rms emittance of Deuteron beam was calculated to be 1.66 π cm mrad and that of Helium beam was calculated to be 0.178 π cm mrad by this method.

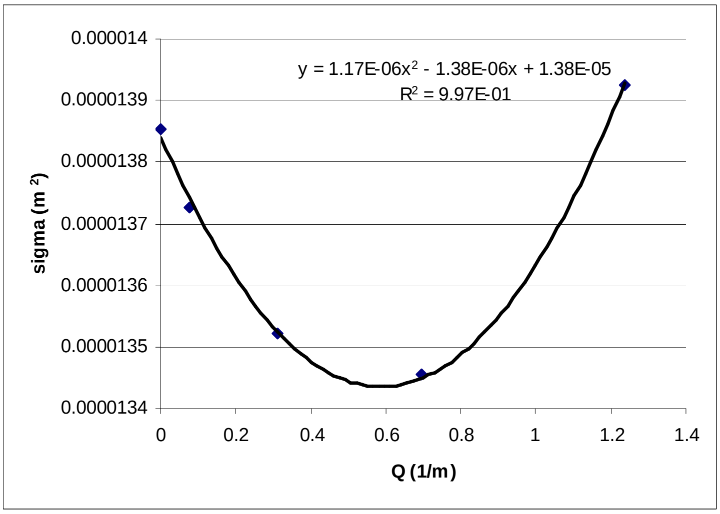

Fig.3.12: A square of beam radius plotted as a function of magnetic strength of solenoid lens for Helium beam

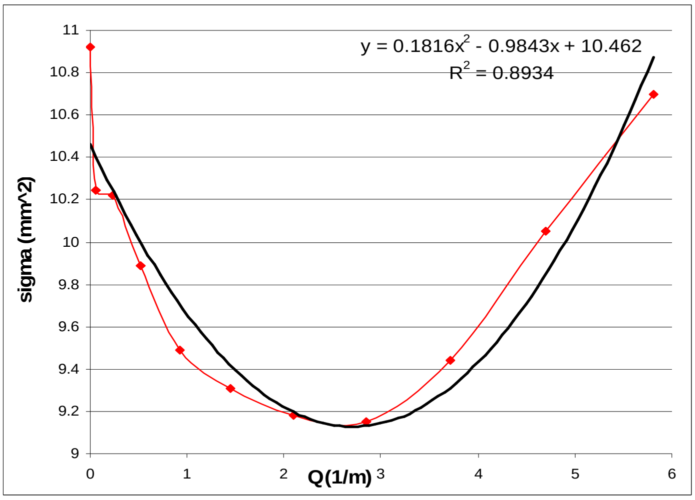

Fig.3.13: A square of beam radius plotted as a function of magnetic strength of solenoid lens for Deuteron beam.

3.4.3.2 Slit Scan Method

Another method that was used for the measurement of transverse beam emittance in the LEBT was the slit-scan method. A slit-wire scanner based emittance measurement setup was developed for the measurement of beam emittance [64]. It consists of movable slits of 0.35 mm width and movable thin wire of 0.05 mm diameter. The spatial beam distribution was scanned by the slit while the angular distribution was scanned by the wire scanner which was located at a distance of 140 mm from the slit. A 1 μm precision linear motion mechanism was provided for movement of the slit and the wire. The beam emittances in both transverse directions are measured in a simultaneous fashion in this setup. The schematic of the emittance measurement setup is shown in Fig. 3.14. The emittance of H^+ and D^+ beams was measured using this setup.

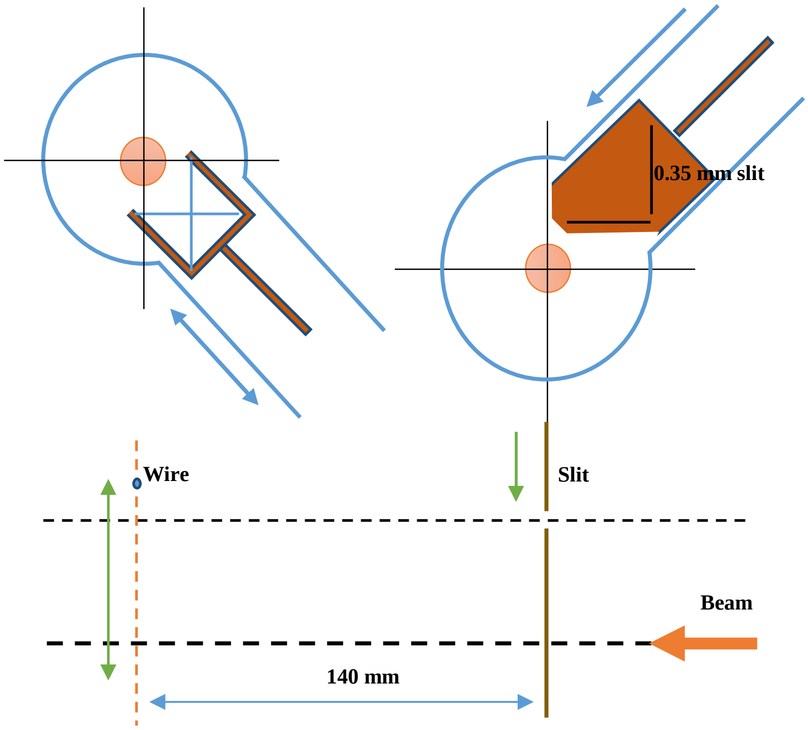

Fig. 3.14: Schematic of the slit wire emittance measurement setup.

A typical wire scan data for different slit positions from the emittance measurement setup for 100 μA, 50 keV D^+ beam is shown in Fig. 3.15. The raw data shows double humps which indicate the presence of different species other than D^+ in the beam. The raw data is Gaussian fitted for multiple peaks and the D^+ ion species data is extracted out.

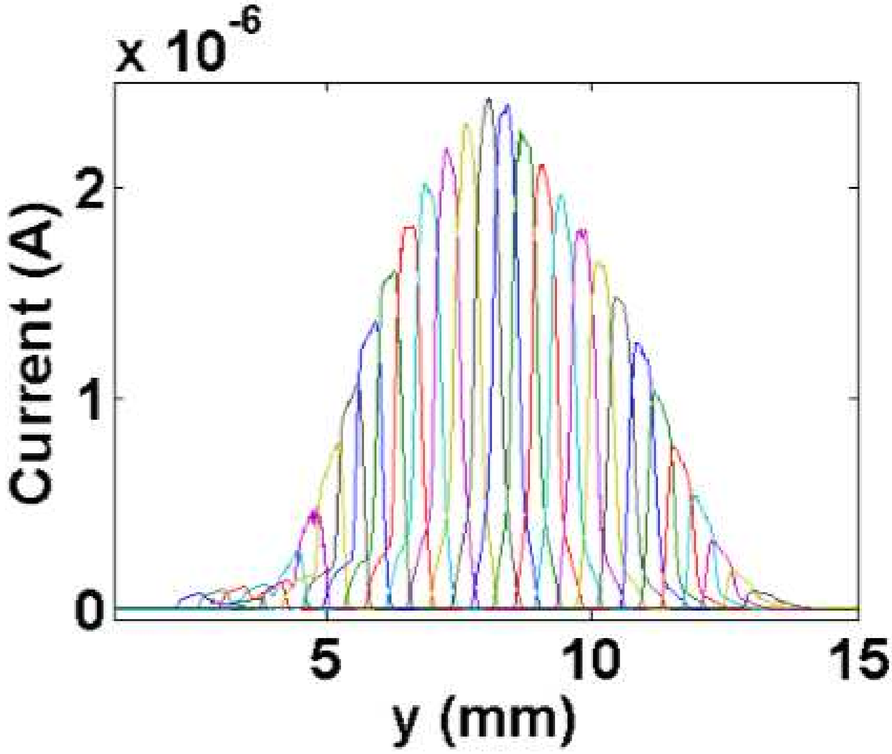

Fig. 3.15: Typical wire scan data at different slit positions for 100 μA, 50 keV D^+ beam.

This data is analyzed and values of x′ are calculated from equation 3.19. The beam rms emittance is then calculated using equation 3.7. The 2D emittance contour plots and the 3D beam distribution plots in phase space are then plotted. In Fig. 3.16. (a), both the rms (inner ellipse) and 100% emittance (outer ellipse) are plotted. Fig. 3.16. (b) shows the beam emittance 2 D contour plot while in Fig. 3.16. (c) the 3 D beam distribution in phase space is plotted. These results are plotted for 100 μA, D^+ ions. Similar measurements and analysis was done for H^+ beam also.

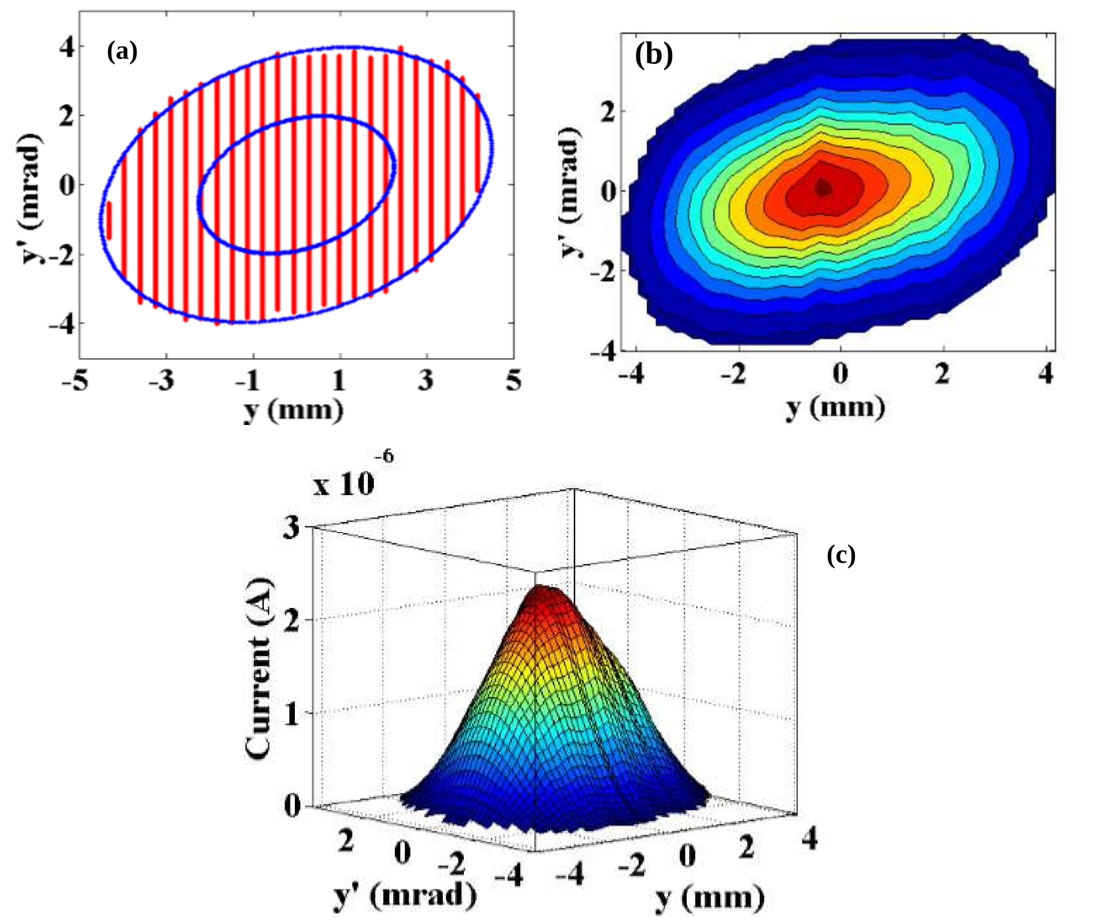

Fig. 3.16: (a) Beam emittance plot (y-y’) of 100 μA, D^+ ions. (b) Beam emittance 2D contour plot. (b) 3D distribution of beam in phase space. (c) 3D distribution of beam in phase space.

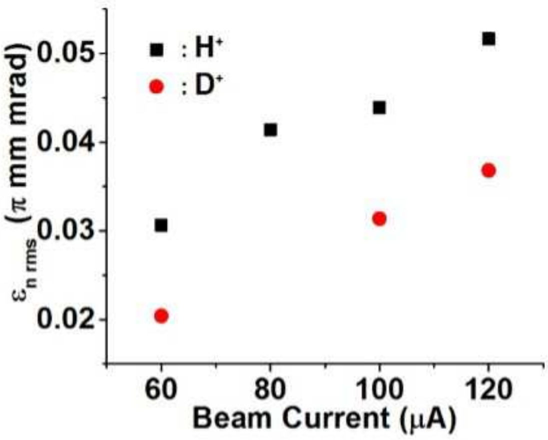

Fig. 3.17. Variation of normalized RMS emittance of H^+ and D^+ ions with ion beam current.

Fig. 3.17. shows the variation of normalized rms emittance of H^+ and D^+ beams as a function of beam current. The beam energy for both the ion species is 50 keV. H^+ has larger emittance than D^+ ions and the emittance increases with increase in beam current.

The acceptance value of normalized RMS emittance for the 400 keV RFQ is 0.02 π cm mrad for D^+ ions and hence at these low beam currents (~100 μA) the emittance of the input beam is well within the acceptance value of RFQ.

3.4.4 Discussion of the results

It can be seen that the emittance measurement using the solenoid scan gives a much higher value of the emittance as compared to the slit wire method. There are two main reasons for this. The beam coming from the ion source contains different species in addition to the main beam as can be seen in Fig. 3.13. While these have been separated during the analysis in slit wire method, it is not possible to do the same for the solenoid scan method. So the emittance calculated using the solenoid scan method is essentially the emittance of the entire beam containing all the species coming from the ion source. Also for the solenoid scan method, the beam has to be symmetric. However, there is some asymmetry in the beam which results in emittance values not so accurate. Hence for this LEBT system, the slit wire method is a more accurate way of calculating the emittance.

3.5 Summary and Conclusions

A 400 keV deuteron RFQ based linac has been built at BARC. It consists of a rf ion source, a 400 keV RFQ for D^+ beams and a low energy beam transport (LEBT) line to match the beam from the ion source to the RFQ. The LEBT was designed using 2 solenoids for focusing the beam. Based on the simulations, a LEBT test bench has been setup at Van de Graaff to validate the simulations and focusing of the solenoids that have been designed and fabricated. Experiments to measure the beam emittance and transmission in the line were done. The beam emittance measurement of proton, deuteron and helium beams was done using the solenoid scan and the slit wire method. The emittance value for the Deuteron beam is well within the acceptance value for the RFQ. Using this LEBT line 50 keV deuteron beam has been matched to the RFQ and accelerated to 400 keV.

Chapter 4

Physics studies of a high intensity proton linac

4.1 Introduction

High-power proton linacs are today being developed for a variety of applications such as accelerator driven systems (ADS) for transmutation or energy production [ref], neutron spallation source for condensed matter study, neutrino factories, muons colliders, production of rare isotope beams for nuclear physics studies etc. These linear accelerators for these applications are required to deliver proton beam of up to several MW to several tens of MW power and operate with CW or pulsed high intensity beams. In particular, accelerator driven systems [1] have evoked considerable interest in the nuclear community around the world because of their capability to incinerate the MA (minor actinides) and LLFP (long-lived fission products) radiotoxic waste and utilization of Thorium as an alternative nuclear fuel. In the Indian context, due to our vast thorium resources, ADS is particularly important as one of the potential routes for accelerated thorium utilization and the closure of the fuel cycle [2].

One of the main sub-systems of ADS is a high energy (~1 GeV) and high current (~30 mA) CW proton linac. The primary concern in building such high-power linacs is the beam losses, which could limit the availability and maintainability of the linac and various subsystems due to excessive activation of the machine. A careful beam dynamics design is therefore needed to avoid the formation of halo that would finally be lost in the linac or in transfer lines. In addition to this, the electrical efficiency, reliability and beam loss rate for such a system needs to be improved to a great extent compared to the existing high energy linacs. In India, it was, therefore, planned to take a staged approach towards development of the accelerator technology for ADS, dividing it into 3 sections: namely, 20 MeV, 100-200 MeV and 1 GeV [23].

In the first phase, BARC has initiated the development of Low Energy (20 MeV) High Intensity Proton Accelerator (LEHIPA) [24] as front-end injector of the 1 GeV accelerator for the ADS programme. Physics design studies have also been done for a 1 GeV proton linac for our ADS program. Proton beams are accelerated up to 100 MeV using normal conducting and upto 1 GeV using superconducting elliptical cavities.

4.2 Design choices

One of the most important and challenging part in the ADS system is the high power proton accelerator. While efforts are on all over the world to build such a linac, there is no such linac yet that is operating. The main requirements from the accelerator are

1. High Reliability – In order to get uninterrupted power from the reactor, the accelerator has to be highly reliable. It should be able to operate continuously for long periods of time without beam trips. For high reliability it is important that the accelerator design should be conservative and based on proven and already demonstrated structures.
2. High Beam Power – The accelerator for ADS should be able to deliver tens of MW of power. Typically about 1 GeV energy and beam currents of > 10 mA are considered.
3. CW operating mode – CW operating mode is required to avoid undesirable thermal shocks to the fuel elements which results from the pulsed nature of the beam.
4. High conversion efficiency – The conversion efficiency of electrical power to beam power should be as high as possible. For this, superconducting structures should be used and the normal conducting structures should be optimized for high shunt impedance.
5. Minimum beam loss – Any loss of beam in the accelerator will lead to activation of the accelerator components which will prevent the service staff from accessing the accelerator for maintenance. For this the beam loss should

be restricted to less than 1watt/m [65]. The beam should therefore be free from halo formation which will manifest as beam loss at high energy.

6. Easy maintenance and serviceability.

The architecture of the accelerator should be based on these features. High energy synchrotrons are ruled out because of their pulsed nature. The accelerators that can give a CW beam are cyclotrons and linacs. However, cyclotrons can deliver maximum beam currents of only 5- 10 mA, which makes linacs the more popular choice of accelerator for ADS application.

The design studies involve choice and optimization of various accelerating structures and the beam dynamics studies through the linac. The low-energy section consists of a high-intensity ion source that delivers beams of few tens of keV energy. Almost all linacs being designed today use the radio-frequency quadrupole (RFQ) [4,5] to accelerate the high current beam from the ion source to a few MeV beam energy. Particular care must be given to the linac front end which must deliver a high quality beam in order to have low beam losses at higher energies where they are most dangerous. The intermediate-energy structures accelerate the beam to about 100 MeV. These are usually normal-conducting drift-tube Linac structures (DTL, SDTL, CCDTL) [66]. However, superconducting structures, like spoke type resonators and half wave resonators, are also being contemplated especially for CW beams. The high energy structures accelerate the beams from few hundred MeV to GeV energies. At these energies, superconducting RF technology seems to be the best option in order to design a cost-effective machine in terms of both capital and operational costs and superconducting multicell elliptical cavities are used for acceleration in this energy range.

In the present design, the RFQ is chosen to accelerate the 50 keV, 30 mA proton beam to 3 MeV. After the RFQ, the Drift Tube linac (DTL) is a used as it is considered a viable structure with high shunt impedance for accelerating the 3-MeV beam from the RFQ where the beam energy is still low and hence regular focusing is needed. The RFQ energy could be increased, but the net system cost would increase as a result. It will also increase the fabrication difficulties as RFQ is a complex structure with very high tolerances. A transition to a CCDTL structure is made at 40 MeV because this structure, is believed to be more stable than the DTL structure as it operates in the π/2 mode and has a favorable shunt impedance at this energy. The effective shunt impedance per unit length [67] is an important figure of merit used to characterize an accelerating cavity. It is a measure of the energy gain per unit power dissipation and is defined as:

$$ZT^2 = \frac{(E_0 T)^2}{P/L}$$

Where, E_0 is the average axial electric field, T is the transit time factor, P is the average power dissipation and L is the length of the cavity. The CCDTL also allows the focusing quadrupoles to remain outside the linac tank, facilitating alignment and diagnostics. The drift-tube structure also becomes simpler as the quadrupoles are not housed inside the drift tubes. At 100 MeV, transition is made to superconducting cavities which then accelerate the beam to 1 GeV. Superconducting linear accelerators are now considered as an option for high intensity projects around the world. They offer various advantages such as reduction in ac power, in linac length because of the higher accelerating gradients, and in the number of klystrons and associated rf power systems. Furthermore, there is an increased safety margin against radio activation from beam losses that would impede hands-on-maintenance and would limit the availability. This latter advantage is the result of the higher gradients that increase the longitudinal focusing, larger bore radius and the improved vacuum in the cryogenic environment of the superconducting accelerator. The superconducting linac is composed of three sections made of 5-cell elliptical cavities designed for geometric beta of 0.49, 0.62 and 0.8.

4.3 Design criterion

The linac for ADS is required to deliver 30 mA of CW proton beam at 1 GeV energy. The main design criterion for such a linac is low beam loss and control of transverse emittance. An r.m.s. normalized emittance of 0.2 π mm mrad is considered to be a reasonable goal for the H^+ ECR ion source and hence has been assumed for the simulations. The reduction of beam losses is a major concern in the design of the linac in order to avoid activation of the machine and irradiation of the environment. Other important design factors are the need to avoid generation of beam halos, current independent operation and tuning, and high operational availability.

The linac is designed using both normal-conducting (NC) and superconducting (SC) accelerating-cavity structures. A normal-conducting linac for low-velocity particles combined with a superconducting linac for high-velocity particles utilizes the advantages of both technologies. High-current, low-velocity proton linacs have demanding focusing requirements to control space-charge forces, which can be provided straightforwardly with present normal-conducting structures. But, focusing requirements relax with increasing velocity and are compatible with the longer-period focusing lattice of a high-velocity superconducting linac.

The main design criterions for such a linac are:

- Low beam loss (<1 Watt/m) to allow hands-on-maintenance of the entire linac
- Low emittance increase
- Avoid halo formation

For this, the following design philosophy was adopted

- Maintaining the transverse and longitudinal phase advances per unit length constant at all transitions between the structures to provide a current independent match into the next structure [68]. For this the quadrupole gradients and accelerating electric fields are varied between the structures.
- Matching the transverse and longitudinal phase spaces at the end of one structure to the acceptance of the next structure by using carefully designed transport lines.
- Keeping the zero current phase advance per period (σ_0) in all the planes below 90 degrees. This is done to avoid envelope instability which causes emittance increase and beam loss.
- Having smooth transitions throughout the linac in terms of RF frequencies, accelerating structures, focussing period length etc.

4.4. Linac Design

A schematic of the designed linac is shown in Fig. 4.1.The linac for ADS consists of an RFQ followed by a DTL, CCDTL and SC linac. The RFQ accelerates the beam from 50 keV to 3 MeV and the DTL takes the beam to 40 MeV. The CCDTL accelerates the beam to energy of 100 MeV. The beam is then accelerated to 1 GeV using 5 cell supererconducting elliptical cavities. While the RFQ and DTL operate at 352.21 MHz, the operating frequency of CCDTL and SC linac is 704.42 MHz. [25,69]

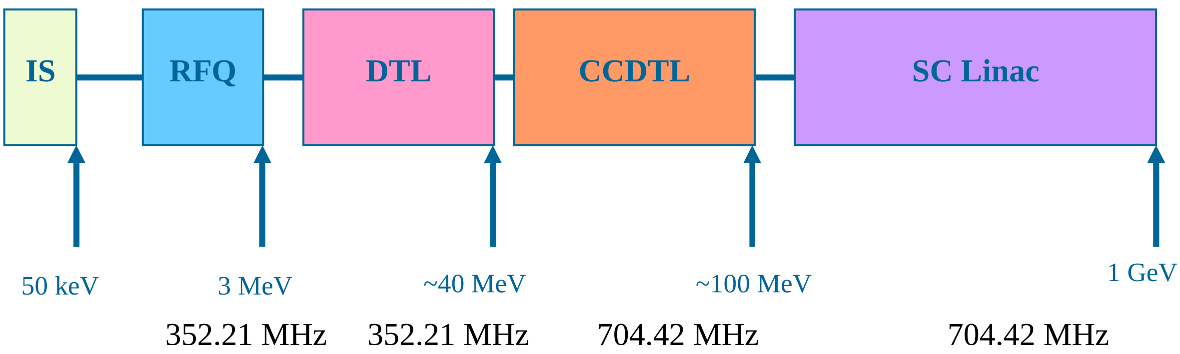

Fig.4.1: Schematic of the 1 GeV Linac for ADS.

End to end simulations of the linac have been done using PARMTEQM, PARMILA and TRACE3D codes. The transverse and longitudinal phase advances per unit length are maintained constant at all transitions between the structures to provide a current independent match into the next structure. For this the quadrupole gradients and accelerating electric fields are varied between the structures.

The details of the accelerator design are discussed in the subsequent sections.

4.4.1 Ion Source & LEBT

The front end injector consists of the ECR ion source, the low energy beam transport (LEBT) line and the RFQ to accelerate the beam to 3 MeV.

The ion source will be an ECR ion source and will deliver 30 mA proton beam at 50 keV energy. The main challenge is to provide a high brightness beam i.e beam at low emittance and high intensity.

The main criterion for the design of the LEBT was to minimize the emittance growth with minimum beam loss. With this criterion, in our design the beam from the ion source is matched to the RFQ using two solenoids for focusing the beam. Solenoids are preferred over quadrupoles because they focus simultaneously in x and y planes and produce a round beam which is required at the RFQ input. The computer code TRACE2D was used for an initial design of the LEBT for 50 keV, 1 mA DC H^+ beam. The LEBT was used to transport the phase space ellipse at the exit of the ion source to the entrance of the RFQ and match it to the acceptance of the RFQ. The RFQ match point was obtained by back tracing the beam from the shaper to the radial matching section of the RFQ in TRACE2D. Then the beam from the ion source was matched to the RFQ match point using TRACE2D to get a mismatch factor of zero in x and y. This matching was done using 2 solenoids and 3 drift spaces. The total length of the LEBT is about 3 m.

4.4.2 RFQ

After the source and the LEBT section, the beam is accelerated to 3 MeV by a RFQ at 352.2 MHz. RFQs have the capability of focusing, bunching and accelerating the beam simultaneously. At low energies (β ~ 0.01 to 0.08), RFQ is most efficient structure for accelerating the beam with high transmission and low emittance growth. A Radio Frequency Quadrupole accelerator consists of two pairs of parallel electrodes, which produce an electrostatic quadrupole field on the axis. In order to generate an axial field component for acceleration, the electrodes are modulated longitudinally and one pair of electrodes is longitudinally shifted with respect to the other pair by 180^o, so that the distance from the axis of the vertical vanes at its minimum if denoted by a, the horizontal vanes will be ma apart from the axis where m is the modulation parameter and its value greater than one. This electrode geometry produces a longitudinally varying axial potential which gives rise to a longitudinal electric field. The beam is accelerated by longitudinal RF electric fields and focused by RF electric-quadrupole fields.

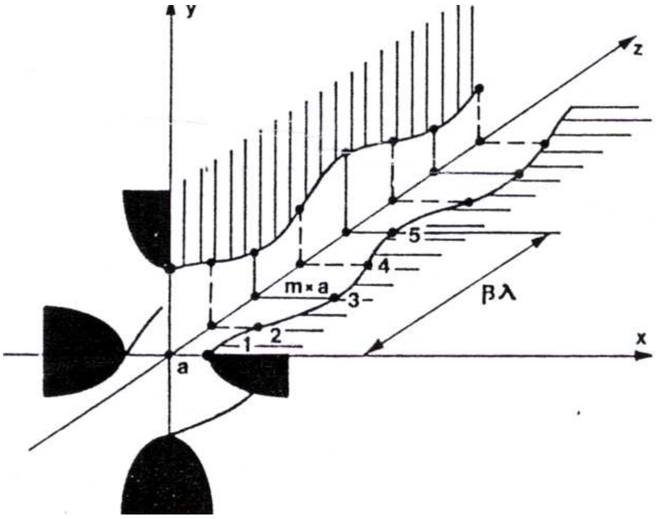

Fig 4.2: Modulations along the length of the RFQ.

Since the field is alternating at RF frequency, the particles gain energy if they are in synchronism with the field. The modulation controls the strength of the longitudinal bunching and accelerating field while only slightly perturbing the strength of the transverse focusing field. The transverse focusing field is sustained along the entire length of the RFQ to maintain focus, and the longitudinal field is increased slowly along the axis to adiabatically bunch and capture the beam and then to accelerate it to full energy.

The RFQ operating at 352.21 MHz accelerates the 30 mA proton beam from 50 keV to 3 MeV. In this design the vane voltage has been kept constant, keeping the peak surface field less than 1.8 times the Kilpatrick limit. The cavity design was done using SUPERFISH [49]. The electric field lines in one quadrant of the RFQ are shown in Fig.4.3. The transmission at the end of the RFQ is 97.5 %. The parameters of the RFQ are shown in Table 4.1. The total length of the RFQ is 3.52 m and the total rf power requirement is 385 kW which includes 88.5 kW of beam power.

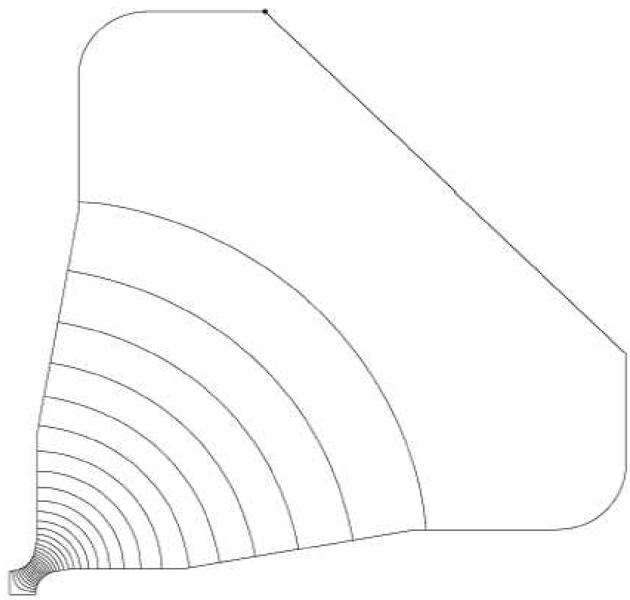

Fig.4.3: Electric field lines in one quadrant of the RFQ.

Table 4.1. Parameters of the RFQ.

Parameters	**Value**
Frequency	352.21 MHz
Input energy	50 keV
Output energy	3 MeV
Input current	30 mA
Transverse emittance	0.02/0.023 π cm-mrad
Synchronous phase	-30^0
Vane voltage	76.7 kV
Peak surface field	32.51 MV/m
Length	3.52 m
Total RF power	385 kW
Transmission	95.9 %

4.4.3 Drift Tube Linac (DTL)

The Drift Tube linac is a resonant cavity excited in TM_{010} mode. It consists of a succession of drift tubes separated by gaps. The drift tubes shield the beam from the electric field when it is in the decelerating phase. Quadrupoles inserted in the drift tubes provide focusing. The DTL is used for ions in the velocity region near $0.05 < \beta < 0.4$, where the space charge forces are considerable. The schematic of DTL is shown in Fig.4.4. The advantages of DTL are:

1. It is an open structure without cell end walls, generally resulting in high effective shunt impedance.
2. Focusing quadrupoles within the drift tubes provide strong focusing and permit high beam current limits.

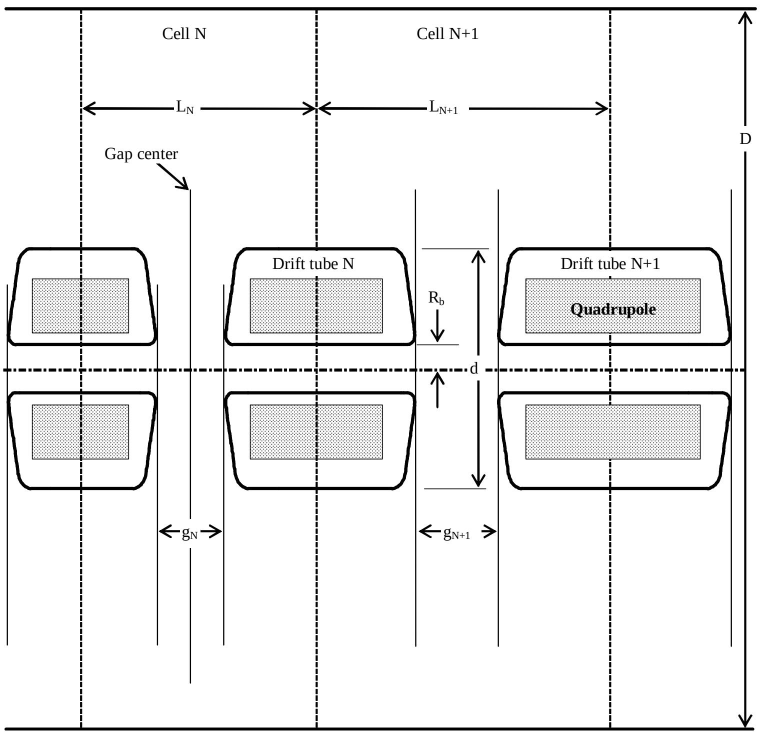

Fig.4.4: Schematic of the drift tubes in the DTL.

4.4.3.1 Electromagnetic Design

The program DTLFISH in the POISSON SUPERFISH code distribution is used to design the cavity shape and compute surface fields and rf power losses. DTLFISH sets up the geometry for drift-tube linac (DTL) cells. Fig.4.5.(a) shows the basic outline of DTL cavity generated by DTLFISH and Fig.4.5.(b) shows the detailed geometry of the drift tube. The DTL cell is a figure of revolution about the beam axis. DTLFISH assumes a symmetric cell, and therefore sets up SUPERFISH runs for only half the cell. The symmetry plane is in the gap center between the two drift-tube noses. DTLFISH tunes the cell by adjusting the cavity diameter (D), drift-tube diameter (d), gap (g), or face angle (α_f).

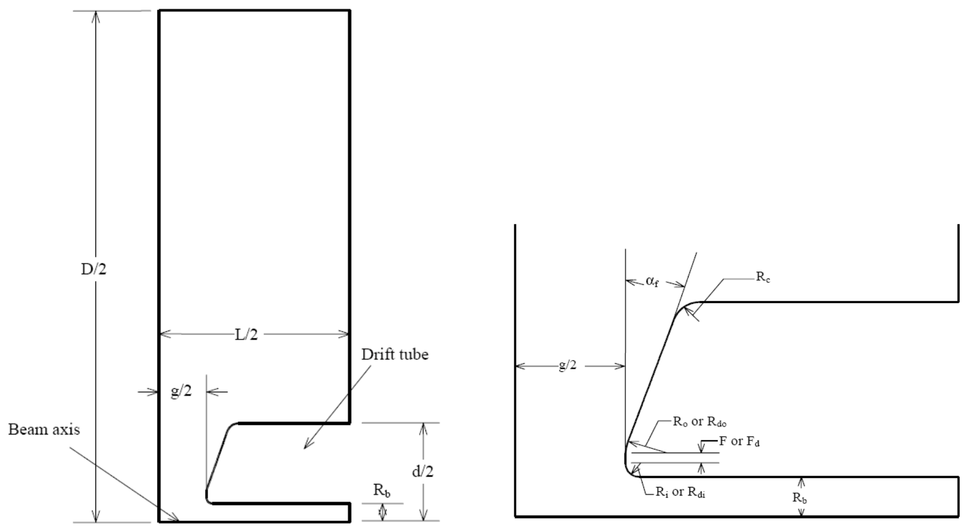

Fig.4.5:(a). The DTL half cell set up by the code DTLfish. (b). Detail near the drift-tube nose.

The DTL cavity was designed with the following design criteria:

- To have good shunt impedance
- To have a constant tank diameter, bore radius and drift tube diameter along the structure for ease of fabrication.
- To have space for quadrupoles inside the drift tubes.
- To avoid voltage breakdown by keeping peak surface field below $0.8E_k$.

To design the DTL cavity first the cavity diameter was optimized. The idea was to use the same tank diameter for all the DTL tanks i.e in the entire energy range. For this, the effect of varying the tank diameter on the various figure of merits of the cavity viz. effective shunt impedance, the peak surface electric field, power dissipation etc. at different energies was studied.

It can be seen from Fig.4.6. that in the lower energy range i.e. 3-20 MeV, the optimum diameter is around 53 cm and in the higher energy range i.e. 20-50 MeV, the optimum diameter is around 51 cm. As a compromise for all energies a tank diameter of 52 cm was chosen.

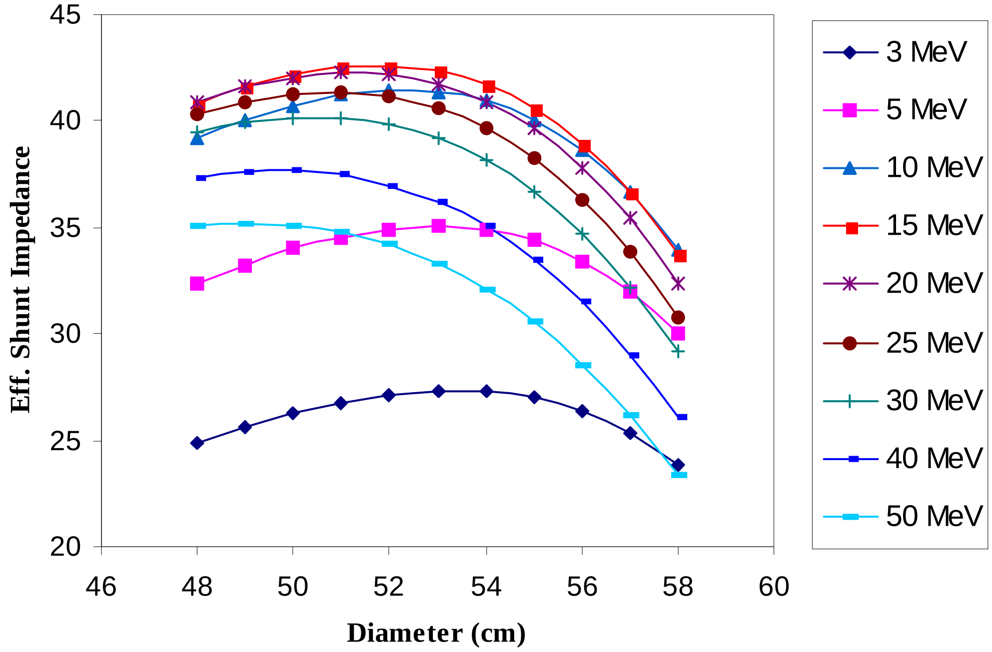

Fig.4.6: Variation of effective shunt impedance of the DTL with diameter at different energies.

As the face angle is increased the effective shunt impedance also increases at all energies. This can be seen in Fig.4.7. However larger face angles also reduce the space available for the focusing magnets in the drift tubes. Hence the face angle is kept 0° from 3 MeV to 20 MeV where the drift tube lengths are small. Beyond 20 MeV it is increased 10°, where the drift tubes become long enough to accommodate the quadrupoles. This increases the effective shunt impedance at 20 MeV as can be seen in Fig.4.8. The shape of the drift tubes and the electric field profile in the DTL at 3 MeV, 20 MeV and 40 MeV is shown in Fig.4.11.

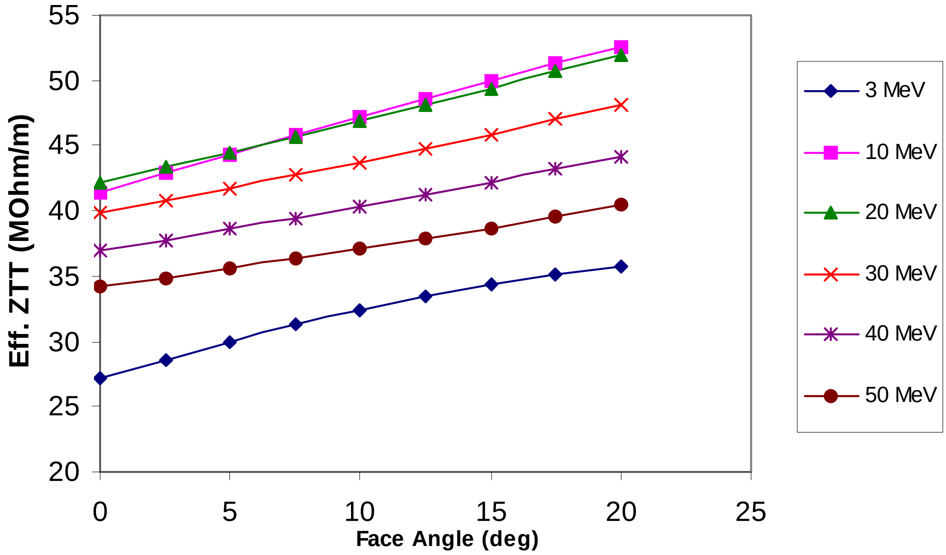

Fig.4.7: Variation of effective shunt impedance in the DTL with face angle at different energies.

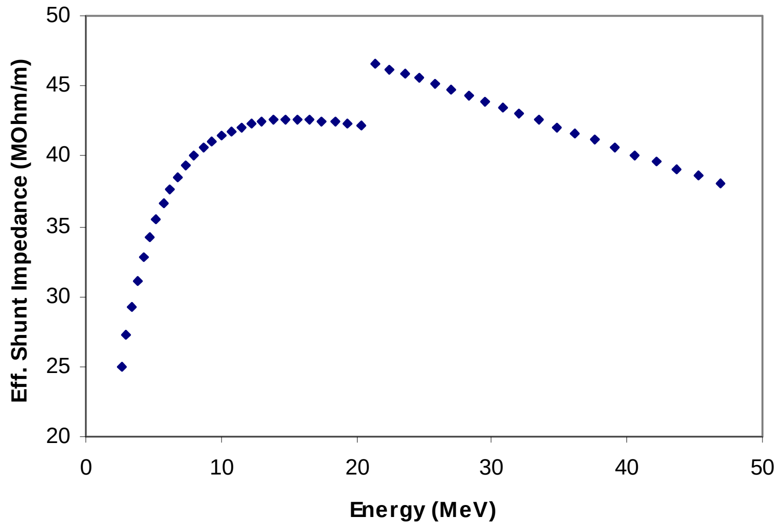

Fig.4.8: Variation of effective shunt impedance in the DTL with energy.

The drift tubes must be large enough to accommodate quadrupole magnets for focusing and to provide space for cooling of drift tubes which is essential in CW operation. As can be seen from Fig.4.9., the effective shunt impedance decreases with increase in the drift tube diameter. As a compromise between the two, the drift tube diameter was chosen to be 12 cm.

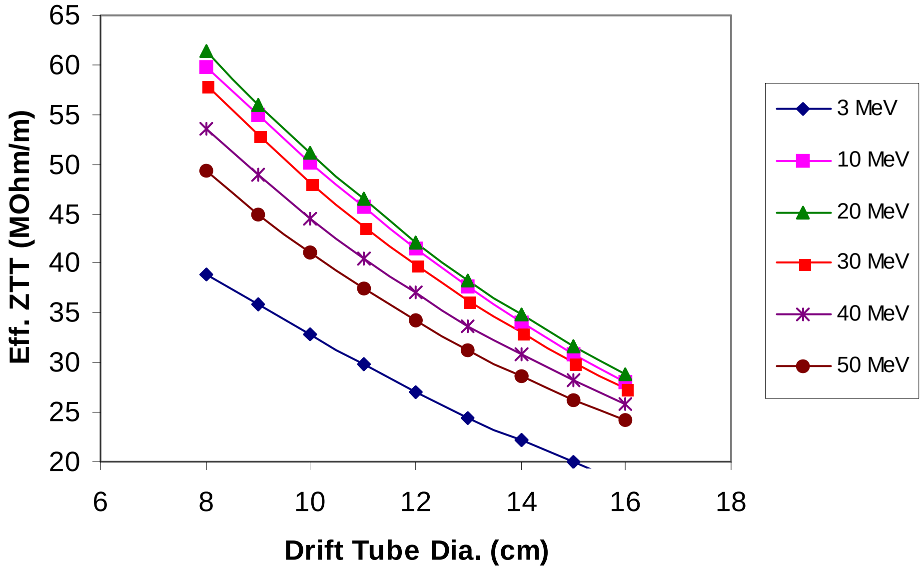

Fig.4.9: Variation of effective shunt impedance in the DTL with Drift tube diameter at different energies.

The effective shunt impedance decreases with increase in bore radius as can be seen from Fig.4.10. Hence a smaller bore radius is preferred. But in order to ensure low beam losses the aperture must be much larger than the rms beam size. So the aperture is chosen to be 1.1 cm.

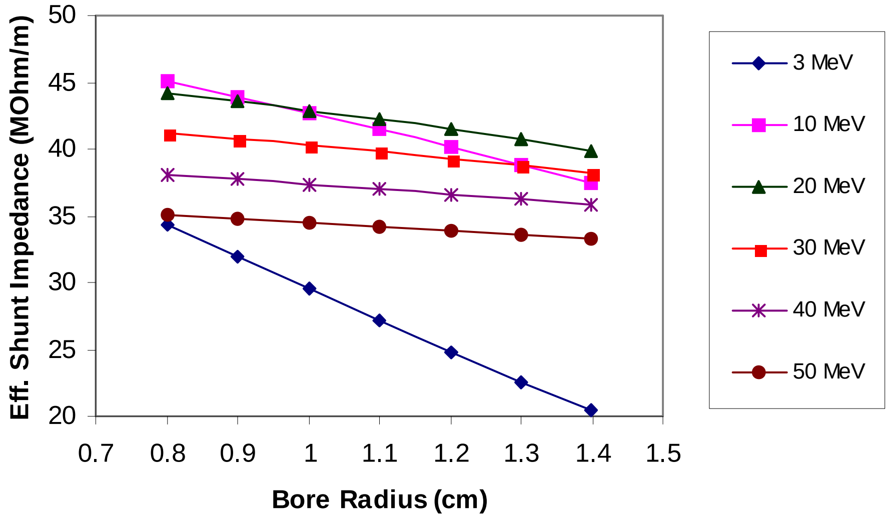

Fig.4.10: Variation of effective shunt impedance in the DTL with bore radius at different energies.

The final parameters of the designed DTL cavity are summarized in Table 4.2.

Table 4.2. Parameters of DTL cavity.

Parameter	**3-20 MeV**	**20-40 MeV**
Frequency (MHz)	352.21	352.21
Tank Diameter D (cm)	52	52
Drift Tube Diameter d (cm)	12	12
Bore Radius R_b(cm)	1.0	1.0
Face Angle α_f (degrees)	0	10
Corner Radius R_c(cm)	1.5	1.5
Inner Nose Radius R_i(cm)	0.5	0.5
Outer Nose Radius R_o(cm)	0.5	0.5

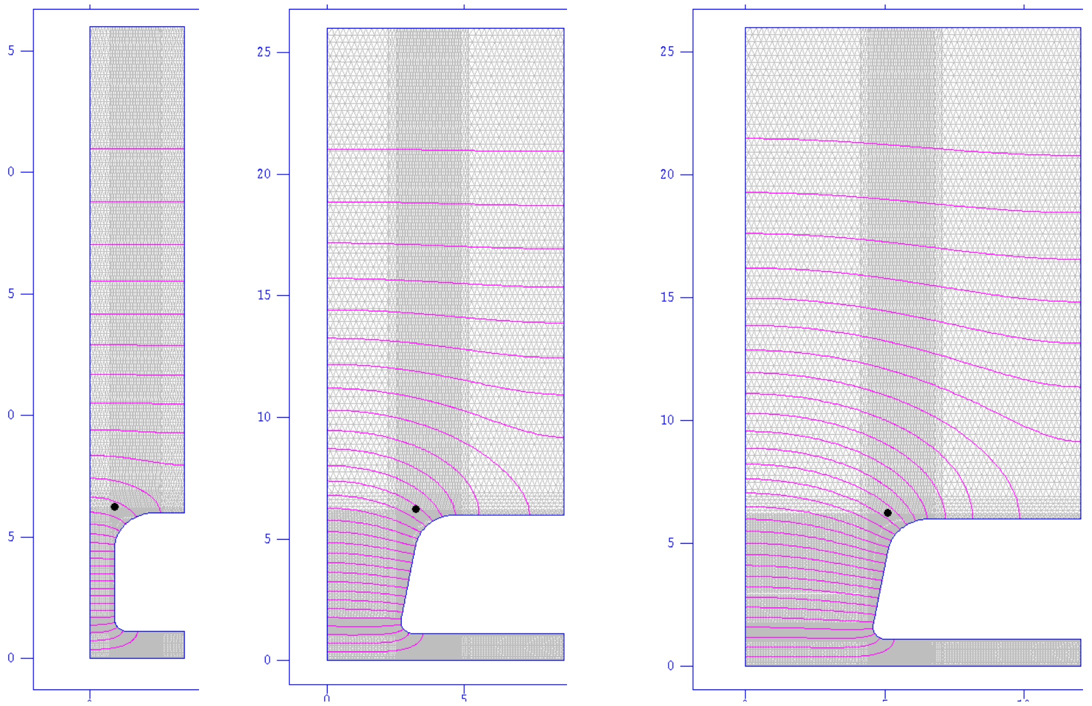

Fig.4.11: Electric field profiles in the DTL at 3 MeV, 20 MeV and 40 MeV.

4.4.3.2 Beam Dynamics design

The beam from the RFQ is accelerated to ~ 40 MeV using DTL at 352.21 MHz. The 3 MeV beam from the RFQ is matched into the DTL using the Medium Energy Beam Transport Line (MEBT), which consists of 4 quadrupoles for transverse matching and 2 rf gaps for longitudinal matching. The matching was done using TRACE 3D [33] code. The beam dynamics design in the DTL has been done using PARMILA [70]. FFDD lattice is used in the DTL for transverse focusing. For this lattice the quadrupole gradient required to match the transverse phase advance between RFQ and DTL, for current independent matching, comes out to be ~ 43 T/m. This can be achieved by permanent magnet quadrupoles placed inside the drift tubes. The focusing lattice period is $4\beta\lambda$ throughout the DTL. The total length of the DTL is 22.66 m and the RF power required is 1.97 MW. The DTL will be built in 4 tanks. The axial electric field is kept constant at 2.5 MV/m in all the tanks. The beam dynamics parameters of the DTL are summarized in Table 4.3.

Table 4.3. Beam Dynamics parameters of DTL tanks.

DTL Tank No.		**1**	**2**	**3**	**4**
Energy Range (MeV)		3 - 11.14	11.14-19.29	19.29–29.18	29.18-40.12
No. of Cells		52	33	31	30
Synch. Phase (deg)		-30	-30	-30	-30
Acc. Grad. (MV/m)		2.5	2.5	2.5	2.5
Total Power (kW)		470	429.43	498.93	574.07
Tank Length (cm)		512.15	495.15	585.47	673.52
Trans. Emit (cm mrad)	**X**	0.02293	0.02295	0.02293	0.02291
	Y	0.02263	0.02261	0.02263	0.02265
Long. Emit (deg MeV)		0.10577	0.10594	0.10601	0.10608

The beam profile through the DTL is shown in Fig.4.12 and the beam profile in transverse phase spaces, transverse coordinate space and longitudinal phase space at the end of the DTL is shown in Fig. 4.13.

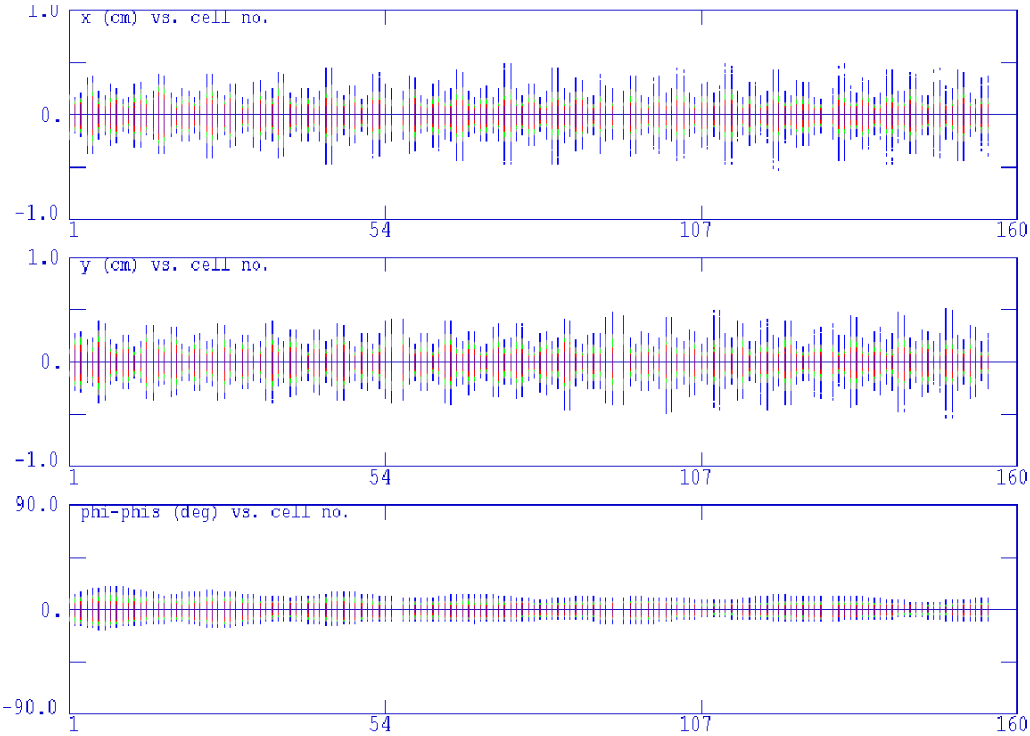

Fig.4.12. Beam Profile through the DTL

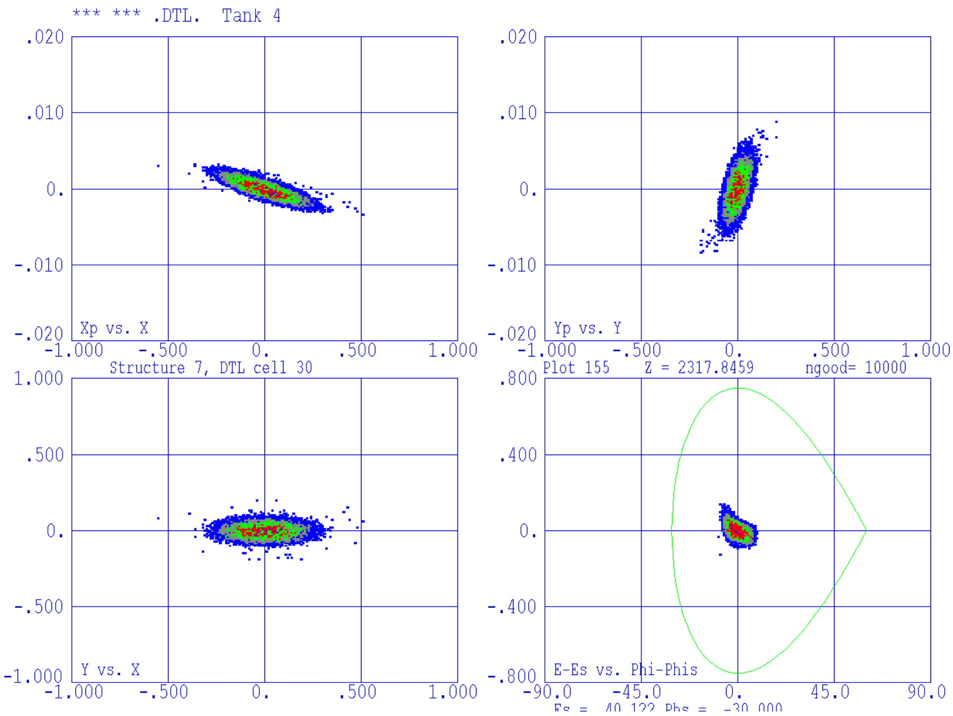

Fig.4.13 : Beam profile in (a). Transverse phase space in x (b) Transverse phase space in y (c). Transverse coordinate space xy and (d). Longitudinal phase space at 40 MeV.

4.4.4 Coupled cavity drift tube Linac (CCDTL)

In the medium energy range, the velocity of the particles is high enough to allow long drifts between focusing elements. The CCDTL structure is suitable for use in this energy range. It is made of groups of small 2-gap DTL tanks resonantly coupled to each other by single-cell bridge couplers, with the quadrupoles placed between the tanks. The single DTL tanks operate in the 2π-mode, while the chain of tanks operates in the more stable π/2 mode, with no field in the bridge-coupler cavities. Fig.4.14. shows the schematic of a CCDTL. In this structure, the separation between the two consecutive gaps within the same cavity is βλ, while the separation between the last gap of a cavity and the first gap of the next cavity is βλ/2. This ensures that the particle is in synchronization with the accelerating field in each gap. Advantages of using CCDTL are:

- Since the quadrupoles are not housed inside the drift tubes, this allows more flexibility on the drift tube design which can now be optimized for higher shunt impedance.
- The resonating mode is the π/2 which is an intrinsic stable mode.

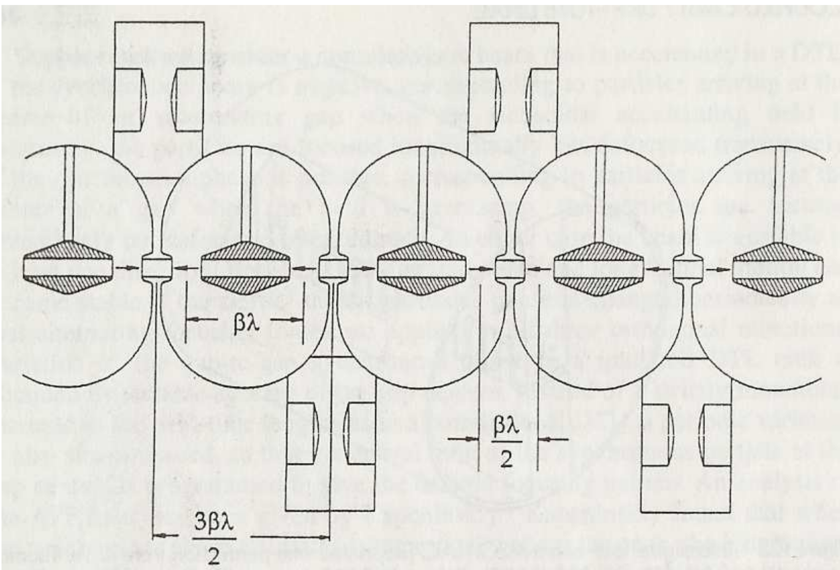

Fig.4.14: Schematic of a CCDTL.

4.4.4.1. Electromagnetic design

The program CDTFISH in the Poisson SUPERFISH code distribution is used to design the cavity shape and compute surface fields and rf power losses. CDTfish sets up the geometry for coupled-cavity drift-tube linac (CCDTL) cavity as shown in Fig.4.15. It tunes the cavity by adjusting either the cavity diameter or the drift tube gaps. The CCDTL cavity is a figure of revolution about the beam axis.

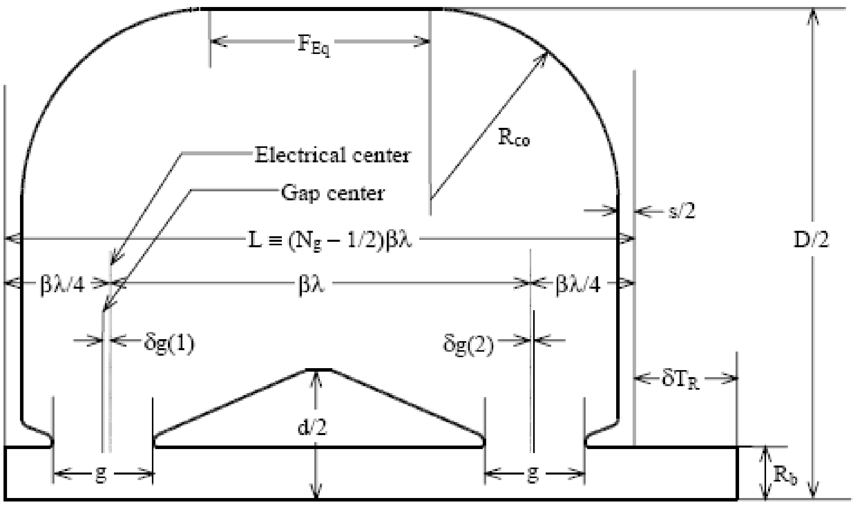

Fig.4.15: Full cavity of a one-drift-tube, 2-gap CCDTL

Studies were done to optimize the CCDTL cavity at 352.21 MHz and at the next harmonic frequency 704.42 MHz. The effective shunt impedance of the CCDTL cavity at 40 MeV was found to be higher at 352.21 MHz than at 704.42 MHz. However, the power dissipation is much lower for the CCDTL structure designed at 704.42 MHz than at 352.21 MHz as can be seen from Fig.16. Studies were also done to compare the 2 gap and 3 gap CCDTL structures. Again it was found that even though the effective shunt impedance is higher for the 3 gap structure the power dissipation is less for the 2 gap CCDTL structure. This can also be seen from Fig.4.16.

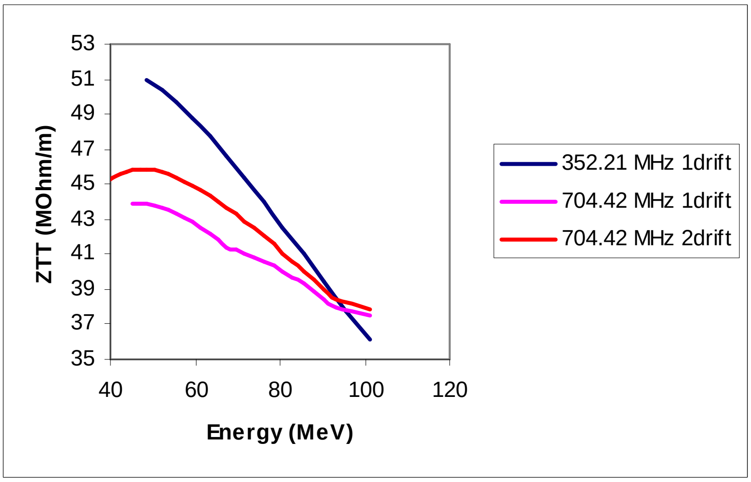

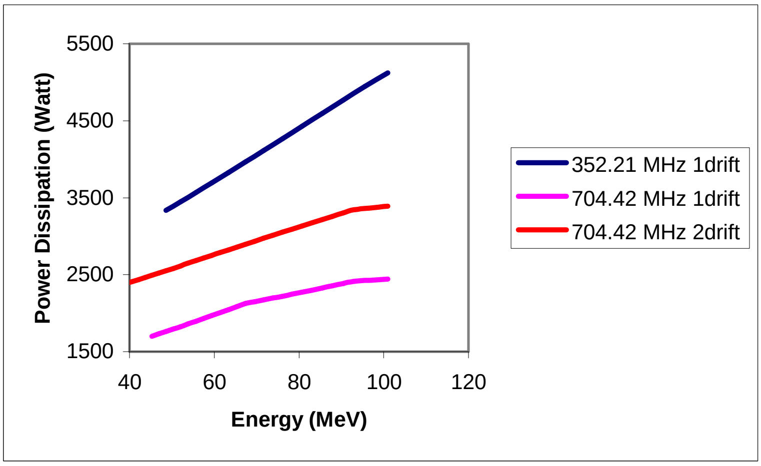

Fig.4.16: Variation of the effective shunt impedance and power dissipation in the CCDTL with energy for 352.21 MHz 1 drift CCDTL, 704.42 MHz 1 drift CCDTL, 704.42 MHz 2 drift CCDTL cavity.

At 40 MeV, it was found that the effective shunt impedance of the CCDTL starts becoming more than that of the DTL and the power dissipation in the two structures is comparable as can be seen from Fig.4.17. Hence at 40 MeV, we have switched to 2 gap CCDTL structure at 704.42 MHz.

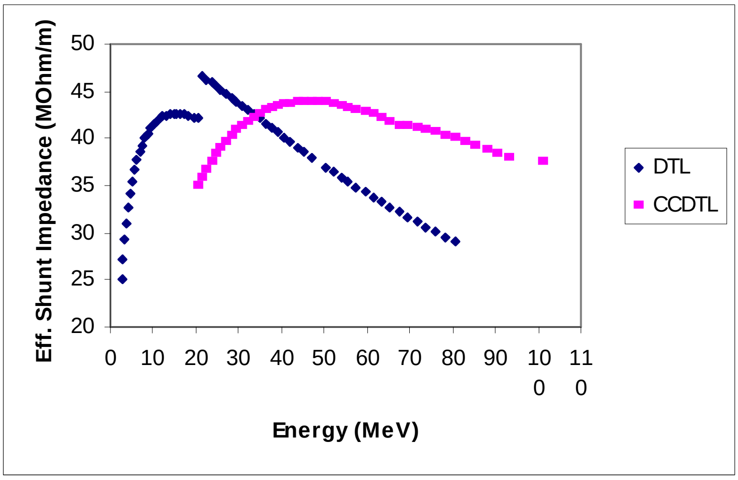

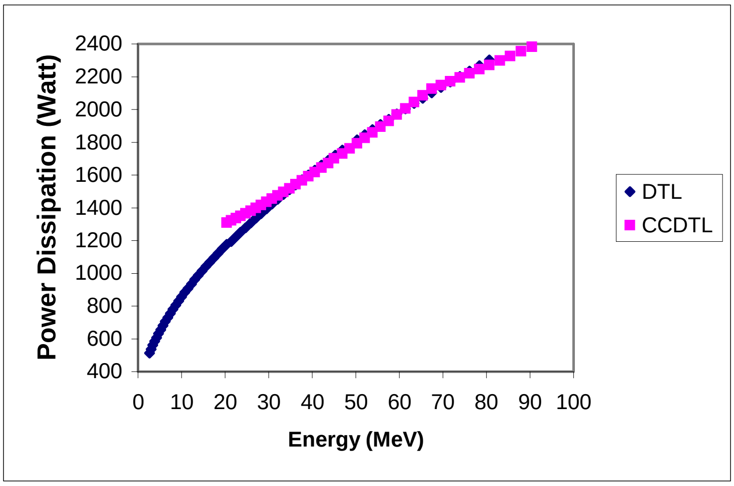

Fig.4.17: Variation of the effective shunt impedance and power dissipation in the CCDTL and DTL cavity with energy.

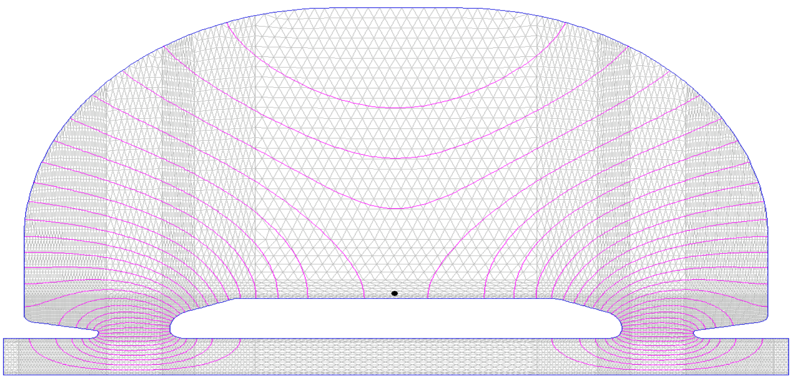

Fig.4.18: Electric field profile in the CCDTL.

The results of the cavity design are summarized in Table 4.4. The distance between 2 tanks is 3(βλ)/2, which is used for housing quadrupoles for focusing the beam. The electric field lines in the CCDTL cavity are shown in Fig.4.18.

Table 4.4. Parameters of the CCDTL cavity.

Parameter	**Value**
Frequency (MHz)	704.42
Diameter (cm)	24
No. of gaps	2
Drift tube diameter (cm)	5
Bore Radius (cm)	1.2
Equator flat (cm)	3
Cone angle (Deg)	10
Drift Tube Face angle (deg)	70
Inner Corner Radius (cm)	0.25
Outer Nose Radius (cm)	0.05
Inner Nose Radius (cm)	0.2
Drift Tube Corner Radius (cm)	0.5
Drift Tube Outer Nose Radius (cm)	0.6
Drift Tube Inner Nose Radius (cm)	0.3

4.4.4.2. Beam dynamics

The beam from the DTL is accelerated to ~ 100 MeV using CCDTL at 704.42 MHz. The beam from the DTL is matched to the CCDTL using the last two cells of the DTL and the first cavity of the CCDTL. The gradients in the last 2 quadrupoles in the DTL and the first 2 quadrupoles in the CCDTL are varied for transverse matching. This matching is done using TRACE3D. In the DTL the transverse lattice is of type FOFODODO with a 4 βλ period at 352.21 MHz. Starting in the CCDTL the transverse lattice changes to FODO with a 5 βλ period at 704.42 MHz. A focusing (or defocusing) quadrupole magnet follows every CCDTL cavity.

The phase advances per unit length are maintained constant from the DTL to the CCDTL for current independent matching. For this a quadrupole gradient of 39.8 T/m is taken in the CCDTL and the accelerating gradient is 3 MV/m. The parameters of the quadrupoles for matching the beam from the DTL to the CCDTL are shown in Table 4.5. and the beam trajectory and phase space plots are shown in Fig.4.19 .

Table 4.5. Parameters for matching between DTL and CCDTL.

Matching element	**Gradient (T/m)**
DTL Quad	-57.10
DTL Quad	82.62
CCDTL Quad	-72.80
CCDTL Quad	86.84

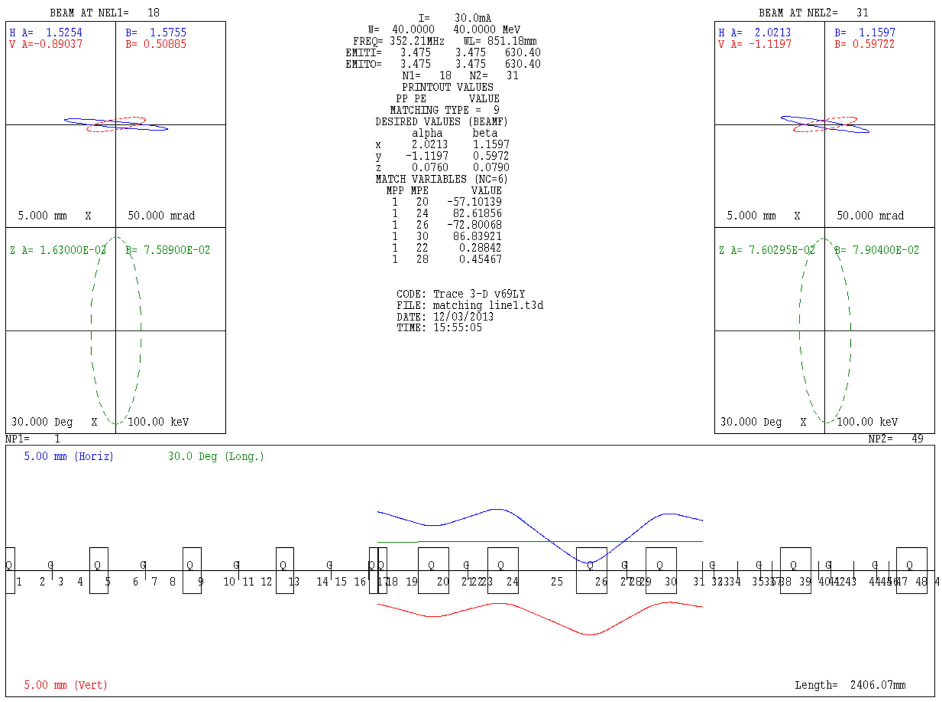

Fig. 4.19: Beam trajectory and phase space plots for matching section between DTL and CCDTL.

The evolution of the beam profile upto 100 MeV is shown in Fig.4.20 and the beam dynamics parameters are summarized in Table 4.6. Fig. 4.21. shows the beam profile in the transverse phase space, the transverse coordinate space and the longitudinal phase space at the end of the CCDTL.

Table 4.6. beam dynamics parameters of the CCDTL.

Parameter		**Value**
Energy Range (MeV)		40.12-100.25
Frequency (MHz)		704.42
Current (mA)		28.8
Focusing lattice		FODO
Lattice period		5βλ
Quadrupole gradient (T/m)		39.8-18.03
Eff. length of quad. (cm)		8.0
No. of quadrupoles		186
Synchronous phase (deg)		-30
Avg. acc. Gradient (MV/m)		1.04-2.5
Aperture radius (cm)		1.2
Total length (m)		69.5
Total RF Power (MW)		4.65
Norm. rms trans. Emitt. (π cm-mrad)	x	0.0231 - 0.0233
	y	0.0236 - 0.0242
Long. Emitt. (deg-MeV)		0.115 - 0.236

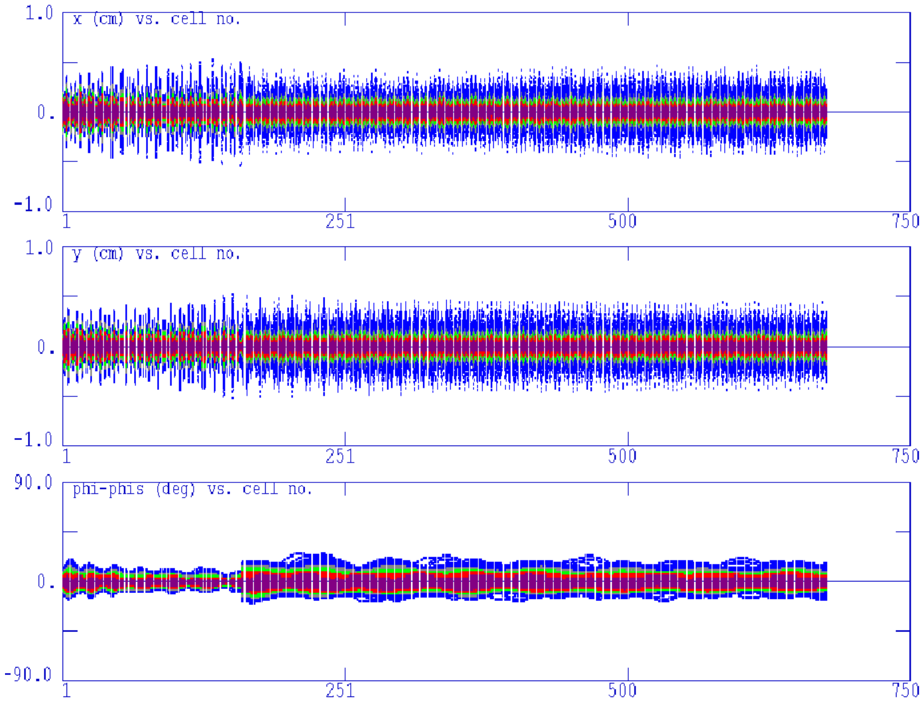

Fig.4.20: Beam Profile through DTL and CCDTL.

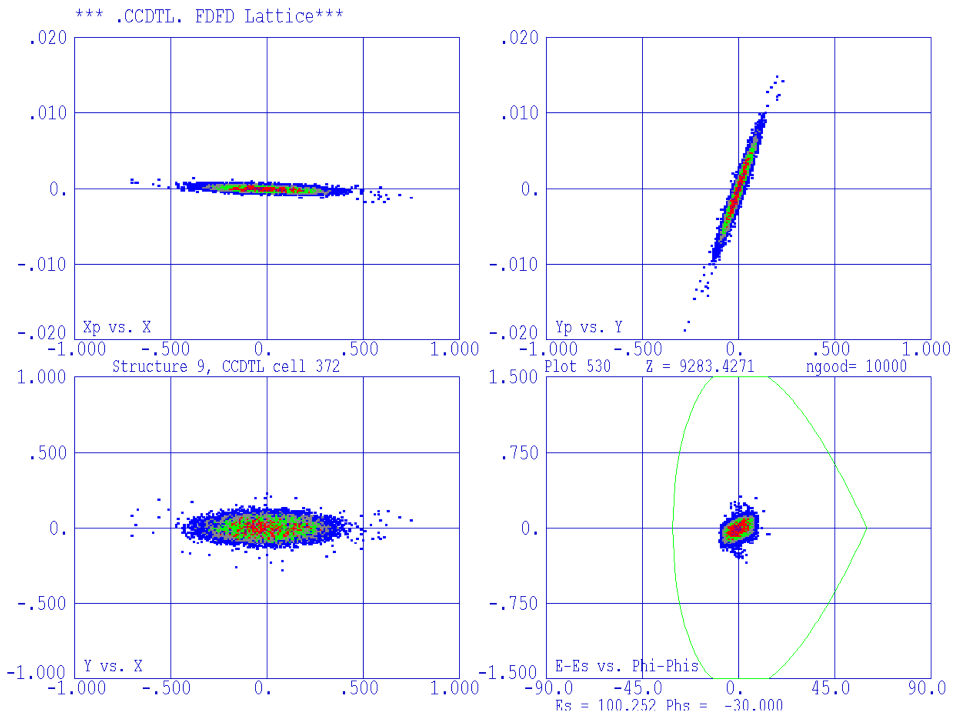

Fig. 4.21: Beam profile in (a). Transverse phase space in x (b) Transverse phase space in y (c). Transverse coordinate space xy and (d). Longitudinal phase space at 100 MeV.

4.4.5 Superconducting Linac

At higher energies (> 100 MeV for protons), most normal conducting structures are less efficient. At these energies, the space charge forces are not as high as in the lower energy range and the demand on focusing is reduced. Hence, superconducting multicell elliptical cavities are a preferred choice at these energies. Superconducting cavities offer various advantages over normal conducting cavities. The advantages of using superconducting cavities are [71]:

- In normal conducting linac a huge amount of power is deposited in the copper structure, in the form of heat, that needs to be removed by water cooling (in order not to melt the structures). The limited cooling capabilities in normal conducting cavities reduce the accelerating electric field gradient limit for high duty-cycle beams. Thus, superconducting structures offer the possibility to accelerate CW beams with high accelerating gradients
- The rf power dissipated in the cavities in a normal conducting cavity can be much higher than the power transferred into the beam for acceleration whereas in superconducting cavities, the power losses in the cavity are a negligible part of the total RF power. Hence the efficiency of superconducting cavities is very high.
- As shunt impedance is not an issue in superconducting cavities (it is already high due to negligible power dissipation), therefore these cavities are not optimized for high shunt impedance and hence the beam aperture can be larger offering larger aperture to beam radius ratio and hence there is lesser probability of beam loss.

However now we need to operate at cryogenic temperatures and the cavities must be housed inside cryostats where the temperature is maintained to 4 K or 2 K. Hence superconductivity, at the expenses of higher complexity, drastically reduces the dissipated power and the cavities transfer the RF power to the beam more efficiently. So, superconducting cavities are the best choice for the CW accelerator for ADS applications.

4.4.5.1. Electromagnetic Design

Superconducting elliptical cavities at 704.42 MHz are used to accelerate the beam from 100 MeV to 1 GeV. These cavities operate in the TM_{010} mode in the π mode. The superconducting cavities are designed to perform over a given velocity range and are identified by a design velocity called the geometric velocity or β_G. The design approach takes advantage of the large velocity acceptance of the superconducting cavities. For a cavity with N identical cells, the transit time factor T can be expressed as a product of two separate factors

$T = T_G T_S$.

The gap factor T_G, which is also the transit-time factor for a single gap of length g, RF wavelength λ, and particle-velocity β, is given by the expression

$T_G = \sin(\pi g/\beta\lambda)/(\pi g/\beta\lambda)$.

The synchronism factor T_S is a function of N and of the ratio of the local velocity, β to the cavity geometric velocity,

$$\beta_G = \frac{2L}{\lambda},$$

where L is the cell length.

The synchronism factor is given by:

$$Ts = \left\{ \begin{array}{ll} (-1)^{\frac{N-1}{2}} Cos(N\pi\beta_G / 2\beta) / NCos(\pi\beta_G / 2\beta), & \text{N odd} \\ (-1)^{\frac{N}{2}+1} Sin(N\pi\beta_G / 2\beta) / NCos(\pi\beta_G / 2\beta), & \text{N even} \end{array} \right\}$$

In order to choose the number of cells per cavity, a compromise must be made between many competing effects. SUPERFISH is used to compute the gap factor T_G and the synchronism factor T_S is computed from the above expression for varying no. of cells/cavity. The results are plotted in the Fig.4.22. As can be seen in the figure a small number of cells/cavity provides a large velocity acceptance. On the other hand, using a larger number of cells/cavity has the advantage of reducing the overall number of system components, system size, and system complexity. As a compromise between the two, in our design, we have chosen 5 cells/cavity.

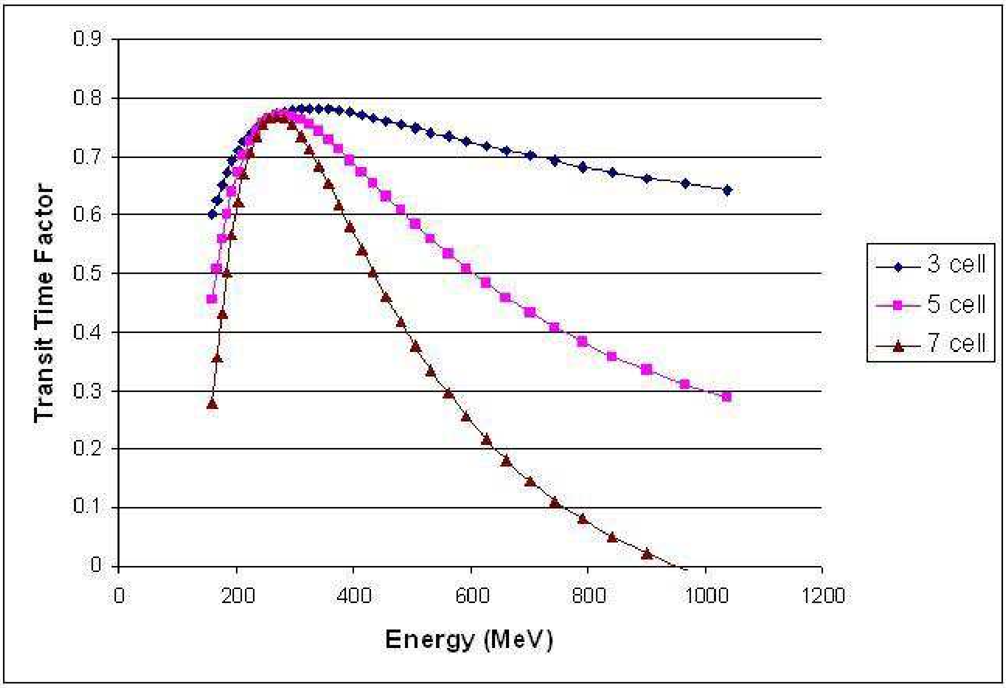

Fig 4.22: Variation of TTF with energy for different no. of cells/cavity.

Once the no. of cells/cavity has been chosen, the β_G values for the cavities, the number of constant β_G sections and the beam velocity limits for each section have to be determined. As can be seen from Fig.4.22., the transit-time factor decreases as the reference-particle velocity β deviates from β_G of the cavity. β_{min} and β_{max} for each section are determined by percentage decrease in transit time factor, that it is allowed to fall at the ends of each section from its maximum value for a given cavity of N cells. In our design, the transit time factor is not allowed to fall more than 75 % of its maximum value. The entire energy range from 100 MeV to 1 GeV is then divided into

3 sections, corresponding to β_G = 0.49, β_G = 0.62 and β_G = 0.8, each using different cavity geometry in that energy range as can be seen from Fig.4.23.

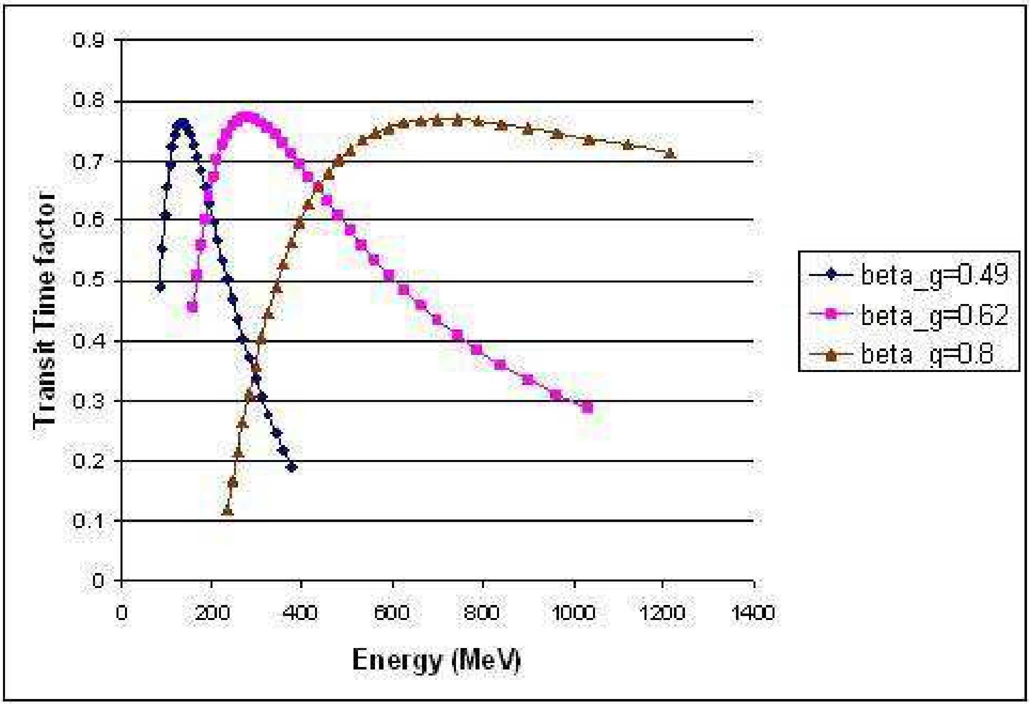

Fig.4.23: Variation of the TTF of the designed elliptic cavities with energy.

4.4.5.2 Cavity design

The program ELLFISH in the POISSON SUPERFISH code distribution is used to design the cavity shape. ELLFISH sets up the geometry for so-called elliptical cavities, which are often used in superconducting applications. These cavities feature an elliptical segment near the bore radius as shown in Fig.4.24. The elliptical cavity is a figure of revolution about the beam axis. ELLFISH tunes the cell by adjusting either the cavity diameter, outer radius of curvature, or the angle that the straight side of the cavity makes with the vertical.

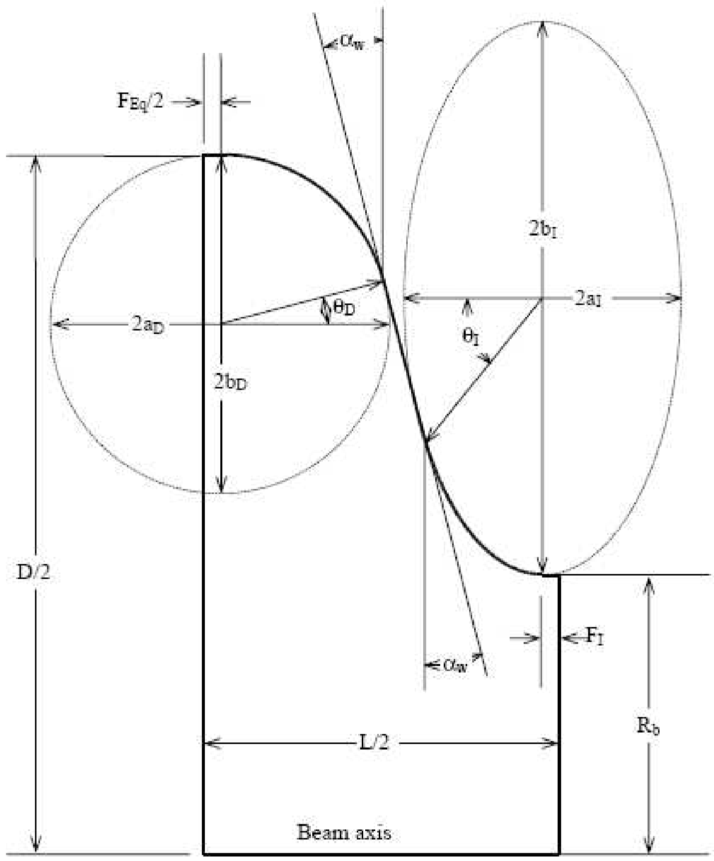

Fig.4.24: Geometry of the elliptic cavity.

An elliptical cavity design [72, 73] is a compromise between various geometric parameters. The main advantage of using superconducting cavity is a possibility of high accelerating electric field gradient E_0. How large an E_0 can be chosen depends on the maximum surface fields that can be maintained in the cavity. There are 2 characteristics, peak surface magnetic field B_P and the peak surface electric field E_P, which limit in principle an achievable value of E_0. The area of maximum magnetic field occurs at the equator and should not exceed H_c^{rf}, which is the critical magnetic field to prevent quenching of the superconducting cavities. The theoretical limit of H_c^{rf} for niobium is 190 mT. However in practice we try to limit B_P to 60 mT. E_P occurs near the Iris of the cavity and also has certain limit given by the field emission threshold. The regions of peak magnetic and electric fields in an elliptical cavity are shown in Fig. 4.25.

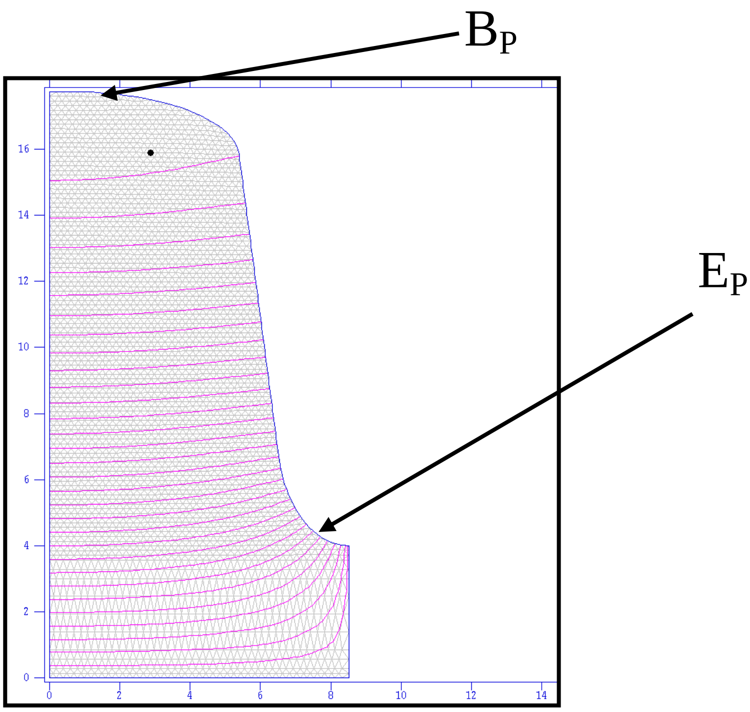

Fig. 4.25: Regions of peak surface magnetic field and electric field in an elliptical cavity.

To maximize the accelerating field it is important to minimize E_P/E_0 and B_P/E_0. The criterions for the elliptical superconducting cavity design are:

$$\frac{E_P}{E_0} < 2.5$$

$$\frac{B_P}{E_0} < 4.5\,\mathrm{mT/(MV/m)}$$

$$B_P < 60\,\mathrm{mT}$$

$$E_P < 27.5\,\mathrm{MV/m}$$

With these design criterions the various parameters of the elliptical cavity cell that need to be optimized are

1. **Dome B**, the vertical semi-axis of dome ellipse (which allows to reduce the capacitive volume in favor of the magnetic volume and viceversa, in order to balance the peak surface magnetic and electric fields on the cavity walls),
2. **Dome A/B**, the dome ellipse aspect ratio (vertical axis divided by the horizontal axis, allows to find a local minimum for the peak surface magnetic field),
3. Wall angle α_w (which influences the mechanical behavior of the cavity and controls its inductive volume)
4. **Iris A/B**, the iris ellipse aspect ratio (which allows to find a local minimum for the peak surface electric field).
5. Equator Flat $\mathbf{F_{eq}}$
6. $\mathbf{R_b}$, the bore radius.

A last geometrical parameter, **D**, the distance between the equator and iris ellipse centers, is used as the free variable for tuning the cavity to the desired frequency, leaving all the other parameters unaltered.

The design criteria are met by limiting the spatial average of the axial accelerating field Eo to 11 MV/m in the first set of superconducting cavities designed for β_G = 0.49 and to 15 MV/m in the second and third set of superconducting cavities designed for β_G = 0.62 and 0.8. The parameters of the designed cavity are summarized in Table.4.7. and Fig.4.26. shows the electric field profile in the 5 cell elliptic cavity for β_G = 0.49.

Table 4.7. Parameters of the SC cavity.

Parameter	**βg = 0.49**	**βg = 0.62**	**βg = 0.8**
Dome B (cm)	2.4	1.7	2
Dome A/B	0.85	2.0	2.4
Wall Angle (deg)	6	7	7
Equator Flat (cm)	1.5	1.2	1.2
Iris A/B	0.8	0.6	0.6
Diameter (cm)	36.707	35.938	35.485
E_P (MV/m)	33.99	26.95	22.04
B_P (mT)	68.10	54.56	47.98
E_P/E_0	2.27	1.80	1.47
B_P/E_0 (mT/(MV/m))	4.54	3.64	3.20
R_sQ (Ω)	137.828	179.429	214.755
Q	0.92×10^{10}	1.20×10^{10}	1.44×10^{10}

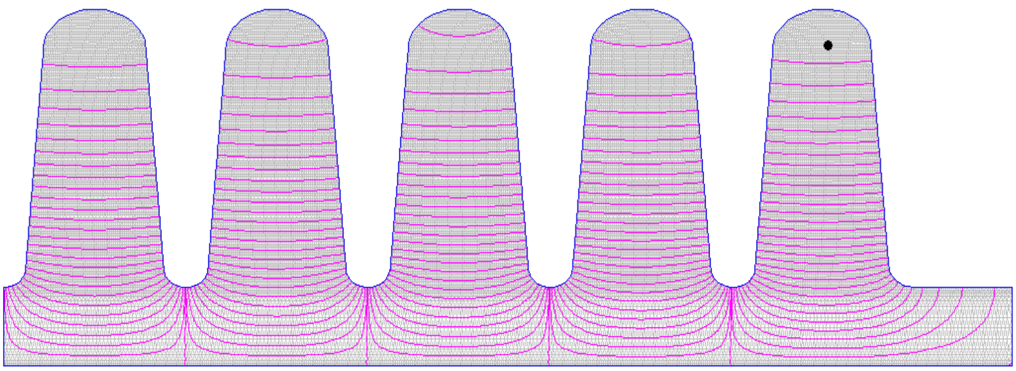

Fig.4.26: Electric field profile in the 5 cell elliptic cavity for $\beta_G = 0.49$.

4.4.5.3 Beam Dynamics design

The beam dynamics was done using PARMILA code. The transverse focusing is achieved by using room temperature electromagnetic quadrupole doublets in between the cryomodules containing the superconducting cavities. The focussing doublets are placed after every 2 cavities in the first section, which will have 16 cryostats, after every 3 cavities in the second section having 15 cryostats and after every 4 cavities in the second section having 17 cryostats. To obtain a current independent match between the normal conducting linac and superconducting linac, which has a weaker focusing; the quadrupole gradients in the CCDTL are gradually reduced with energy. Transverse matching is done using the last 2 quadrupoles in the CCDTL and the first 2 qaudrupoles in the superconducting linac. Transverse matching between two superconducting sections was done by making small adjustments to the quadrupole gradients at the transition between the sections. Longitudinal matching was achieved by adjusting the synchronous phase ϕ_s in the superconducting cavities to maintain constant longitudinal phase advance per unit length on both sections and maintaining a constant energy gain in each cavity. This was done by keeping ($\Delta W\tan\phi_s/L$) constant on both sides of the transition, where ΔW is the energy gain per cryomodule and L is the length of the focusing period. The beam dynamics parameters of the SC linac are shown in Table 4.8. The beam profile through the linac is shown in Fig. 4.27 and the beam profile in the transverse phase spaces, the transverse coordinate space and the longitudinal phase space is shown in Fig. 4.28. The variation of emittance with beam energy is plotted in Fig. 4.29 and Fig. 4.30 shows the variation of beam size with energy. The layout of the cryomodules for the three beta sections is shown in Fig. 4.31. It can be seen that the aperture is 10-12 times the rms beam size in the normal conducting linac, while in the superconducting linac where the risk due to activation is more; it is more than 16 times the rms beam size.

Table 4.8. Parameters of the superconducting linac

Parameter		**β_G = 0.49**	**β_G = 0.62**	**β_G = 0.8**
Energy Range (MeV)		100.25-191.62	191.62-434.88	434.88-1014.26
Frequency (MHz)		704.42	704.42	704.42
Current (mA)		28.8	28.8	28.8
Trans. focusing lattice		Doublet	Doublet	Doublet
Lattice period (cm)		308.13	607.9	793.41
Quad. gradient (T/m)		5.8-4.31	4.5	4.4
Eff. length of quad. (cm)		35	40	45
Synchronous phase		-30	-26.84	-26.48
Maxm. Acc. Grad. (MV/m)		11	15	15
Cavities/cryomodule		2	3	4
No. of cryomodules		16	15	17
Aperture radius (cm)		4.0	4.0	4.0
RF Power (MW)		2.63	7.01	16.69
Total length (m)		49.3	91.19	134.88
Norm. rms trans. Emitt. (π cm-mrad)	x	0.0233 -0.0255	0.0255-0.026	0.026-0.031
	y	0.0242 -0.0245	0.0245-0.026	0.026-0.026
Long. Emitt. (deg-MeV)		0.236 -0.248	0.248 -0.271	0.271-0.279

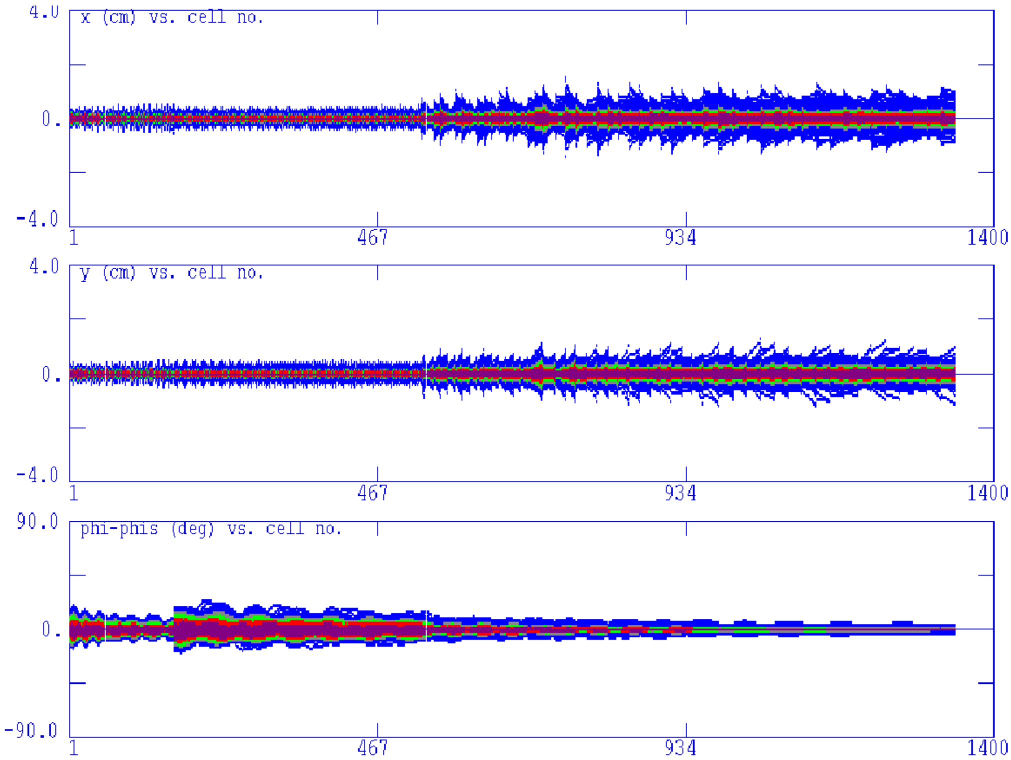

Fig.4.27: Beam profile through the linac.

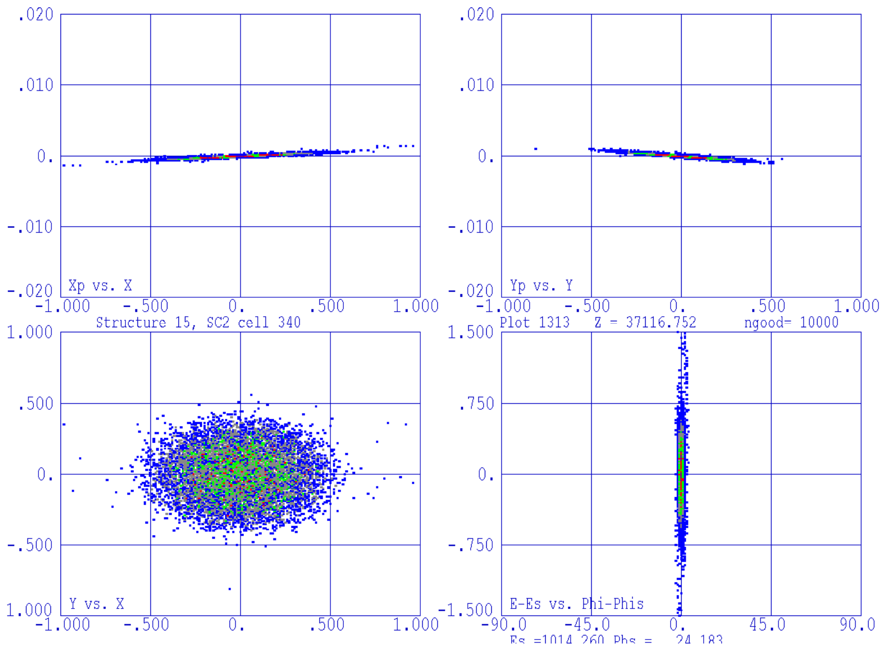

Fig. 4.28: Beam profile in (a). Transverse phase space in x (b) Transverse phase space in y (c). Transverse coordinate space xy and (d). Longitudinal phase space at 1 GeV.

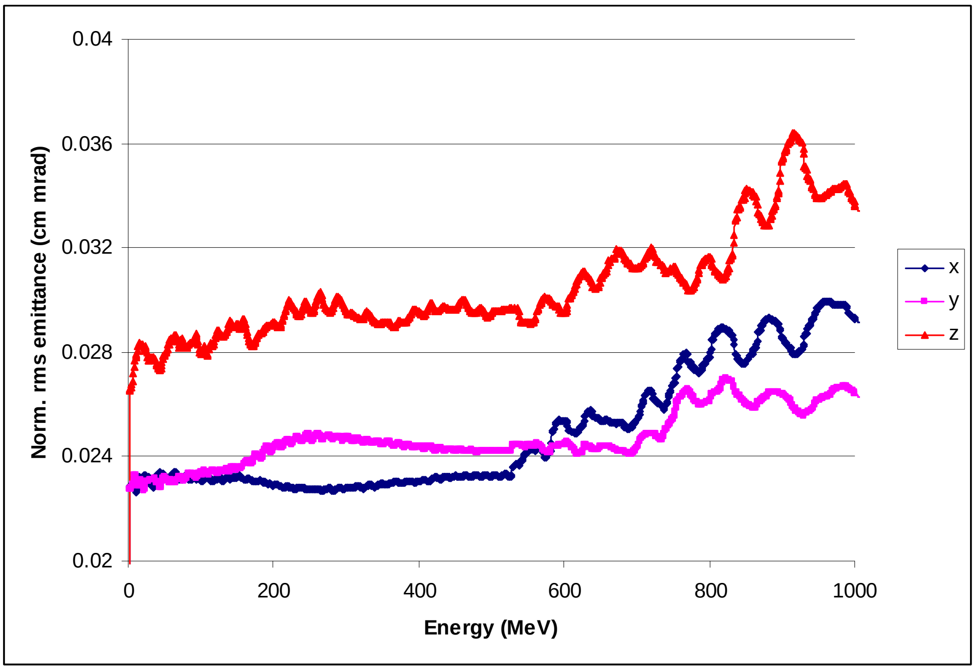

Fig. 4.29: Variation of emittance with energy in the linac.

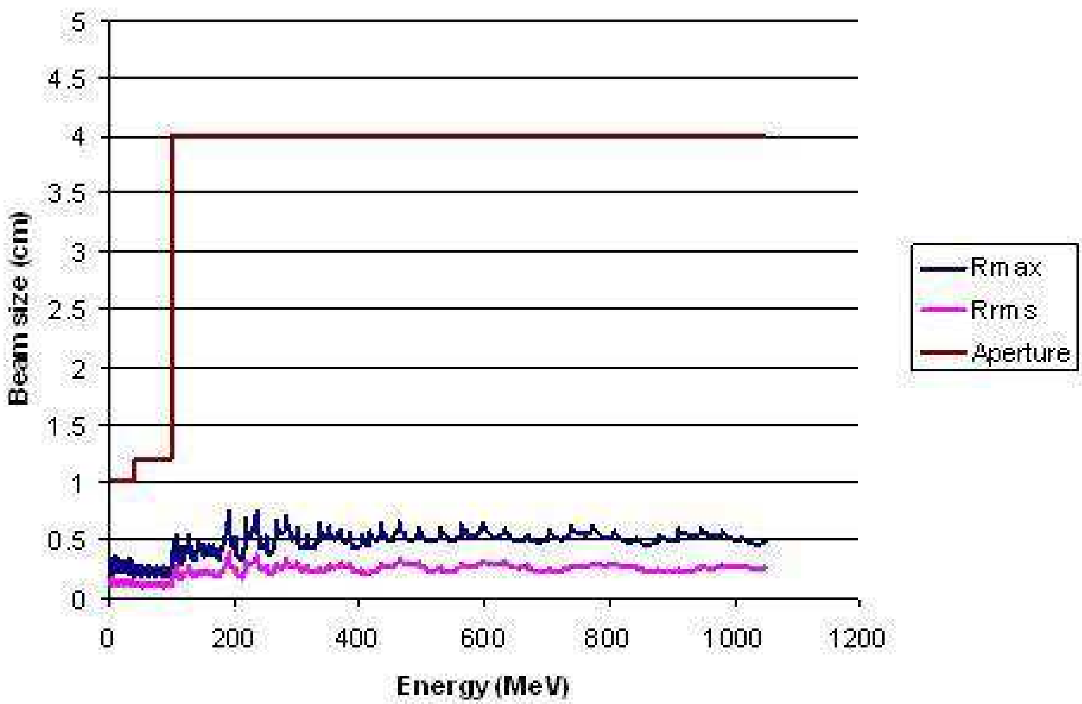

Fig.4.30: Variation of beam size with energy in the linac.

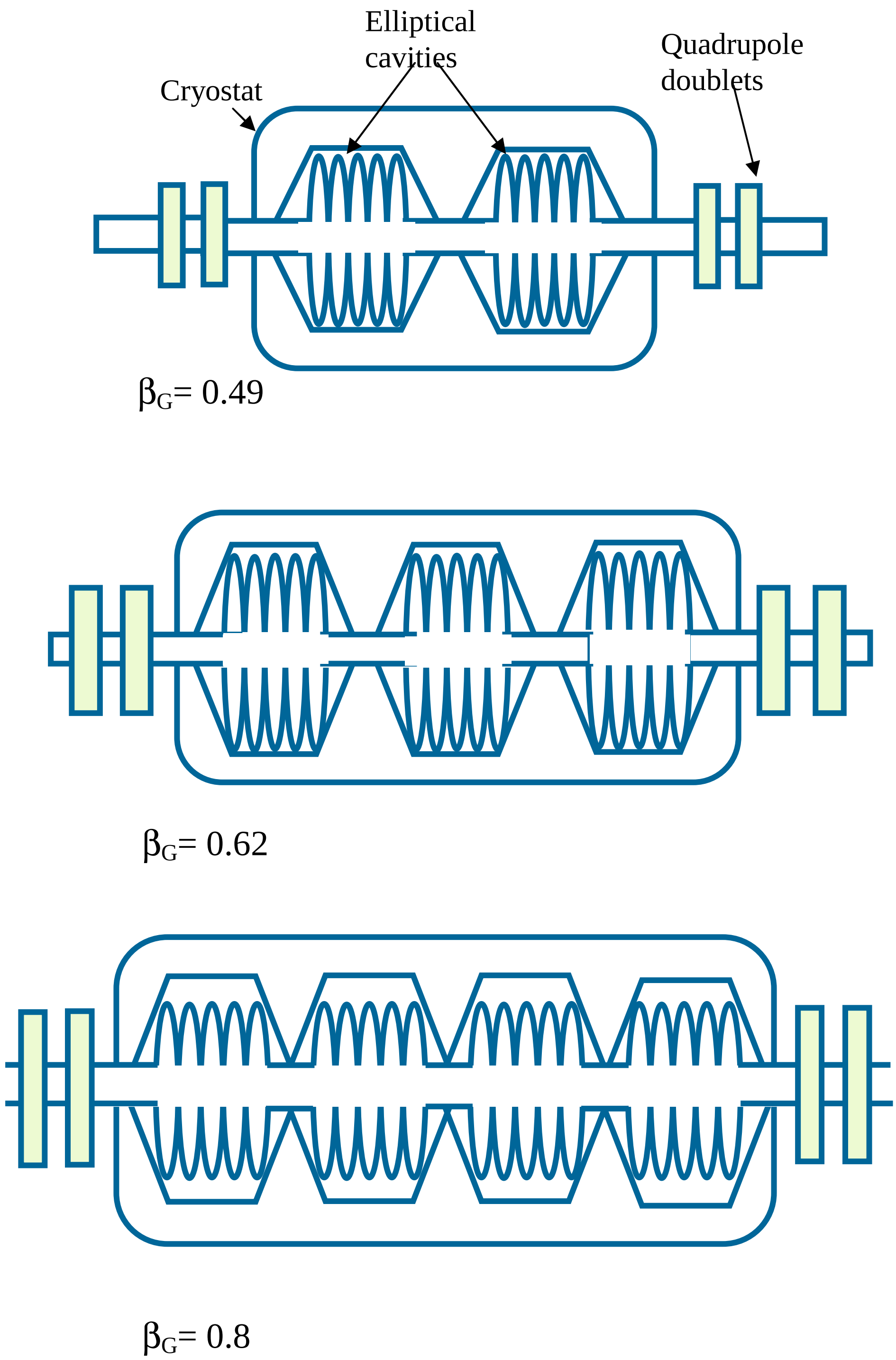

Fig.4.31: Layout of cryomodules for different beta sections.

4.5 Summary and conclusions

A 1 GeV, 30 mA linac has been designed for the Indian ADS programme and its beam dynamics studies have been done. The linac is normal conducting upto 100 MeV and superconducting from 100 MeV to 1 GeV. It consists of an ECR ion source, a RFQ which will accelerate the beam to 3 MeV, DTL upto 40 MeV followed by CCDTL to accelerate the beam to 100 MeV. The proton beam is then accelerated to 1 GeV using superconducting 5 cell elliptical cavities. The total RF power required in the linac is about 33.5 MW. The total length of the designed accelerator is about 350 m and the overall transmission is about 96%. The 4% loss takes place in RFQ during bunching of the beam which is not expected to pose any radiation problem. In the high energy section superconducting cavities are used where the aperture to rms beam size ratio is high to minimize the risk of activation due to any beam loss.

CHAPTER 5

Design of Superconducting Structures at Medium and High Energy

5.1 Introduction

One of the main sub-systems of ADS is a high energy (~1 GeV) and high current (~30 mA) CW proton linac. In the past, a possible configuration for the 1 GeV linac has been worked out using normal conducting structures in the medium energy section and detailed beam dynamics studies have been done [25]. This has been described in chapter 4 of this thesis. However, in recent times, in view of advances in the superconducting technology and new structures like the spoke resonators being developed for use in the medium energy range, the DTL and CCDTL structures used in this energy range are being replaced by these superconducting structures. The accelerating gradients that have been achieved with these SC structures today are up to 18 MV/m [74] as compared to the accelerating gradients of 2-3 MV/m with NC structures at these energies. With these gradients, overall shorter length of the linac will be possible. Also, for CW structures, lot of RF power is dissipated on the structures and removing this dissipated heat is a major challenge in normal conducting structures. This also leads to wastage of lot of RF power which is very expensive. Use of superconducting technology will make the linac compact and cost effective. With SC cavities, larger apertures can be used; hence probability of beam loss also reduces. So for high current linacs operating in CW mode, superconducting option seems to be the best. With these advantages, various projects are now considering superconducting cavities in the medium energy range. For the

Indian ADS programme also, it has now been planned to go for superconducting structures right after the RFQ. The proposed layout of the linac is shown in Fig. 5.1.

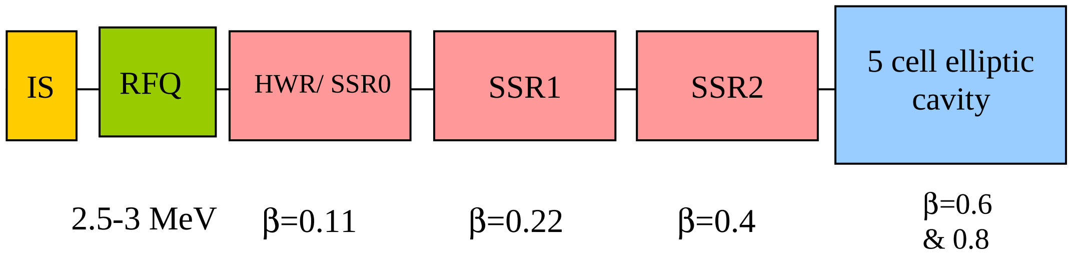

Fig. 5.1: Proposed layout of the 1 GeV linac for ADS.

The medium energy section will consist of three different types of structures. Immediately after the RFQ, to accelerate the beam to around 10 MeV, two types of TEM structures are being considered as options for acceleration of the beam: the HWR at 162.5 MHz and the Single Spoke Resonator (SSR) at 325 MHz. Both options are being investigated in order to leave open the possibility of going to a lower frequency in order to have a larger bore to mitigate beam halos. However, this decision can be taken only after detailed beam dynamics investigations. The beam from 10 MeV will be accelerated by two families of single spoke resonators, the SSR1 at $\beta_G = 0.22$ to accelerate the beam to about 35 MeV and SSR2 at $\beta_G = 0.4$ to about 150 MeV, both operating at 325 MHz. This beam is then accelerated to1 GeV using multicell elliptical cavities [75].

5.2 Low and medium energy superconducting cavities

At low energies, the velocity of the particles is changing continuously as it gains energy in the linac. In order to maintain synchronism between the RF field and the beam particles for energy gain, the cell length has to keep increasing with the velocity of the particles. Normal conducting cavities like DTL, CCDTL, SDTL etc are designed with increasing cell lengths to maintain this synchronism. Another possible configuration is that the distance between cavities is fixed, and the phase of each cavity is individually adjusted to take into account the increase in beam velocity. In this case, each cavity has to be driven by an individual RF amplifier and phase and amplitudes of each cavity can be set independently. This scheme has the advantage of flexible linac operation, but has the drawback of a high cost. Having individual RF amplifiers or multiple splitting schemes from a single amplifier can be expensive, as can completely separated single-gap cavities. For superconducting structures, shunt impedance and power dissipation are not a concern, and the much lower RF power required allows using simpler and relatively inexpensive amplifiers. This type of configuration is therefore preferred for most superconducting linac applications at low energy, up to some 100–150 MeV, where more operational flexibility is required and where the short cavity lengths allow having more focusing per unit length, as is required at low energy. The transit time factor of a cavity with few cells has a broad velocity acceptance, and if each cavity is excited by its own RF generator, each cavity phase can be adjusted independently to maximize the acceleration of the injected beams.

The superconducting cavities used at low and medium energies are generally TEM coaxial type structures, such as quarter wave and half wave resonators loaded at the end by a drift tube. Typically, a single inner conductor loaded by a drift tube at the end is contained within the cylindrical cavity and it gives two accelerating gaps with opposite polarity. The spacing between the gap centres is maintained as $\beta_s\lambda/2$, where β_s is the velocity of the synchronous particle that travels between the two gap centres in half a RF period, and λ is the RF wavelength. The loading element is either quarter wavelength or half wavelength long and the maximum electric field occurs at $\lambda/4$ in both the cases. The first type of structure is called the quarter wave resonator and is shown in Fig. 5.2. (a). The second type of structure is called the half wave resonator and is shown in Fig. 5.2. (b).

 

Fig.5.2: (a).Quarter wave resonator and (b). Half wave resonator.

Another superconducting resonator that has been recently proposed for several proton beam applications requiring operation in CW mode or at a large duty cycle is the spoke resonator. The main advantages of spoke resonator over other structures are the compact dimensions and the relative insensitivity to mechanical vibrations. While in the half wave resonator the inner spoke conductor is along the axis of the cavity, in the spoke resonator, it is perpendicular to it. A single spoke resonator is a 2-gap resonator. However it is more economical to have structures with more number of gaps. This can be done by having more than one spoke in the same resonator. These are known as multi spoke resonators. The adjacent spokes in a multi spoke resonator are oriented perpendicular to each other [76]. Single, double and triple spoke resonators are shown in Fig. 5.3.

Fig. 5.3: Single, double and triple spoke resonators.

Quarter wave resonators are favorable for operation at low energy and low frequency typically < ~ 160 MHz. Higher frequencies present an unfavorable aspect ratio that introduces intolerable beam steering. In the frequency range 160-350 MHz, the coaxial HWR are very well suited. Their high symmetry and short physical length make them steering-free and mechanically stable. The HWR however has lower shunt impedance as compared to the QWR and the spoke resonators. For the same velocity and frequency range, the single spoke structure (SSR) is a competitive candidate. The main difference between Coaxial and Spoke HWR is the symmetry axis of the outer conductor. This is parallel to the beam axis in the Spoke, leading to a larger cavity volume leading to higher shunt impedance. In a small machine, intended to operate at 4 K, this difference in shunt impedance has a big impact on the power dissipation and thus the cooling requirements.

5.3 Cavity design studies

5.3.1 Design criterion

The design of a low and medium-β superconducting structure is a tradeoff between several factors. A lower value of operating frequency has to be chosen inorder to keep the cell lengths reasonable at low energy. The choice of a low frequency increases the voltage gain per cell, the beam energy acceptance, and beam quality, while decreasing rf losses and beam losses. But a low rf frequency increases structure size and microphonics [77] level, making rf control more challenging [78]. Having a larger number of cells per cavity can give higher voltage gain per structure, but the velocity acceptance is narrower. Several structure geometries are therefore needed, each of which is optimized for a particular velocity range. Also, lower the velocity of the charged particle under acceleration, the faster it will change, and the narrower the velocity range of a particular accelerating structure. This implies that the smaller the β of a cavity, the smaller the number of cavities of that β which can be used in the accelerator. Also, failure of a low-β cavity to achieve its design gradient means that the particle will not be captured by the following accelerating section. As a consequence of their small number, and importance of achieving their design gradient, medium-β cavities need to be designed and operated more conservatively than high-β cavities. As β increases structures can be designed more aggressively with the expectation of achieving the design gradient on average.

The design of superconducting cavities involves optimization of several parameters. The main parameters are frequency, operating temperature, energy gain, transit time factor, peak magnetic and electric fields, geometric beta, stored energy, accelerating gradient, geometry factor and multipacting. Some parameters are discussed below.

Frequency and operating temperature

The surface resistance that determines the RF losses in the cavity depends on the operating frequency. The surface resistance for a niobium cavity is given by [79]

$$R_s(\Omega) = 9x10^{-5}\frac{f^2(GHz)}{T(K)}e^{-\alpha T_c/T} + R_{res} \qquad (5.1)$$

Where, α = 1.92, T_c = Critical temperature which is 9.2 K for Nb, R_{res} = Residual resistance which is determined by imperfections in the surface. Typical values of residual resistance are of the order of 10-20 nΩ, but in several experiments values as low as 1-2 nΩ have been reached. The first term in equation 5.1 is the BCS resistance. Variation of BCS resistance with temperature for Niobium at different frequencies is plotted in Fig. 5.4. It can be seen that, at lower frequencies, cavities can be operated at higher temperatures. Thus for structures like HWR and spoke resonators that operate in the frequency range 150 MHz to 350 MHz, can be operated at 4 K is possible which simplifies the cryogenic design while for multicell elliptical cavities that operate at higher frequencies, the operating temperature is 2 K.

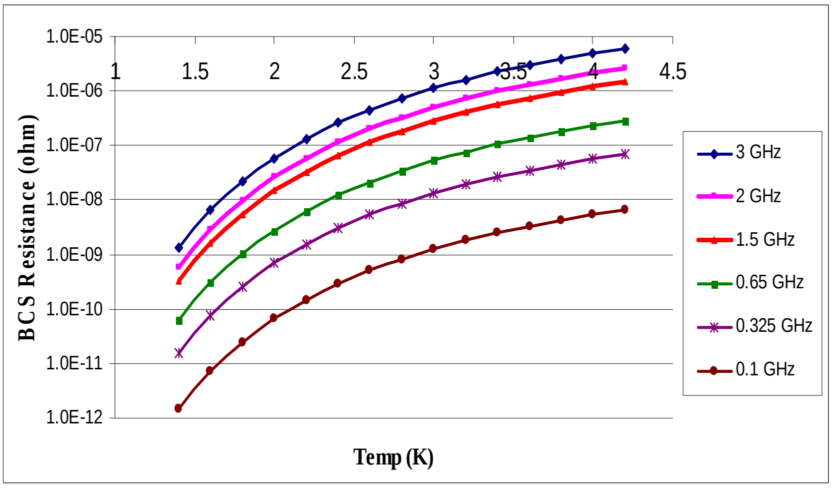

Fig. 5.4: Variation of BCS resistance of Nb with temperature for different frequencies.

Transit time factor and geometric beta

Unlike normal conducting structures that are varying beta structures, the superconducting cavities are designed to perform over a given velocity range. Each cavity is identified by a design velocity called the geometric velocity or β_G and is used to accelerate particles over a range of beta values near β_G. This is because superconducting cavities have a large velocity acceptance. The velocity acceptance is defined in terms of the transit time factor T [79]. The particles with velocity equal to β_G have the maximum value of T. Particles with velocity less than or greater than β_G have smaller values of T. The velocity acceptance is defined as the velocity range $\Delta\beta$ around β_G for which the transit time factor falls to N times the maximum value of T, where N can range from 0.6 to 0.7. Thus different structures corresponding to a value of β_G are needed for acceleration of particles in different energy ranges. The velocity acceptance of cavities is smaller at lower velocities. Also, as the number of cells per cavity increases, the velocity acceptance of the cavity decreases.

:

Peak surface fields

Another parameter to be optimized is the peak surface electric and magnetic fields. A high value of peak surface electric field causes breakdown due to field emission while a high value of peak surface magnetic field can cause breakdown of superconductivity if Hp > H_c^{rf}, where H_c^{rf} is the critical value of rf field at which quenching occurs. The ratio of the peak fields to the accelerating field, E_p/E_0 and B_p/E_0 have to be minimized. The criterions for cavity design are:

For high beta cavities,

$$\frac{E_P}{E_0} < 2.5 \qquad \frac{B_P}{E_0} < 4.5\,\mathrm{mT/(MV/m)}$$

For low beta cavities,

$$\frac{E_P}{E_0} < 4 - 6 \qquad \frac{B_P}{E_0} < 6 - 20\,\mathrm{mT/(MV/m)}$$

With these design criterion, the designs of a 162.5 MHz HWR for $\beta_G = 0.11$, a 325 MHz SSR0 for $\beta_G = 0.11$ and 650 MHz elliptic cavities (both $\beta_G = 0.6$ and $\beta_G = 0.8$) were done.

5.3.2 Half wave resonator at 162.5 MHz

The HWR [80] was designed in CST MWS and optimized to resonate at 162.5 MHz while keeping the peak surface electric and magnetic fields within the limits. Fig. 5.5 shows the electric field lines in the HWR designed in CST MWS and the some of the parameters and results are summarized in Table 5.1.

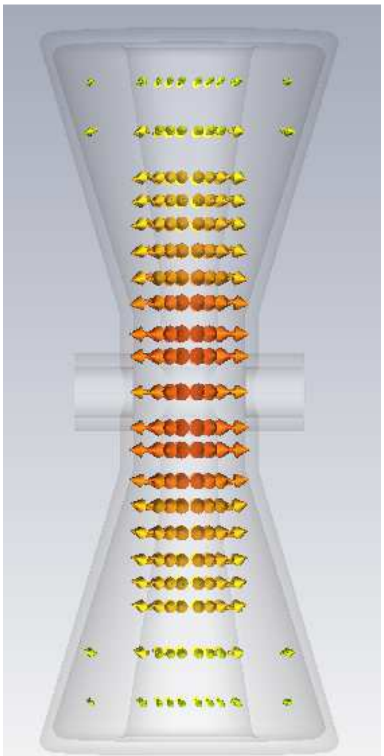

Fig. 5.5: Electric field lines in the HWR designed in CST MWS.

The peak surface magnetic field occurs at the outer conductor's surface encircling the spoke while the peak surface electric field appears near the aperture.

Table. 5.1. Design parameters of HWR.

Parameters	**Value**
Beta	0.11
Frequency (MHz)	162.5
E_{pk}/E_0	5.15
B_{pk}/E_0 (mT/(MV/m))	6.44
Height (H) (mm)	860
Spoke radius (mm)	80
Aperture radius (mm)	33

5.3.3 Single-Spoke Cavities at 325 MHz

A single-spoke resonator [81] SSR0 (β_G = 0.11) has been designed as an alternative to the HWR to accelerate the beam after the RFQ. The SSR was designed in CST MWS and optimized to resonate at 325 MHz while keeping the peak surface electric and magnetic fields within the limits. Fig. 5.6 shows the electric field lines in the SSR designed in CST MWS and the some of the parameters and results are summarized in Table 5.2.

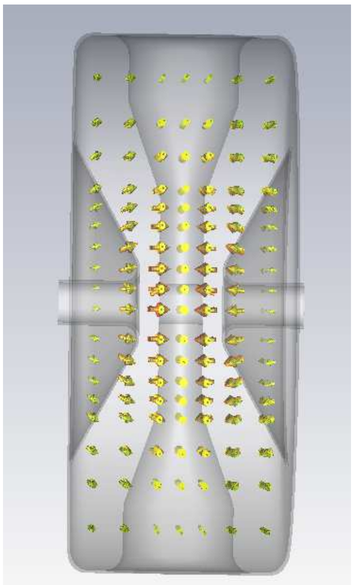

Fig. 5.6: Electric field lines in the SSR0 designed in CST MWS.

Table 5.2. Design parameters of SSR0.

Parameters	**Value**
Beta	0.11
Frequency (MHz)	325
E_{pk}/E_0	5.78
B_{pk}/E_0	6.53
Height (H) (mm)	399.4
Spoke radius (mm)	45
Aperture radius (mm)	15

For theSSR0, the peak surface magnetic field occurs on the spoke while the peak surface electric field appears near the aperture.

The SSR0 will accelerate the beam from the RFQ to around 10 MeV. It is planned to further accelerate the beam to around 150 MeV by using 2 different families of single-spoke resonators – SSR1 and SSR2. The design optimization of these cavities is in progress.

5.3.4 Elliptic Cavities at 650 MHz

Multi-cell elliptic cavities [72] operating in the TM_{010} mode will be used to accelerate the beam at higher energies (~150 MeV – 1 GeV). Elliptical cavities corresponding to $\beta_G = 0.6$ and $\beta_G = 0.8$ were designed using SUPERFISH. The design criterion was to minimize the peak surface electric and magnetic fields and keep the ratios $E_{pk}/E_0<2.5$ and $B_{pk}/E_0<4.5$ mT/(MV/m). The main design parameters are shown in Table 5.3 and the electric field lines in the elliptical cavities as designed in SUPERFISH is shown in Fig. 5.7.

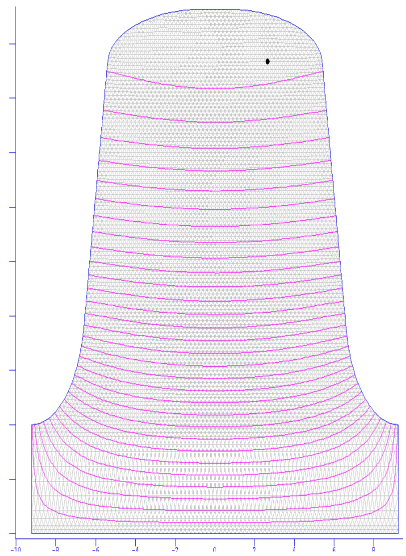

Fig. 5.7: Electric field lines in the elliptical cavity designed in SUPERFISH.

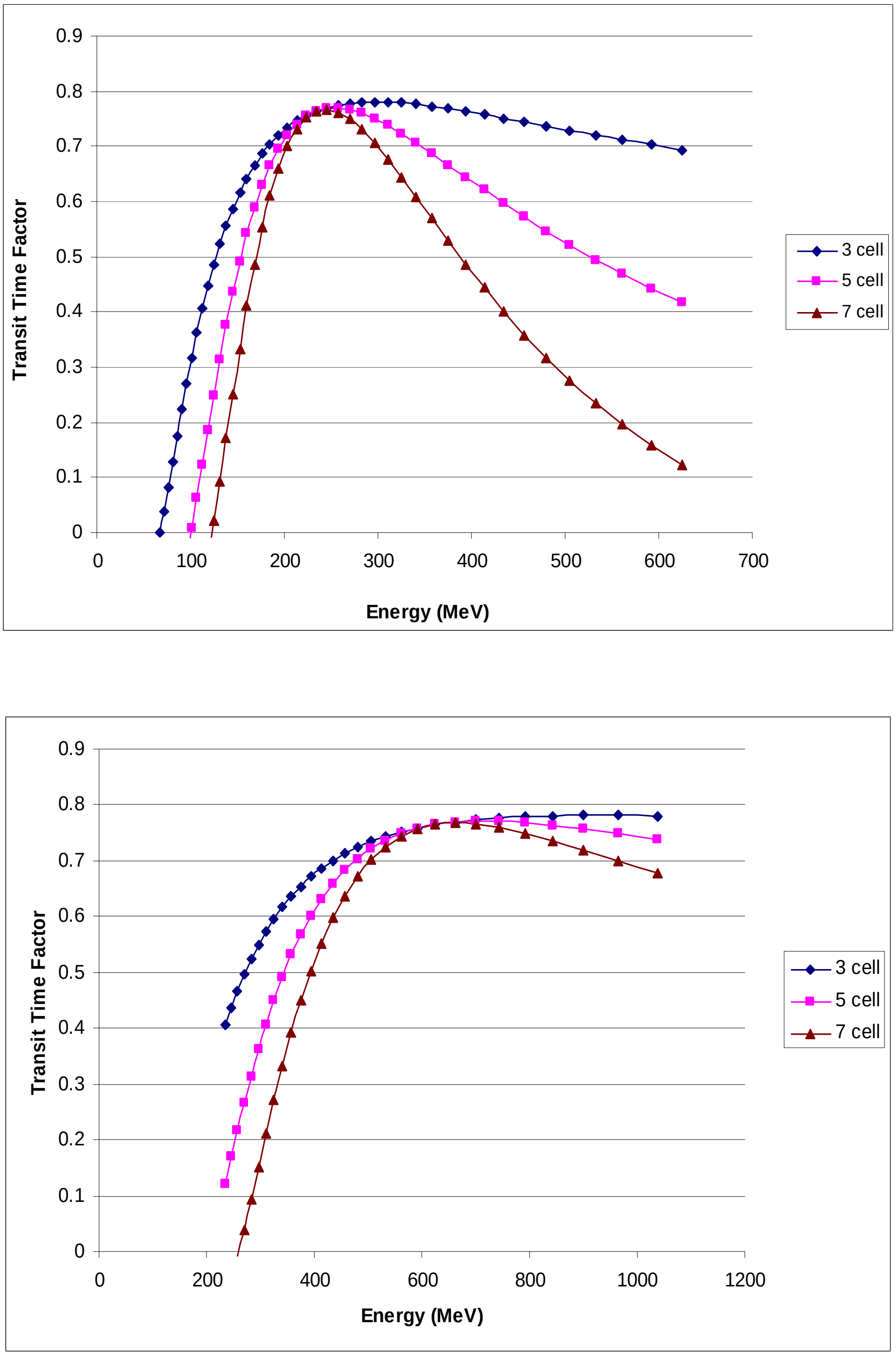

Fig. 5.8: Variation of TTF with energy for different no. of cells/cavity for (a) $\beta_G = 0.6$, and (b) $\beta_G = 0.8$.

Table 5.3. Parameters of the elliptical cavities for β_G = 0.6 and β_G = 0.8.

Parameters	**β_G = 0.6**	**β_G = 0.8**
No. of Cells	5	5
Frequency (MHz)	650	650
Diameter (cm)	39.34	38.54
Dome B (cm)	2	2
Dome A/B (cm)	1.9	2.4
Wall Angle (deg)	8	7
Iris a/b (cm)	0.8	0.6
Bore Radius (cm)	4.0	4.0
Equator Flat (cm)	0.5	1.2
Acc.gradient (MV/m)	15	15
E_{pk}/E_0	1.89	1.45
B_{pk}/E_0	3.57	3.29
R_sQ	175.2	205.03

Figs. 5.8. (a) and (b) show the transit time factor curves for the two types of cavities for 3, 5 and 7 cells per cavity. It can be seen that the velocity acceptance is higher for lower number of cells per cavity. On the other hand, using a larger number of cells per cavity has the advantage of reducing the overall number of system components, system size, and system complexity. So a careful compromise has to be made between the two.

For the elliptical cavity, the peak surface magnetic field occurs on the surface of the dome ellipse while the peak surface electric field appears on the surface of the equator ellipse near the aperture. Preliminary 3D simulations of the single cell elliptical cavity for β_G = 0.6 have been also done. Fig. 5.9 shows the electric field lines in the single cell elliptical cavity designed using CST MWS. Electric field lines in the elliptical cavity designed in CST MWS is shown in Fig. 5.9.

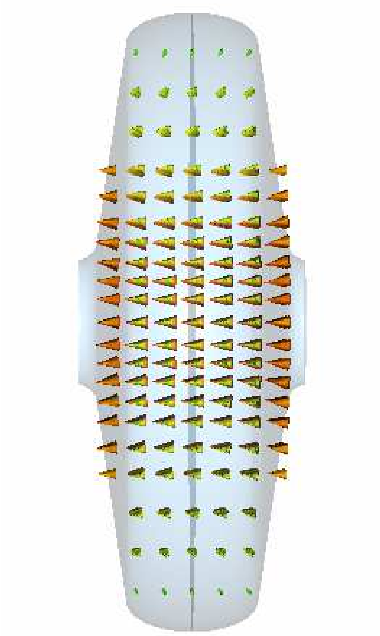

Fig. 5.9: Electric field lines in the elliptical cavity designed in CST MWS.

5.4 Summary and Conclusions

The 1 GeV linac for the Indian ADS programme will consist of superconducting structures after the RFQ. Preliminary optimizations of the electromagnetic design of the different types of superconducting cavities like the HWR, SSR and elliptical cavities have been done to get the resonant frequency and minimize the peak surface fields. Further detailed studies are in progress.

At intermediate energies, from 10 MeV to around 150 MeV, spoke resonators are proposed – the SSR1 to accelerate the beam to around 30 MeV followed by the SSR2 which will accelerate the beam to around 150 MeV. For the higher energy section, it is planned to use two types of 5-cell elliptical cavities corresponding to $\beta_G = 0.6$ and $\beta_G = 0.8$. The results of electromagnetic design simulations of 162.5 MHz HWR and the 325 MHz SSR0 for $\beta_G = 0.11$, and the 650 MHz elliptic cavities (both $\beta_G = 0.6$ and $\beta_G = 0.8$) are presented.

CHAPTER 6

Summary and scope of future work

6.1 Summary

The work in this thesis comprises of design and development of LEBT systems and design studies of high current, high energy linacs.

A two solenoid based magnetic LEBT has been designed for LEHIPA. The main design criterion was to match the beam from the ion source to the RFQ with minimum emittance growth and beam loss. For this detailed beam dynamics studies were done to study the beam transport in the LEBT. The beam to be transported through the LEBT is a low energy, high current beam. The space charge forces due to Coulombic repulsion between the particles in the beam are very strong for such a beam and causes increase in beam size and emittances. It was found from simulations that space charge compensation decreases the beam size as well as emittance growth in the LEBT. Hence space charge compensation will be used in the LEBT. The LEBT is 3.28 long and its functions include beam focusing and steering at the RFQ match point, dc beam current diagnosis and beam profile measurement through CCD monitors. The LEBT will also have a water-cooled collimator and an electron trap at the RFQ entrance. Design of LEBT components like the solenoids, steerers and electron trap has also been done.

A 400 keV, 1 mA deuteron RFQ based linac has been built at BARC. It consists of a rf ion source, a 400 keV RFQ for D^+ beams and a low energy beam transport (LEBT) line to match the beam from the ion source to the RFQ. The LEBT for this system was designed using 2 solenoids for focusing the beam. Based on the simulations, a LEBT test bench was setup at Van de Graaff to validate the simulations and focusing of the solenoids that were designed and fabricated. Experiments to measure the beam emittance and transmission in the line were done. The beam emittance measurement of Helium, Deuteron and proton beams was done using the solenoid scan and the slit wire method. The emittance values are well within the acceptance value for the RFQ.

A 1 GeV, 30 mA linac has been designed for the Indian ADS programme and its beam dynamics studies have been done. The linac is normal conducting upto 100 MeV and superconducting from 100 MeV to 1 GeV. It consists of an ECR ion source, a RFQ which will accelerate the beam to 3 MeV, DTL upto 40 MeV followed by CCDTL to accelerate the beam to 100 MeV. The proton beam is then accelerated to 1 GeV using superconducting 5 cell elliptical cavities. The total RF power required in the linac is about 33.5 MW. The total length of the designed accelerator is about 350 m and the overall transmission is about 96%. The 4% loss takes place in RFQ during bunching of the beam which is not expected to pose any radiation problem. In the high energy section superconducting cavities are used where the aperture to rms beam size ratio is high to minimize the risk of activation due to any beam loss.

In view of good progress in the field of superconducting cavities in the low and medium energy range and development of new structures like the superconducting spoke resonators that are suitable for acceleration of high current CW beams, it is proposed to go for superconducting structures right after the RFQ. The cavity design of a HWR at 162.5 MHz and single spoke resonator at 325 MHz, both for $\beta_G = 0.11$ has also been reported in this thesis. The design of elliptical cavities at 650 MHz for $\beta_G = 0.6$ and $\beta_G = 0.8$ has also been discussed.

6.2 Scope of future work

The LEHIPA LEBT has been designed as reported in this thesis. Based on this design, the various components have been fabricated. The next step is to assemble the LEBT with the ion source and validate the simulations. Also, the measurements will provide good insight to the phenomena of space charge compensation which cannot be completely understood be simulations alone. Elaborate experiments to study this effect in the LEBT with different types of gases at different gas pressure in the beam line have to done.

Design of high intensity linacs is a vast area and there is scope for lot of work in this field: from design optimization of accelerating structures to understanding the non linear effects due to space charge to improve the beam dynamics design. The beam dynamics reported in this thesis is with normal conducting structures like DTL and CCDTL in the medium energy range. But now in view of the plan to go ahead with superconducting structures right after the RFQ, detailed cavity dynamics and beam dynamics studies with these structures needs to be done. Another area where lot of work is required is understanding the formation of beam halos and eliminating them in high intensity linacs.

One of the most crucial issues in designing high current, high intensity proton accelerators is minimizing beam loss. Beam loss should be limited to less than 1 watt/m in the linac to be able to allow hands on maintenance of the machine. Beam loss can cause more severe effects in the high energy region where it gives rise to both shielding issues and activation of the accelerator components. Beam loss measurements at SNS and LANSCE suggest that even at a loss level of 1 watt/m (the SNS linac specification) hands-on maintenance is still possible with limited access time and strict administrative controls; however, it is advantageous to keep the losses as low as possible. The goal should be on the order of 0.1 watt/m, where unrestricted hands-on maintenance and quick access will lead to higher machine availability [65].

Beam halos [82] are identified as one of the dominant loss mechanisms in high intensity proton linacs. Beam halos are a small fraction of the particles surrounding the dense beam core which can eventually result in beam loss. Typically, the halo particles are considered as those that lie outside the phase space boundary of an ellipse with the same shape as the rms emittance and an area of about 8 to 10 times the rms emittance.

Although the exact mechanism for halo formation is not clearly understood, the main cause of beam-halo formation in high intensity proton-linac beams has been identified as arising from the space-charge forces that act in mismatched beams [83].

Some of the mechanisms that can result in the formation of halos in high intensity proton linacs are [84]:

1. The parametric 2:1 resonances - this results from the coupling of the mismatched beam core to the movements of single particles. This is the most important halo mechanism in high intensity linacs.
2. Envelope lattice resonances - these occur between the beam envelopes and the elements of a periodic focusing structure. They can cause rapid rms emittance growth and halo formation but can be easily avoided by keeping the zero current phase advance per period in all the three planes below 90°.
3. Intra-beam scattering Intra-beam scattering - this may be of importance in the LEBT section, where gas is introduced in the beam pipe for space charge compensation. In the high energy section of the linac, where the vacuum in the beam pipes is much better than in the LEBT, the effect of the intra beam scattering on halo formation seems to be negligible [85].

Beam loss can be prevented by careful beam dynamics studies preventing the halo formation in the beam. Although all emittance growth is not necessarily associated with the generation of a halo, halo formation is always accompanied by emittance growth [86]. Understanding of emittance growth and halo formation, as a result of many effects combined together, requires realistic computer simulations involving detailed beam dynamics studies with large number of particles. These can be done with the help of modern multi particle codes like IMPACT, TRACK and TRACEWIN which, in their parallelized versions can handle upto 10^8 particles and do these calculations in reasonable time frames.

References

1. F. Carminati, R. Klapisch, J.P. Revol, J.A. Rubio and C. Rubbia CERN/AT/93-47 (ET); C. Rubbia et al; CERN/AT/95-44 (ET); CERN/LHC/96-01 (EET); CERN/AT/95-53 (ET); CERN/LHC/97-01 (EET).
2. P.K.Nema, P.Singh, P.Satyamurthy, S.B.Degweker, V.K.Handu, "ADS Program and associated developments in India-Roadmap and Status Activities", ADS-INT-03, presented at IAEA Conference. http://www-pub.iaea.org/MTCD/publications/PDF/P1433_CD/datasets/papers/ads_int-03.pdf
3. S. S. Kapoor, Accelerator-driven sub-critical reactor system (ADS) for nuclear energy generation, Pramana – J. Phys. **59**, 6 (2002).
4. John W. Staples, "RFQs- An Introduction". AIP Conf Proc. 249, 1483 (1992).
5. M. Weiss, "Radio Frequency Quadrupole", Proc. CAS, Aarhus, Denmark, 1986; CERN 87-10 (1987).
6. Y. Cuvet, J. Genest, C. Vˆllinger, M. Vretenar, Development of a 352 MHz Cell-Coupled Drift Tube Linac Prototype, Proceedings of LINAC 2004.
7. P.Blewett, Proc. of the CERN Symposium 1956, p. 162.
8. U.Ratzinger et al., Nucl, Instr. and Meth. A, vol. 263 (1988), p. 261.
9. J.H.Billen, F.L.Krawczyk, R.L.Wood, and L.M.Young, 'New RF Structure for Intermediate-Velocity Particles', Proceedings of the 1994 International Linac Conference, Vol. 1, p. 341.
10. K. Schoenberg, The LANSCE Accelerator: A powerful tool for science and applications, Proceedings of PAC07, Albuquerque, New Mexico, USA.
11. S Henderson, Spallation neutron source progress, challenges and power upgrade paths, Proceedings of EPAC08, Genoa, Italy.
12. M. Lindroos, S. Molloy, D. McGinnis, C. Darve, H. Danared, ESS AB, Lund, The ESS Linac Design, Proceedings of LINAC2012, Tel-Aviv, Israel.
13. Lawrence, G.P. (1998), High-Power Proton Linac for APT; Status of Design and Development, Proc. of LINAC98, 23-28 August 1998, Chicago

14. D. De Bruyn & J.U. Knebel, "The Integrated Project EUROTRANS: EUROpean Research Programme for the TRANSmutation of High Level Nuclear Waste in an Accelerator Driven System (ADS)", 38th annual meeting of the IAEA Technical Working Group on Fast Reactors & Accelerator Driven Systems, Sao Paolo & Rio de Janeiro (Brazil), May 23 – 27 (2005).
15. Alex C. Mueller, Accelerator Studies for an ADS within the European Project EUROTRANS, AIP Conference Proceedings 798, 334 (2005).
16. D. De Bruyn, D. Maes, P. Schuurmans, G. Van den Eynde & H. Aït Abderrahim, Status of the ADS Research & Development and of the related technology in Belgium: the evolution of the MYRRHA project, IAEA Technical Meeting on the Review of the Status of Accelerator Driven Systems R&D and Technology, Vienna (Austria), 4-6 December,2006.
17. Accelerator Group, JAERI/KEK Joint Project Team, "Accelerator Technical Design Report for High-Intensity Proton Accelerator Facility Project, J-PARC", JAERI-Tech 2003-044, KEK Report 2002-13.
18. C. K. Park et al., The KOMAC Project: Accelerator and Transmutation Project in Korea, Proceeding of APAC98, Tsukuba, (1998).
19. Guan Xialing, The R/D of high power proton accelerator technology in China, Pramana – J. Phys. 59, No.6, 951- (2002).
20. A.M. Kozodaev, O.V. Shvedov, V.N. Konev, B.Yu. Sharkov, N.D. Gavrilin, N.V. Lazarev, D.A. Liakin, A.M. Raskopin, E.B. Volkov, Development and construction of experimental ADS at ITEP, Proceedings of EPAC 2002, Paris, France.
21. Sherman, J.D. et al. (1998), "Status Report on a dc 130-mA, 75-keV Proton Injector", Rev. Sci. Instr. **69,** 1003-8.
22. R. Gobin, Reliability of the High Power Proton Source SILHI, OECD/NEA Proc. 2nd International Workshop on Utilisation and Reliability of High-Power Proton Accelerators, 22-29 November 1999, Aixen- Provence, France.
23. S S Kapoor, Roadmap for development of accelerator-driven sub-critical reactor systems, BARC/2001/R/004.

24. P. Singh, S.V.L.S. Rao, Rajni Pande, T. Basak, Shweta Roy, M. Aslam, P. Jain, S.C.L. Srivastava, Rajesh Kumar, P.K. Nema, S. Kailas and V.C. Sahni, Accelerator Development in India for ADS Programme, Pramana – J. Phys. **68**, 33 (2007).
25. Rajni Pande, Shweta Roy, S V L S Rao, P Singh and S Kailas, Physics design of a CW high-power proton LINAC for ADS, Pramana – journal of Phys., Vol. 78. No. 2, Feb. 2012, pp-247-255.
26. P. Roychowdhury and D. P. Chakravarthy, "High intensity electron cyclotron resonance proton source for low energy high intensity proton accelerator", Rev. Sci Instrum. 80, 123305 (2009).
27. D. W. Cheng et al., "Design of the Prototype Low Energy Beam Transport Line for the Spallation Neutron Source", Paper WEA31, 1999 Particle Accelerator Conference, New York.
28. H. Vernon Smith, Jr., Terry Figueroa, Lash D. Hansborough, Margye Harrington, Kenneth Johnson, Debora Kerstiens, Subrata Nath, Joseph D. Sherman, Ralph R. Stevens, Jr., Michael Thuot, Lloyd M. Young, and Thomas J. Zaugg, Comparison of beam simulations with measurements for the LEDA LEBT H^+ beam, Proceedings of the 1999 Particle Accelerator Conference, New York, 1999.
29. N. Chauvin, O. Delferrière, R. Duperrier, R. Gobin, P.A.P. Nghiem, D. Uriot, Beam dynamics simulation of the Low Energy Beam Transport Line for IFMIF/EVEDA, Proceedings of LINAC08, Victoria, BC, Canada.
30. P. M**.** Lapostolle, IEEE Trans. Nucl. Sci**.** NS-18, 1101 (1971).
31. F. J. Sacherer, IEEE Trans. Nucl. Sci**.** NS-18**,** 1105 (1971).
32. PSI Graphic Transport Framework by U. Rohrer based on a CERN-SLAC-FERMILAB version by K.L. Brown et al.
33. TRACE 3D Documentation, Third edition Los Alamos Report LA-UR-97-886, May 1997
34. K.R. Crandall et al "RFQ Design codes" LANL Report 6A-UR-96-1836, Sept 10, 1997.

35. P.N. Ostroumov and K.W. Shepard. Phys. Rev. ST. Accel. Beams 11, 030101 (2001).
36. http://irfu.cea.fr/Sacm/logiciels/index3.php
37. http://www.pulsar.nl/gpt/index.html
38. D. P. Grote, Alex Friedman, Irving Haber, Jean-Luc Vay, The WARP Code: Modeling High Intensity Ion Beams, AIP Conference Proceedings, 749(1):55–58.
39. A. Chance, N. Chauvin, R. Duperrier, The SolMaxP Code, Proc. of IPAC 2012, New Orleans, USA.
40. Y.K. Batygin, Design issues of Low Energy Beam Transport, Proceedings of IPAC2013, Shanghai, China
41. Thomas Wangler, "RF Linear Accelerators", Wiley & Sons Publishers (1998) Page 218-219.
42. V. Kumar, Am. J. Phys. 77 (2009) 737
43. K.R. Crandall, R.H. Stokes and T.P. Wangler, Proc. 1979 Linac Conf., Brookhaven National Laboratory Report BNL-51134, (1979), p 205-216.
44. M Reiser, Theory and design of charged particle beams (John Wiley & Sons, New York, 1994).KV distribution, Page 361.
45. N. Chauvin, O. Delferrière, R. Duperrier, R. Gobin, P.A.P. Nghiem, D. Uriot, Beam dynamics simulation of the low energy beam transport line for IFMIF/EVEDA, Proceedings of LINAC08, Victoria, BC, Canada
46. M Reiser, Theory and design of charged particle beams (John Wiley & Sons, New York, 1994), Page 236.
47. Ferdinand, R., Sherman, J., Stevens Jr., R. R., and Zaugg, T. (1997) Space-charge neutralization measurement of a 75-kev, 130-ma hydrogen-ion beam.In Proceedings of PAC'97, Vancouver, Canada.
48. R. Gobin, P. Beauvais, R. Ferdinand, P. Leroy, L. Celona, G. Ciavola, and S. Gammino S., Improvement of beam emittance of the CEA high intensity proton source SILHI, Review of Scientific Instruments, 70(6):2652–2654.

49. J H Billen and L M Young, POISSON SUPERFISH, LA-UR-96-1834, L.A.N.L. K.R. Crandall.
50. CST microwave studio, simulation tool for electromagnetic analysis and design, CST, Germany
51. L.M. Young, et al., "High-Power Operations of LEDA," Proc. LINAC 2000 (Monterey, 21-25 August 2000) pp. 336-340.
52. E. Fagotti, “SPES LEBT: Electron Trap Device”, INFN-LNL (REP), 202/2004, 212-213.
53. S.V.L.S. Rao and P. Singh, Design studies of a high-current radiofrequency quadrupole for accelerator-driven systems programme, Pramana – Journal of Phys., Vol. 74, No. 2, February 2010, pp – 247-259.
54. S.V.L.S. Rao, Piyush Jain, Jose V. Mathew, Rajni Pande, Shweta Roy, S. Shrotriya, N. Patel, Shiju, M. R. Mishra, Gireesh Singh, L. Tayade, Praveen P., B.M. Kukreti, Rajesh Kumar, Manjiri Pande, S. Krishnagopal, S.K. Gupta, P. Singh, Design, development and acceleration experiments of a four vane RFQ at BARC, Ind. Particle Accelerator Conf. (InPAC-2013), 2011, VECC, Kolkata.
55. K.R. Crandall, D.R. Rusthoi, “Computer Program TRACE2D”, Los Alamos Scientific Laboratory Report, LA-10235, 1986.
56. Rajni Pande, S V L S Rao, Shweta Roy, Manas Mishra, L.D Tayade, P.R Parate, Sapna P, Shailaja Ware, S.K Singh, A Agarwal, S.K Gupta, P Singh, A LEBT for the 400 keV RFQ based neutron generator at BARC, Ind. Particle Accelerator Conf. (InPAC-2011), 15-18 February, 2011, IUAC, New Delhi.
57. Thomas Wangler, “RF Linear Accelerators”, Wiley & Sons Publishers (1998) Page 207-208.
58. Thomas Wangler, “RF Linear Accelerators”, Wiley & Sons Publishers (1998), Page 265.
59. S.Y. Lee, Accelerator Physics(World Scientific, 2004), Page 62-63.

60. Wai-Ming Tam, Charecterization of the Proton ion source beam for the high intensity neutrino source at Fermilab, PhD Thesis.
61. J.G. Wang, D.X. Wang, M. Reiser, Beam emittance measurement by the pepper-pot method, Nuclear Instruments and Methods in Physics Research Section A: Accelerators, Spectrometers, Detectors and Associated Equipment, Volume 307, Issue 2, Pages 190-194.
62. K. Kasamsook, K. Akiyama, K. Nanbu, M. Kawai, F. Hinode, T. Muto, T. Tanaka, M. Yasuda, Y. Mori, H. Hama, "Beam quality measurements of a low emittance dc gun employing a single crystal of LaB_6 cathode", Proceedings of the4th Annual Meeting of Particle Accelerator Society of Japan and the 32nd Linear Accelerator Meeting in Japan (August 1-3, 2007, Wako Japan)
63. V S Pandit, P R Sarma, S Bhattacharya and R K Bhandari, The measurement of the RMS emittance of an ion beam with an arbitrary density profile, Meas. Sci. Technol. 8 (1997) 1085–1089.
64. Jose V. Mathew, S. V. L. S. Rao, Rajni Pande, M. R. Mishra, L. D. Tayade, P. R. Parate, P. Singh, Transverse Emittance Measurement Studies of a Deuteron Ion Source Beam, Ind. Particle Accelerator Conf. (InPAC-2013), 2011, VECC, Kolkata.
65. Robert A. Hardekopf, Beam loss and activation at LANSCE and SNS, 7th ICFA Mini-Workshop on High Intensity, High brightness Beams, Sept 1999.
66. J.H.Billen, F.L.Krawczyk, R.L.Wood, and L.M.Young, 'New RF Structure for Intermediate-Velocity Particles', Proceedings of the 1994 International Linac Conference, Vol. 1, p. 341.
67. T. P. Wangler, Principles of RF Linaear Accelerators, John Wiley & Sons, INC, 1998, page 46-47.
68. R S Mills, K R Crandall and J A Farrell, Designing Self-Matching Linacs, Proc. 1984, Linac Conf.
69. Rajni Pande, Shweta Roy, T. Basak, S.V.L.S. Rao and P. Singh, Beam Dynamics for the 1 GeV Proton Linac for ADS, Proc. Indian Particle

Accelerator Conference (InPAC-2006), BARC, Mumbai, Nov. 1-4, 2006, page 207.

70. J.H.Billen, PARMILA Code, LA-UR-98-4478, Revised July 26, 2005.
71. H Padamsee et al, RF Superconductivity for Accelerators, Cornell University Ithaca, New York (Wiley-Interscience Publication, 1998) Page 6-8.
72. C. Pagani, D. Barni, A. Bosotti, P. Pierini, Design criteria for elliptical cavities, The 10th Workshop on RF Superconductivity, 2001, Tsukuba, Japan.
73. D Barni et al, SC cavity design for the 700 MHz TRASCO linac, EPAC, 2000.
74. Gonin, T. Khabibouline, G. Lanfranco, A. Mukherjee, J. Ozelis, L. Ristori, G. Romanov, D.A. Sergatskov, R. Wagner, R. Webber, G. Apollinari, High gradient test results of 325 MHz Single Spoke cavity at Fermilab, Proceedings of LINAC08, Victoria, BC, Canada.
75. Rajni Pande, Shweta Roy, S. V. L. S. Rao, S. Krishnagopal, P. Singh, Design of RF structures for a superconducting proton linac, Proc. of InPAC 2013, VECC, Kolkata.
76. C. S. Hopper and J. R. Delayen, Superconducting spoke cavities for high-velocity applications, Physical Review STAB, 16, 102001 (2013).
77. J. R. Delayen, "Ponderomotive Instabilities and Microphonics ", Physica C 441 (2006) p. 1.
78. H Padamsee, *RF superconductivity*, WILEY-VCH Verlag GmbH & Co. KGaA, Weinheim, 2009, Page 18.
79. Thomas P Wangler, "RF Linear Accelerators", 2008 WILEY-VCH Verlag GmbH & Co. KGaA, Weinheim (2008) Page 33-42.
80. Z.A. Conway, R.L. Fischer, S.M. Gerbick, M.J. Kedzie, M.P. Kelly, S.V. Kutsaev, B. Mustapha, P.N. Ostroumov and K.W. Shepard, Development of a superconducting Half Wave Resonator for PXIE, Proceedings of LINAC2012, Tel-Aviv, Israel.
81. K. Shepard *et al.*, "Development of Niobium Spoke Cavities for a Superconducting Light-Ion Linac", Proceedings of the XIX International Linac Conference, Chicago Illinois, p. 956.

82. C. K. Allen and T. P. Wangler, “Beam halo definitions based upon moments of the particle distribution” PHYSICAL REVIEW SPECIAL TOPICS - ACCELERATORS AND BEAMS, VOLUME 5, 124202 (2002).
83. T.P. Wangler et al., "Dynamics of Beam Halo in Mismatched Beams", Proc. of Linac96, Geneva, August 26-30, 1996.
84. Frank Gerigk, Beam Halo in high intensity hadron linacs, 2006.
85. N. Pichoff, Intrabeam scattering on halo formation, Proc. Particle Accelerator Conf., New York, USA, 1999.
86. Thomas P. Wangler, “RF Linear Accelerators” (2008 WILEY-VCH Verlag GmbH & Co. KGaA, Weinheim), pp 325-329.